The metal-semiconductor interface: Fe-Si(001) and Fe-InP(001)

Dissertation

zur Erlangung des akademischen Grades

Doctor rerum naturalium (Dr. rer. nat.)

vorgelegt der

Mathematisch-Naturwissenschaftlich-Technischen Fakultät
(mathematisch-naturwissenschaftlicher Bereich)
der Martin-Luther-Universität Halle-Wittenberg

von Herrn **Florin Zavaliche**

geb. am: 09. Januar 1970 in Bacău, Rumänien

Gutachterin/Gutachter:

1. Prof. Dr. rer. nat. Jürgen Kirschner

2. Prof. Dr. rer. nat. Ulrich Köhler

3. Prof. Dr. rer. nat. Henning Neddermeyer

Halle/Saale, ____16 April 2002____

Abstract

Spinelectronics has been greatly benefiting from the investigation of the ferromagnet-semiconductor interface. In this work, a study of the reconstructions of Si(001) and InP(001) surfaces, and the characterization of thin Fe films grown on these substrates are presented. To suppress Fe-Si reactions, a Au buffer layer was grown in two steps on (2×1) Si(001). First, a reconstruction of the Si(001) surface was performed by the deposition of less than one monolayer of Au at around 1000 K. The reconstructed surface is characterized by enlarged structural units on rectangular-like terraces. Second, an ultrathin Au layer was added but the films are disordered. The early onset of a strong out-of-plane magnetization in ultrathin Fe films deposited on buffered Si(001) at 150 K points at a significant reduction of silicide formation. The perpendicular orientation of magnetization in ultrathin Fe films grown at 150 K is either preserved or is recovered upon annealing close to room temperature. This behavior cannot be put solely on the expense of competition between the relevant anisotropy terms, and structural and/or compositional modifications in the growing film are considered. The InP(001) substrates cleaned by ion bombardment show a highly ordered P-rich (2×4) reconstructed surface. Different stackings of the (2×4) units, comprised of mixed In-P and missing dimers, are revealed. The growth of Fe films on P-rich (2×4) InP(001) in the submonolayer thickness range does not show any preferential growth direction and a disordered film is obtained as the thickness is increased. Auger electron spectroscopy data reveal the segregation of one monolayer of In to the top of the growing Fe film at 300 K, but does not support a strong Fe-InP(001) intermixing. The current-voltage characterization of patterned Fe films grown on n-InP(001) show non-rectifying contacts at room temperature. A uniaxial in-plane magnetic anisotropy was observed up to an Fe thickness of ≈14 monolayers and the surface/interface contribution is assessed. From the magnetization behavior it is deduced that very small, if any, magnetically dead layers form at the interface. The presented results make the Fe-Si and Fe-InP systems good candidates for spinelectronic applications.

II

Zusammenfassung

Das Forschungsgebiet der Spinelektronik hat in der Vergangenheit viel von Untersuchungen der Grenzschichten zwischen Ferromagneten und Halbleitern profitiert. In der vorliegenden Arbeit wird über Untersuchungen zu den Oberflächenrekonstruktionen von Si(001) und InP(001) und dem Wachstum von Fe Schichten auf diesen Substraten berichtet. Um Fe-Si Reaktionen zu unterdrücken, wurde eine Au Pufferschicht in zwei Stufen auf die (2×1) Si(001) Oberfläche aufgewachsen. Zunächst wurde eine Rekonstruktion der Si(001) Oberfläche durch Deposition von weniger als einer Atomlage Au bei etwa 1000 K durchgeführt. Die rekonstruierte Oberfläche ist durch größere strukturelle Einheiten von nahezu rechteckigen Terrassen gekennzeichnet. Als nächstes wurde eine ultradünne Au-Schicht hinzugefügt, die jedoch ungeordnet ist. Das frühe Einsetzen einer stark aus der Ebene orientierten Magnetisierung in ultradünnen Fe-Schichten, die auf den so gepufferten Si(001) bei 150 K abgeschieden wurden, deutet auf eine deutlich reduzierte Silizidbildung. Die senkrechte Orientierung der Magnetisierung in ultradünnen Fe Schichten, die bei 150 K abgeschieden wurden, bleibt entweder erhalten oder wird beim Aufheizen bis nahe an Raumtemperatur wiederhergestellt. Dieses Verhalten kann nicht ausschließlich den konkurrierenden Prozessen zwischen den relevanten Anisotropiebeiträgen zugeschrieben werden, weshalb Änderungen der Struktur und/oder der Zusammensetzung während des Wachstums in Betracht gezogen werden. Die durch Ionenbeschußgereinigten InP(001)-Substrate weisen eine hochgradig geordnete P-reiche (2×4) rekonstruierte Oberfläche auf. Verschiedene Abfolgen der (2×4) Einheitszellen, zusammengesetzt aus gemischen In-P Dimeren, werden gezeigt. Das Wachstum von Fe Filmen auf P-reichen (2×4) InP(001) Oberflächen im subatomaren Dickenbereich zeigt keine präferentielle Wachstumsrichtungen und ungeordnete Filme werden beobachtet, wenn die Bedeckung erhöht wird. Augerelektronenspektroskopiedaten belegen die Segregation einer Atomlage von In auf der Oberfläche des wachsenden Fe Films bei 300 K, schließen aber eine starke Durchmischung aus. Die Stromspannungskennlinien von strukturierten Fe Filmen auf n-InP(001) zeigen ohmsche Kontakte bei Raumtemperatur. Es wurde eine uniaxiale magnetische Anisotropie in Fe Filmen bis 14 Atomlagen beobachtet, die auf die Grenzfläche oder die Oberfläche des Fe Films zurückzuführen ist. Aus dem Verhalten der Magnetisierung wird geschlossen, daß sehr wenige oder keine magnetisch tote Lagen an der Grenzfläche zum Substrat vorliegen. Die dargestellten Resultate legen nahe, daß die Systeme Fe-Si und Fe-InP geeignete Kandidaten für Anwendungen in der Spinelektronik sind.

Contents

"(...) the greatest curiosity, upon which the fate of the island depends, is a loadstone of a prodigious size, in a shape resembling a weaver's shuttle. (...) By this loadstone, the island is made to rise and fall, and move from one place to another. (...) For in this magnet the forces always act in lines parallel to its direction."

Jonathan Swift (1667-1745), *Gulliver's Travels*

Chapter 1

Introduction

A strong interest towards the investigation of the ferromagnet-semiconductor interface has been triggered by the work of S. Datta and B. Dass [1], who proposed the first spin-electronic analogue of the electro-optic light modulator ushering thus what was latter called *magnetoelectronics* [2]. In spite of the large amount of experimental effort focused on the topic, a recent work imposed severe restrictions on the functionality of integrated ferromagnetic metal-semiconductor solid-state devices [3]. Instead, it was proven that an entirely semiconductor-based system is feasible [4], however, only under extreme conditions of low temperatures and high magnetic fields.

From the pragmatic requirement of functionality with moderate magnetic fields and at environmental temperatures, the concept of spin-injection into semiconductors needs substantial modifications, *e.g.* by the integration of a tunnel junction to produce hot electrons as part of the spintronic device [5]. Alternatively, spin polarized electrons can be generated in a metal-based spin-valve structure where hot electrons are injected and filtered by the Schottky barrier [6]. Therefore, the presence of a uniform Schottky barrier appears to be crucial for the feasibility of the device [7]. If a tunnel junction is used as the source of hot spin-polarized electrons, the presence of an additional barrier at the metal-semiconductor contact might not necessarily be beneficial. To maintain a high spin polarization of hot electrons passing into a semiconductor, where the signal is then processed, it is necessary that the electrons see a reduced amount of interface states. These interface states, which may trap the tunneling electrons on their way to the bulk of the semiconductor are responsible for the Fermi level pining and give rise to an enhancement of the Schottky barrier [8]. Therefore, even if hot electrons are to be used for spin

injection into semiconductors, it appears that low rectifying contacts are highly desired. In the context of metal/III-V compound semiconductor contact, it has been reported that metal films which strongly react with the semiconductor anion give rise to small Schottky barrier heights [9, 10]. In addition to the possible hindrance of a high contact barrier, a non-magnetic layer at the interface between the ferromagnet and semiconductor, usually structurally disordered, might act on the travelling hot electrons as strong spin scatterers, preventing thus the spin information being transferred into the semiconductor; all these facts should be considered seriously in the choice of the proper ferromagnet-semiconductor system. Hence, the study of its interface with several surface science and magnetic techniques is necessary to learn more about the basic phenomena occurring at this crucial interface.

Among the possible candidates for substrates, the (001) oriented Si and InP crystals were selected. Silicon based components find themselves basically in every electrical apparatus whose complexity exceeds the one of a simple switch, making our daily life hardly conceivable without the advent of the silicon technology. While the constituents of the cells building up the living beings are carbon based, silicon finds itself at the core of everything artificially powered, and a huge amount of work has been dedicated toward its investigation. The new trends in microelectronics raises the question whether silicon is able to cope with the challenges posed by the emerging field of spin electronics. In this respect, the investigation of the metallic films grown on its technologically relevant (001) surface is of special interest.

In particular, it was found that such substrate strongly reacts with the deposited iron resulting in an amorphous and poorly defined interface, associated with the formation of silicides [11–16] even at ambient growth temperatures [17]. If spin injection applications are kept in mind, such interfaces may act as strong scatterers for electrons passing through the interface, potentially reducing the spin information. To avoid this, a thin, stable and spin-preserving passivation layer of the semiconductor surface is highly desirable in order to reduce intermixing at the Fe-semiconductor interface. Since the previous attempts using non-metal passivation agents were not successful [18, 19] an alternative way had to be considered. Gold seems to be appropriate at least for the relatively large attenuation length ($\lambda > 230$ Å) for ballistic electron transport in Au grown on Si(001) [20]. Besides, the possibility of suppressing the spin-flip scattering for tunneling electrons through a Fe/Au multilayer base fabricated onto an n-type Si(001) collector [21], makes Au the favorite candidate for our purpose. Therefore, the thermodynamically stable Au-induced

reconstruction of Si(001) surface [22, 23], has been used as the first step in the attempt to reduce silicide formation at the Fe/Si interface. In addition, by tempering with the Fe-Si(001) interface, the direction of magnetization can be rotated either out-of the plane or into the film plane, as it will shown in Chapters 3 and 5.

Interesting physics is expected to emerge upon the growth of thin Fe films on InP(001) since it shows a lattice mismatch of only +2.2 %. The relevance of InP(001) in the field of high speed and high frequency (opto-) electronic components and the possibility of realizing low rectifying contacts [24, 25] were kept in mind. It is worth emphasizing that the properties of InP allow the fabrication of semiconductor laser diodes whose wavelength matches the optimum transmission in silica fiber optics. However, early studies reported that strong reactions occur at the Fe-InP interface [9, 10, 25, 26], and not even sulphur passivation of InP is able to prevent the intermixing with the growing Fe film [27].

In this thesis, the growth and magnetic properties of thin Fe films deposited on the (001) surface of Si and InP are investigated. An overview of the experimental methods used in this study together with some insights into their underlying physics is presented in Chapter 2. In Chapter 3, after a brief characterization of the Si(001) surface, the properties of Fe films grown on such substrates are reviewed. In the next sections of Chapter 3, attention is being paid to the surface modifications induced by Au deposition at high temperatures followed by an investigation of the Fe films grown by molecular beam epitaxy on the passivated substrate.

In Chapter 4, the surface of InP(001) prepared by sputtering at elevated temperatures is characterized with respect to its structure and morphology. A unique microscopic appearance among the other III-V compound semiconductors is observed. Thin Fe films of thickness ranging from the submonolayer coverage to almost 20 monolayers grown by molecular beam epitaxy were characterized with respect to their structural, morphological, compositional and magnetic properties.

The main results of the work presented in this thesis are discussed in Chapter 5. Emphasis will be put on the details of surface reconstructions, the degree of interfacial reaction, and on some aspects concerning the observed uniaxial magnetic anisotropy.

In spite of some hindrances, it will be shown in this work that thin Fe films grown on both Si and InP(001) show appealing properties which make the systems good candidates for being integrated into new fields of the semiconductor technology. Finally, all the findings presented in this thesis will be summarized in Chapter 6.

Chapter 2

Experimental methods

In this work, sample preparation and characterization was carried out *in-situ* under *ultra high vacuum* (UHV) conditions at a base pressure better than $\approx 8 \times 10^{-11}$ mbar. As single crystal substrates, both elemental (Si) and III-V compound (InP) semiconductors with the (001) surface orientation were used. Prior to film growth, the contaminants and the native oxide layers were removed either by thermal desorption or by ion bombardment at elevated temperatures. Details on the sample preparation are given in the forthcoming chapters. The Fe (99.99 % purity) deposition was performed by means of an electron beam evaporator at growth rates of about 1.5 monolayers (ML) per minute, where the monolayer coverage is defined in terms of the atomic density of bcc Fe(001), *i.e.*, 1.22×10^{15} atoms/cm^2. Au was evaporated by electron bombardment from a Mo crucible, growth rates of about 0.5 ML/min being obtained (1 ML Au = 1.20×10^{15} atoms/cm^2). The low temperature (LT) growth was performed by cooling the sample holder with liquid nitrogen down to 150 K.

The samples investigation was done with respect to their *structural*, *morphological* and *magnetic* behavior, as well as to their *chemical* composition. The following surface investigation techniques were employed: *Auger electron spectroscopy* (AES) to determine the chemical composition, *low energy electron diffraction* (LEED) to assess the structural information, *scanning tunneling microscopy* (STM) to investigate the surfaces and films morphology and the *magneto-optic Kerr effect* (MOKE) to probe the films magnetization. These experimental techniques will be described in detail in the following sections.

A schematic drawing of the experimental setup used in this work is shown in Fig. 2.1. The system is made up of three chambers: a two stage *load-lock*, the "STM" chamber

and the preparation chamber, equipped as sketched in the figure. The two-stage load-lock allows sample and STM tip transfer in and out of the UHV chambers without breaking the vacuum. Whenever a transfer is required, the lower part, *i.e.*, the air-lock stage, can be vented and pumped down to $\approx 1 \times 10^{-6}$ mbar, while the upper part, the UHV stage, is permanently pumped by an ion pump down to $\approx 5 \times 10^{-9}$ mbar. The two load-lock stages are both equipped with carousels for samples and STM tips storage. A third carousel located in the "STM" chamber, as sketched in Fig. 2.1, allows the sample/tip storage under the best UHV conditions. For sample preparation, *i.e.*, substrate cleaning and film
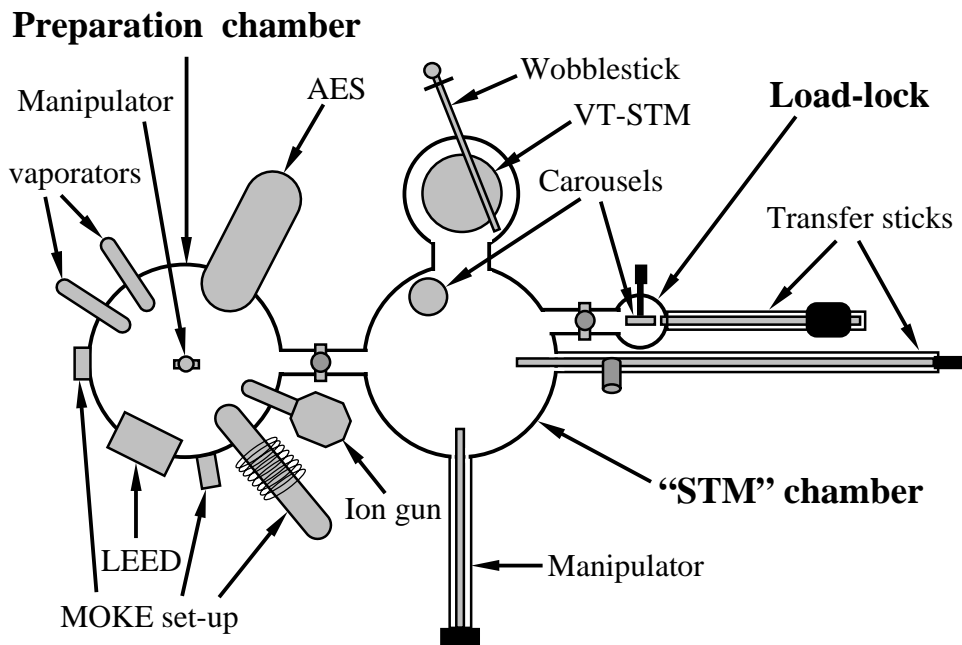
Figure 2.1: A top view sketch of the experimental setup.

growth, freshly cut and mounted single crystal substrates are transferred through the whole UHV system into the preparation chamber where the corresponding techniques are being used. Only the STM measurements are performed in a separate chamber to keep the instrument far from all possible noise sources. To coarsely reduce the mechanical noise, the whole system is placed on small pressurized pillars which insure a relatively good insulation from the building vibrations. A more sofisticated damping system does not appear to be necessary since the STM itself benefits of an eddy-current damping consisting of copper elements and permanent magnets.

2.1 Auger electron spectroscopy

The first technique employed to assess the degree of the substrate cleanness is Auger electron spectroscopy, a powerful tool for probing the surface chemical composition [28]. For short, upon bombarding the surface of a sample with a several keV energy radiation, the energies of the emitted electrons are analyzed and attributed to different chemical species. The effect was discovered by Auger in 1925 [29] by using X-rays as the primary radiation, and after almost 30 years, in 1953, Lander substituted them with an electron beam [30].
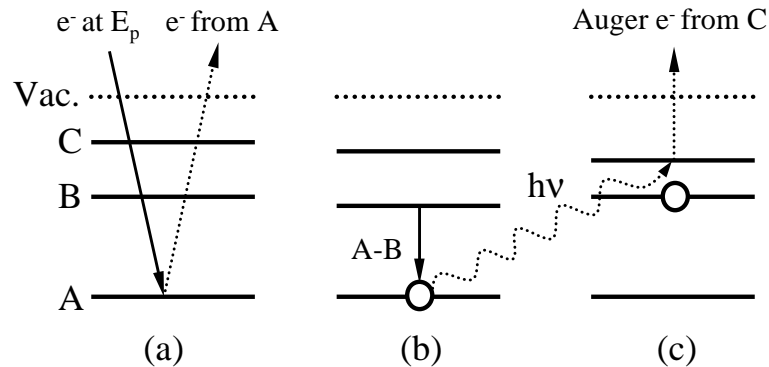
Figure 2.2: A diagram of the processes leading to the emission of an Auger electron: (a) an incident electron with the energy E_p kicks out an electron from the inner shell, A; (b) an electron from the shell B decays in the empty state in A, and (c) the emitted photon is absorbed by an electron from the shell C, which leaves the specimen if the gained energy is higher than the vacuum level.

If an electron beam of energy E_p of the order of keVs impinges on the surface of a solid, a continuous spectrum of electron energies ranging from 0 eV to E_p can be detected. Peaks of various heights and widths can be seen in the spectrum, according to the mechanisms lying behind their occurrence. A sharp peak at the energy E_p and a broad one between 0 and ≈200 eV correspond to the two extreme cases, respectively: the *elastic scattering* and the emission of the *true secondaries* as the result of a cascade inelastic scattering inside the solid. Located between them in energy, on the top of an almost constant background, weak peaks can be distinguished, which are associated with Auger processes, as described in the following. Let us consider an incident electron with the energy E_p striking, for the sake of simplicity, a single atom (Fig. 2.2). The inner shells involved in the processes leading to the emission of an Auger electron will be denoted A, B, and C, which stand for

either of the K,L,M or N atomic levels. As the immediate consequence of the collision, an electron from the inner shell A is ejected from the atom, leaving a single ionized atom, whose electronic configuration is far from its ground state (Fig. 2.2(a)). The hole left behind is depicted in Fig. 2.2 by an open circle. The more shallow levels, B and C, are all shifted downward by the same amount because the nuclear charge screening is less effective as the result of the inner shell ionization. To minimize the energy, an electron from the level B, experiences a decay into the empty state in the shell A (Fig. 2.2(b)). Following this process, a photon with the corresponding energy is emitted and, in turn, may be absorbed by an electron from the even more shallow level. As the hole moves upward, the shell B is repositioned at the initial energy, since it "sees" again the fully screened nucleus charge. The same reasoning does not apply, though, to the shell C. Now, if the energy emitted following the $B{\rightarrow}A$ transition is absorbed by an electron in the C shell, it will leave the atom provided that the energy gain overcomes the vacuum level (Fig. 2.2(c)). The later emitted electron into vacuum is called the *Auger electron*, whose energy depends on the binding energies of the levels involved in the transitions [31]. It is obvious that the Auger electron bears the whole information concerning the inner electronic configuration, which in turn, is determined by the atomic number. Thus, the Auger spectrum is a direct fingerprint of the chemical composition of a specimen. Moreover, since the *mean escape depth* (the average depth were the Auger electrons of a certain energy originate from) is of the order of a few atomic layers, the method appears to be not only *compositional* but also *surface* sensitive.

The progress leading to the AES technique as it is currently used in the our days is due to Harris [32], who firstly proved the advantages of the energy distribution differentiation of the emitted electrons. However, the crucial improvement was made by Palmberg *et. al.* [33] who increased the instrument's sensitivity by orders of magnitude by introducing the so called *cylindrical mirror analyser* (CMA), sketched in Fig. 2.3.

It mainly consists of two coaxial cylinders of radii r_1 and r_2, respectively, in a ratio of about $r_2/r_1 \cong 2$. A variable deflecting voltage $-V$ is applied to the outer cylinder, so that, for a given energy E, and a fixed emission angle of 42°18' (see the Fig. 2.3), the focusing condition reads:

$$\frac{E}{V} = 1.3098 \frac{1}{ln(r_2/r_1)}. \tag{2.1}$$

The electron beam entering through the aperture in the space between the two cylinders is deflected through the final exit of the analyzer aperture and enters the *channeltron*.
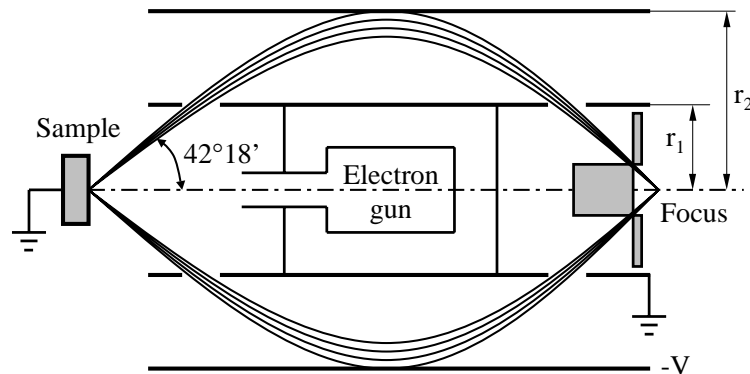
Figure 2.3: A section through the cylindrical mirror analyser with internal electron gun.

The electron current is typically about 10 nA, while the channeltron's dark current is of the order of 1 pA. These values are characteristic for the analyzer used in this work, an *Omicron CMA 150*. Since only the energy distribution *N(E)* is produced in this way, a small modulation is superimposed on the deflecting voltage to obtain the differential distribution *dN(E)/dE*. Therefore, by means of the *lock-in* technique, the first harmonic of the collected current is recorded, whose amplitude is proportional to the desired quantity. Finally, the differential distribution in the energy range of interest is obtained.

2.2 Low energy electron diffraction

While the inelastic scattering between a low energy radiation and a specimen gives valuable insights on the surface composition, the elastic scattering in the energy range of minimum penetration depths offers information on the surface structure. The LEED technique is one of the most important tools in acquiring fast and reliable structural information on the samples' surface. The apparatus used in this work, a rear view *Omicron SPECTALEED* with a LaB_6 filament is schematically shown in Fig. 2.4(a). Both the basic technique and the construction of the LEED pattern can be easily understood by means of the *Ewald sphere*. This is a sphere built in the reciprocal space, whose radius is given by the initial wavevector of the incoming electrons, $\mathbf{k_i}$, divided by 2π. As one can see in Fig. 2.4 for an electron beam at normal incidence, every diffraction spot is located on the sphere, and its position can be expressed as $\mathbf{K} = \mathbf{k_f} - \mathbf{k_i}$, where $\mathbf{k_f}$ is the wavevector of the scattered electron, whose length equals the sphere's radius. With this technique, one can assess the periodicity from the presence and arrangement of the
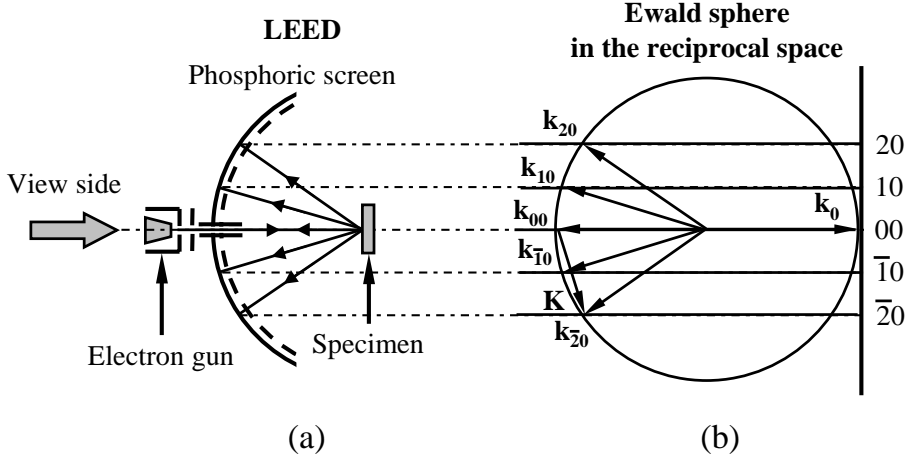
Figure 2.4: A sketch of the LEED technique (a), and the construction of the Ewald sphere in the reciprocal space, for an electron beam at normal incidence (b). The first and second order diffraction spots are illustrated.

diffracted spots, the atom position within the unit cell from spot intensity-beam energy curves, and the arrangement of the building units from the spot profile analysis. The last two quantitative aspects require extensive calculations and precise data acquisition technique. In the following, such approach is briefly addressed. Since in general only the structure of the ultimate surface layer is relevant, phenomena like interference from different atomic layers and multiple scattering are neglected. This approach is known as the *kinematic approximation* [34].

Let us consider an electron with the initial wavevector $\mathbf{k_i}$ which is scattered to the final state $\mathbf{k_f}$ by a specimen surface. The observable quantity, *i.e.*, the diffracted intensity, is given by [35]:

$$I(\mathbf{K}, \mathbf{k_i}) = |\Psi(\mathbf{K}, \mathbf{k_i})|^2 = \sum_{\mathbf{n},\mathbf{m}} f(\mathbf{n})f^*(\mathbf{m})e^{i\mathbf{K}[\mathbf{r(n)}-\mathbf{r(m)}]} \qquad (2.2)$$

where $\mathbf{K} = \mathbf{k_f} - \mathbf{k_i}$ is the scattering vector, and $\Psi(\mathbf{K}, \mathbf{k_i})$ the wavefunction of the scattered electron [36]. The scattering amplitudes, f($\mathbf{n}$) and f($\mathbf{m}$), depend on both $\mathbf{K}$ and $\mathbf{k_i}$, and combine the wave coming from the n-th, and m-th surface atom, respectively, and all underlying atoms. It may be expressed in terms of the Fourier transform of a distribution in the direct space. Equivalently, the scattered intensity may be written as

$$I(\mathbf{K}, \mathbf{k_i}) \propto |F(\mathbf{K}, \mathbf{k_i})|^2 = \sum_{h,k,l} |F_{hkl}|^2 \delta\{\mathbf{K} - (h\mathbf{a}^* + k\mathbf{b}^* + l\mathbf{c}^*)\} * |S(\mathbf{K}, \mathbf{k_i})|^2 \qquad (2.3)$$

where $F(\mathbf{K}, \mathbf{k_i})$ is the Fourier transform of the distribution in the direct space, F_{hkl} the structure factor, *h, k, l* the Miller indices, and $\mathbf{a}^*, \mathbf{b}^*, \mathbf{c}^*$ the basis vectors of the reciprocal lattice. The quantity $S(\mathbf{K}, \mathbf{k_i})$ is the shape function arising from finite volume considerations.

If only the spot profiles are to be analyzed, further simplifications can be made by assuming a homogeneous surface, where all scattering amplitudes are the same and equal to $f = f(\mathbf{K}, \mathbf{k_i})$. In addition, $\mathbf{r}(\mathbf{n}) = \mathbf{r}(\mathbf{n_x}, \mathbf{n_y})$ can be written as $\mathbf{a}_x n_x + \mathbf{a}_y n_y + \mathbf{d_z} h(\mathbf{n})$, with $\mathbf{n} = (n_x, n_y)$ the unit mesh, $\mathbf{a}_x$ and $\mathbf{a}_y$ the in-plane unit vectors, $\mathbf{d_z}$ the vertical unit vector and $h(\mathbf{n})$, the height of the unit cell. Under this approximation the intensity can be split as $I(\mathbf{K}, \mathbf{k_i}) = F(\mathbf{K}, \mathbf{k_i})G(\mathbf{K})$, into a *dynamical form factor* giving the intensity from a single unit:

$$F(\mathbf{K}, \mathbf{k_i}) = |f(\mathbf{K}, \mathbf{k_i})|^2, \tag{2.4}$$

and a *lattice factor* containing the information about the surface structure (describes the spot position):

$$G(\mathbf{K}) = \sum_{\mathbf{n}} \langle e^{i d\mathbf{K}_\perp [h(\mathbf{n+m}) - h(\mathbf{m})]} \rangle e^{i a\mathbf{K}_\parallel \mathbf{n}}, \tag{2.5}$$

where $\mathbf{K}$ was decomposed into a parallel ($\mathbf{K}_\parallel$) and a perpendicular component ($\mathbf{K}_\perp$) to the specimen surface. In turn, the lattice factor is split into a central part depending on $\mathbf{K}_\parallel$, accounting for the sharp Bragg spots given by an ideal surface, and a diffuse profile due to the surface roughness. Thus, the LEED pattern consists of central spikes $I_0(\mathbf{K}_\perp)$, whose sharpness depend on the instrument's transfer function, surrounded by a broadening $I_{diff}(\mathbf{K}_\perp, \mathbf{K}_\parallel)$. The two above contributions vary in anti-phase with each other. Accordingly, from a careful inspection of the lattice factor, important information about steps and defects at surfaces can be obtained [37, 38].

The surface lattice constants of a specimen placed at a known distance from the LEED screen, namely *L* (Fig. 2.5), can be easily derived from the single slit diffraction condition which reads:

$$a \cdot sin\theta = n\lambda, \tag{2.6}$$

where *a* is the corresponding lattice constant, and θ the angle between the incident and the diffracted electron beams. Since low energy electrons are used to probe the surface structure, the *de Broglie* wavelength, λ, after a trivial algebraic manipulation, is classically given by

$$\lambda = \sqrt{\frac{1.50}{E}}\ nm, \tag{2.7}$$
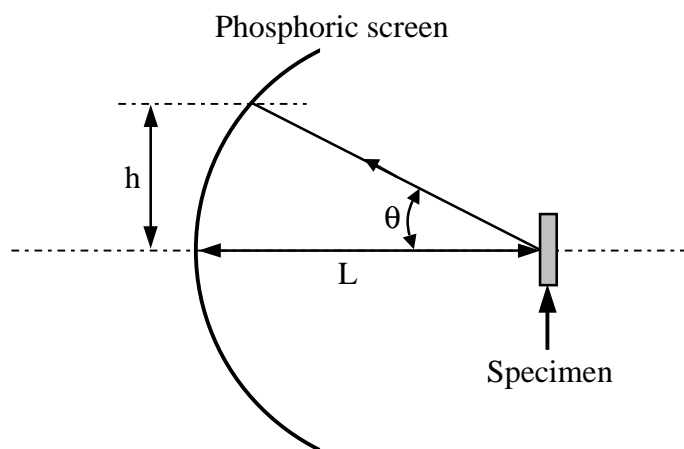
Figure 2.5: The geometrical construction of the n-th order diffraction spot given by a specimen placed at the distance L from the LEED screen.

where E stands for the electron beam energy expressed in eV. Therefore, the derivation of the surface lattice constants is straightforward, provided that the corresponding macroscopic distances are accurately determined.

2.3 Scanning tunneling microscopy

So far, two experimental techniques for surface compositional and structural analysis, respectively, have been briefly reviewed. In spite of the atomic resolution capabilities of the LEED method, it does not provide the complete information on the atomic position in real space, since the phase information is lost by multiplying the Fourier transform of real space distribution with its complex conjugate. If this quantity, in turn, is inverse Fourier transformed, than the so called *Patterson* or *self correlation function* is obtained. As its name says, it gives mere the probability of finding a certain atom at a given distance from a reference one. In addition, the diffraction data is the result of an average of the structure information over the lateral size of the electron beam. Therefore, it appears necessary to device a method able to locally sample the surface in the real space directly, if complete information about the atomic positions is required. Moreover, such a method would be extremely helpful to study local defect phenomena or processes related to the incipient growth stages. The problem was solved by Binning and his coworkers [39] in the early 1980s by constructing the first scanning tunneling microscope (STM) [40].

In the STM apparatus, a sharp metallic tip is brought into close proximity to a specimen's surface, typically of several Å, and a potential is applied on either the tip or the specimen. A slight change in the tip-specimen distance exponentially affects the magnitude of the tunneling current, usually with a ratio of about one order of magnitude per Å. Due to this extremely high sensitivity, the tunneling current is used to accurately control the tip-surface separation distance by means of a feedback circuit. In the so called "constant current" scanning mode, for a given tunneling current (the feedback current) and a bias voltage, a certain **z** position is accommodated. In this way, a constant charge density contour of the surface is obtained.

The tip is driven along the **x, y** and **z** axis by a single tube, or a tripod scanner (schematically depicted in Fig. 2.6 for an easier description of the scanning mechanism).
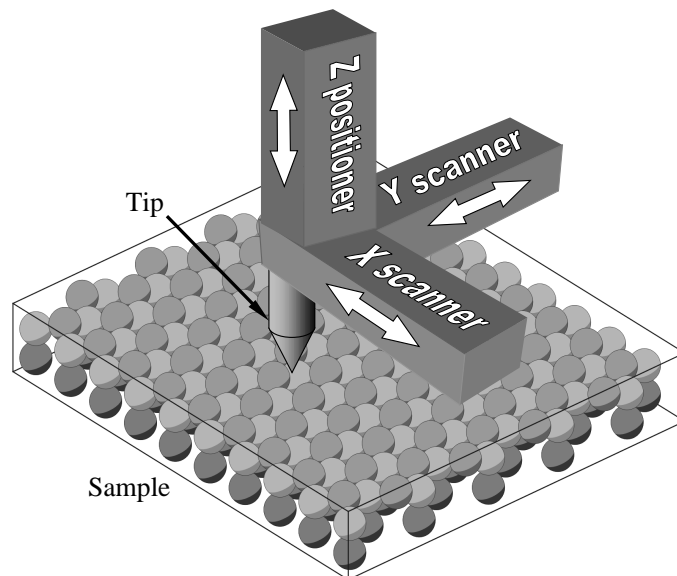
Figure 2.6: A schematic drawing of the tripod STM scanner driving the tip over a specimen surface.

The latter is mainly build up from three orthogonal bars made out of materials showing a high piezoelectric constant. The tip is moved over the sample in the desired direction by applying a voltage on the corresponding piezoelectric element. In the microscope used in this work (*Omicron VT-STM*), a single tube scanner was employed. This has the advantage of a higher resonance frequency than a tripod scanner, but at the same time it has a stronger tendency toward a crosstalk between the orthogonal piezoelectric effects.

If one considers now the energy of the electrons involved in the surface imaging, typi-

cally of few eV, the immediate question arising is how the atomic resolution images can be obtained, while the electron's de Broglie wavelengths are ≈ 12 Å, higher than the typical interatomic distances (≈ 3 Å). This apparent contradiction is straightforwardly resolved by taking into account that the STM operates in the near-field regime, *i.e.*, at tip-surface distances smaller than the electron's de Broglie wavelength. Therefore, the spatial resolution of this technique is no longer diffraction limited. In addition, by invoking the scanner capabilities, one can achieve accurate information about the surface at both nano- and micro-scale.

To determine the tunneling current, or the transmission probability (it decays exponentially with barrier width), in a certain tunneling barrier geometry, one has to solve the corresponding Schrödinder equation with the appropriate boundary conditions. If in the simple case of a unidimensional rectangular barrier an exact solution can be easily found, in the real three dimensional case of an irregular shape barrier the derivation of an exact solution is far from trivial. A relatively simple expression for the transmission was found by García *et al.* [41], but their calculation appears to be unfeasible in the case of a real surface. Since the tip-surface coupling is weak, the first-order perturbation theory can be applied to get a more realistic picture. Under this approach, the current is given by

$$I = \frac{2\pi e}{\hbar} \sum_{m,n} [f(E_m) - f(E_n)] |M_{m,n}|^2 \delta(E_n + V - E_m) \tag{2.8}$$

where $f(E)$ is the Fermi function, $\hbar$ the Planck's constant, V the applied tip-specimen voltage, $M_{m,n}$ the tunneling matrix element between the states Ψ_m and Ψ_n of the respective electrodes, with E_m and E_n the energies of the Ψ_m and Ψ_n, respectively. The difficulty arises from the evaluation of the tunneling matrix elements $M_{m,n}$, which can be written as an integral over any surface inside the barrier region [42]:

$$M_{m,n} = \frac{\hbar}{2m} \int (\Psi_m^\star \nabla \Psi_n - \Psi_n \nabla \Psi_m^\star) d\mathbf{S}. \tag{2.9}$$

where m is the electron mass. The above expression further simplifies into

$$M_{m,n} = -\frac{4\pi^2 \hbar^2}{m} \int a_q b_q^\star \kappa_q e^{-\kappa_q z} e^{i\mathbf{q}\mathbf{X}_t} d\mathbf{q} \tag{2.10}$$

by Fourier expanding the corresponding wavefunctions into planewaves. Here, a_q and b_q are the coefficients of the Fourier expansion of Ψ_m and Ψ_n, respectively, $\mathbf{q}$ is the Fourier wavevector (spatial frequency), with $\mathbf{x}_t$ and z_t the lateral and vertical components,

respectively, of the tip position. κ_q is given by $\kappa^2 + |\mathbf{q}|^2$ where $\kappa^2 = 2m(E_n + V - E_m)/\hbar^2$. However, in reality it is difficult to accurately compute the tunneling current, since the exact atomic structure of the tip is unknown. An ideal point tip geometry [43] has been considered for calculations of the tunneling current in the low voltage regime yielding a direct proportionality with the local density of states (LDOS) at the Fermi level, E_F: $\rho(\mathbf{r}_t, E_F)$. By means of an s-like wavefunction of the tip, the STM images were directly associated with the surface topography for free-electron metal substrates [44]. In the case of the semiconductor surfaces, the above approaches are not straightforward, for the LDOS at E_F is strongly influenced by the applied voltage: $\rho(\mathbf{r}, E_F) \longrightarrow \rho(\mathbf{r}, E_F + V)$ Therefore, the exact proportionality does not hold anymore, except for very low voltages. In addition, $\rho(\mathbf{r}, E_F + V)$ changes discontinuously at the band edges, and the STM images reflect the spatial distribution of the valence and conduction wavefunctions, according to the applied tip-specimen polarity, respectively. Therefore, by tuning the bias voltage, both empty and fill state STM images can be visualized.

2.4   Linear magneto-optic Kerr effect

In this section, the magneto-optic Kerr effect (MOKE), a powerful tool to probe *in-situ* the magnetic properties of the ultra-thin films, will be addressed. The effect, discovered by Kerr in 1876, manifests by the change of the state of polarization and/or intensity of an incident electromagnetic radiation upon reflection from a magnetized material. It is the analogous of the effect discovered in 1845 by Faraday who observed for the first time this phenomena for a transmitted radiation through a magnetized medium. Macroscopically, the effect can be assessed by means of the dielectric ("refractive") tensor of a medium [45], or, equivalently, by considering two different complex indices of refraction in a magnetized medium for the left- and right-circularly polarized light. Let us consider a linearly polarized light beam, which can be described as the sum of a left and a right polarized one, impinging on such medium. Upon the reflection, a phase shift (*circular birefringence*) is introduced between the two components, which in turn are differently absorbed (*circular dichroism*) by the medium. These two phenomena manifest in the reflected light by a rotation of the polarization axis and a conversion of the linear polarization state into an elliptic one.

The microscopic mechanism can be described in terms of the spin-orbit coupling between the spin components of the (spin-polarized) electron wavefunctions and the spatial

components which rule the electric dipole transitions between the Zeeman split states [45]. This approach is based on the early calculations of different refraction indices for the left- and right-circularly polarized light while taking into account the spin-orbit interaction [46]. By introducing the spin-orbit and electron-electromagnetic field interaction terms into the one-electron Schroedinger equation, Argyres [45] found the following expression for the average macroscopical total current density:

$$\mathbf{J}_{total} = \sigma \cdot \mathbf{E} + \alpha \cdot \frac{\partial \mathbf{E}}{\partial t} \tag{2.11}$$

where $\mathbf{E}$ is the electric field of the electromagnetic radiation. Here, σ and α are the complex conductivity and polarizability tensors, respectively, which take the following nondiagonal form in the case of a cubic specimen magnetized uniformly along $\mathbf{z}$:

$$\sigma = \begin{pmatrix} \sigma_{xx} & \sigma_{xy} & 0 \\ -\sigma_{yx} & \sigma_{yy} & 0 \\ 0 & 0 & \sigma_{zz} \end{pmatrix}, \; \alpha = \begin{pmatrix} \alpha_{xx0} & \alpha_{xy} & 0 \\ -\alpha_{yx} & \alpha_{yy} & 0 \\ 0 & 0 & \alpha_{zz} \end{pmatrix} \tag{2.12}$$

where the diagonal terms are independent of the magnetization, $\mathbf{M}$, to the first order (even function of $\mathbf{M}$), while the off-diagonal terms are linear dependent to $\mathbf{M}$ to the first order (odd functions of $\mathbf{M}$). The same matrices can be written down in the case of a perpendicularly magnetized film, while for an in-plane magnetized film, one obtains

$$\sigma = \begin{pmatrix} \sigma_{xx} & 0 & \sigma_{xz} \\ 0 & \sigma_{yy} & 0 \\ -\sigma_{zx} & 0 & \sigma_{zz} \end{pmatrix}, \; \alpha = \begin{pmatrix} \alpha_{xx} & 0 & \alpha_{xz} \\ 0 & \alpha_{yy} & 0 \\ -\alpha_{zx} & 0 & \alpha_{zz} \end{pmatrix} \tag{2.13}$$

Now, if the average macroscopical total current density (2.11) is inserted into the Maxwell equations, and monochromatic plane wave solutions are chosen for the electric and magnetic fields, the Kerr rotation and ellipticity are given by the imaginary and real part of the same quantity, respectively, as follows:

$$\rho = -\Im \left(\frac{N_+ - N_-}{N_+ N_- - 1} \right) \tag{2.14}$$

$$\epsilon = -\Re \left(\frac{N_+ - N_-}{N_+ N_- - 1} \right) \tag{2.15}$$

under the assumption of normal incidence and for $N_+ - N_- \ll N_+$ or N_-. The quantities N_+ and N_- stand for the complex indices of refraction for the right- and left-circularly

polarized light, respectively, and their square are linearly dependent on the components of the conductivity and polarizability tensors.

In the MOKE experiments, three measurement geometries can be distinguished, according to the relative orientation between the magnetization direction and the specimen's surface. The magnetization is perpendicular to the surface in the polar geometry, lies in both the surface and incidence plane in the longitudinal geometry (the one used in this work and sketched in Fig. 2.7) and lies into the surface plane and perpendicular to the
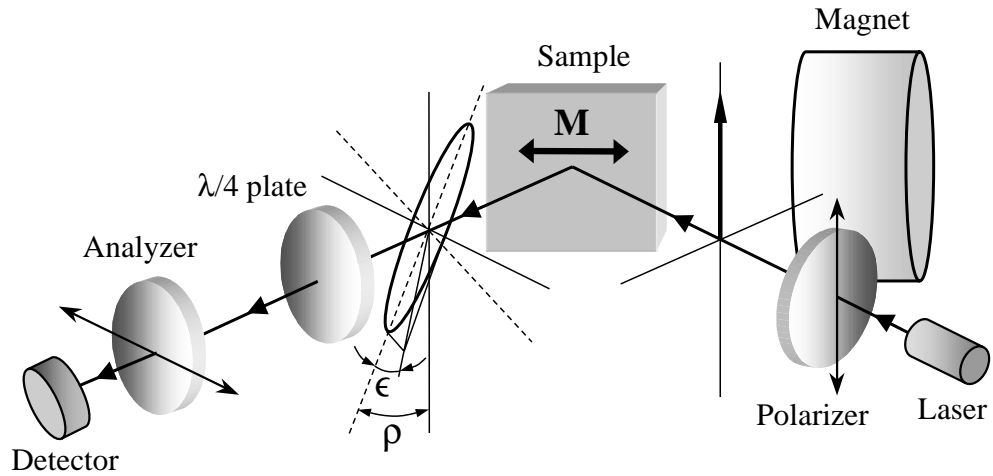
Figure 2.7: A sketch of the longitudinal MOKE set-up. The incident s-polarized light is converted into an elliptically polarized one upon the reflection on the magnetized specimen.

incidence plane in the transversal geometry. The actual values of the Kerr rotation and ellipticity can easily be found for a given geometry in the case of a linearly polarized light (s in the experimental set-up used here), by decomposing it into the right- and left-circularly polarized components, and evaluating the reflection coefficients r_p, r_{ps}, r_{sp} and r_s [47], where s and p stand for the polarization direction perpendicular and parallel to the incidence plane, respectively. In the thin-film limit, *i.e.*, $2\pi d |N|/\lambda \ll 1$ [47], with d the thickness of a film of complex refractive index N and λ the light wavelength, the reflection coefficients are given by:

$$\phi_s = \frac{r_{ps}}{r_{ss}} = \rho + i\epsilon \ and \ \phi_p = \frac{r_{sp}}{r_{pp}} = -\rho + i\epsilon \qquad (2.16)$$

where ϕ_s and ϕ_p are the complex Kerr rotations for the corresponding directions of polarization. Accordingly, the following expression for the rotation can be derived,

$$\rho = \frac{1}{2}\alpha\frac{I - I_b}{I_b - I_d} \qquad (2.17)$$

where the quantities I, I_d and I_b stand for the total transmitted intensity for an angle between the analyzer and the p direction (*skew angle*) of α, the transmitted intensity for crossed polarizer and analyzer (*extinction*) and the background intensity, respectively. An identical formula is found for the ellipticity, provided that a $\lambda/4$ retardation plate is inserted between the sample and analyzer (Fig. 2.7). The retardation plate introduces a corresponding phase shift between the right- and left-circularly polarized components, interchanging the real and imaginary parts in the complex rotation of the reflected beam. Therefore, one can conclude that detailed information about the magnetization state of a specimen surface can be obtained by embedding the magneto-optic Kerr effect into a powerful investigation technique.

In the set-up used in this work, a unipolar magnet piece is brought close to the sample, whose axis makes a non-zero angle with respect to the sample's surface. Therefore, also the perpendicular magnetization can be detected, since it gives a signal about one order of magnitude higher than the in-plane magnetization. The maximum DC magnetic field reachable with this setup does not exceed 30 mT.

Chapter 3

Fe on Si(001)

In this chapter, after an account on the main aspects concerning the growth and magnetic properties of thin Fe films on Si(001), an alternative way to reduce the Fe-Si intermixing by means of a Au passivating layer is presented. With this passivation, a drastic change in substrate morphology and the growth of smooth Fe films with appealing magnetic properties were observed.

Several studies of the reaction of Fe grown on Si(001) have been carried out in the past decade [11,12], but special attention was paid to the investigation of direct band-gap [13] semiconducting iron disilicide [14–16] for its possible use as near infrared light sources and detectors. In the case of room temperature deposited Fe, amorphous Fe_3Si was found to form at the interface [17], possibly harmful for spin-injection applications.

In the attempt to reduce intermixing at the interface, S, Se or B passivation were used [18, 19] giving rise to a rougher surface and it is not clearly established to which extent these can prevent silicide formation. A recent investigation of Fe films grown on S-passivated Ge showed no reduction in the magnetization onset coverage and brought evidence for S migration to the surface of the growing film during deposition [48]. The segregation of the passivation agent on the top of the film may reduce the passivation and contaminate the Fe film. Bertoncini *et al.* [49] investigated an alternative passivation which can be achieved by the growth of ≈10 ML thick $CoSi_2$ film on Si(001) prior to the Fe deposition. They reported a reduced Si migration and the growth of good epitaxial bcc Fe films.

3.1 Substrate preparation

Small pieces ($\approx 10 \times 2 \times 0.5$ mm^3) cut from commercially available p-type Si(001) wafers ($\rho \approx 5$ Ωcm) have been used as substrates. Prior to their mounting into Ni contaminant free holders and inserting into the ultra high vacuum (UHV), the crystals were ultrasonically cleaned and then boiled for several minutes in absolute pure ethanol. After transferring them into the UHV chambers via the load lock system, the samples were firstly outgassed by slightly rising the temperature to about 900 K, so that the pressure did not exceed 5×10^{-9} mbar. Once the pressure went down to several 10^{-10} mbar, short flashes up to $\approx$1600 K were given to remove the native oxide layer. Special attention was paid to keep the maximum pressure in the low 10^{-9} mbar range. Both outgassing and flashing were performed by direct heating, carefully observing the sample temperature with an optical pyrometer. The substrates were considered clean only after the dimer rows of the reconstructed surface were clearly seen in STM scans, as discussed in the next section. The absence of any traces of carbon and oxygen in the Auger spectra along with a sharp two domain (2×1) LEED pattern with low background (see the next section) indicated also a clean sample.

3.2 The (001) surface of Si

Silicon shows the same crystal structure as carbon, namely the diamond structure, depicted in Fig 3.1(a). It can be regarded as two interpenetrating face-centered-cubic sublattices displaced with respect to each other by one quarter of the body diagonal. The lattice constant is 5.43 Å, and the closest coordination shell of each atom consists of four atoms situated in the corners of a regular tetrahedron. Every atom in a (001) plane forms covalent bonds to two atoms in the underneath (001) plane toward one of the $< 110 >$ directions, and to another two atoms in the above (001) plane toward the other $< 110 >$ direction. It is worth underlining here that all $< 110 >$ symmetry axes are equivalent in the diamond structure.

Let us now imagine that the Si crystal is cut normal to the [001] direction and a bulk terminated (001) surface is obtained (Fig. 3.1(b)). The unreconstructed surface, denominated as (1×1) with the unit mesh of 3.84×3.84 Å^2, is unstable, since each atom on it has two broken bonds, called dangling bonds (half filled orbitals) protruding out of the surface and (predominantly) oriented along one of the $< 110 >$ axis ($[\bar{1}10]$ in Fig. 3.1(b),
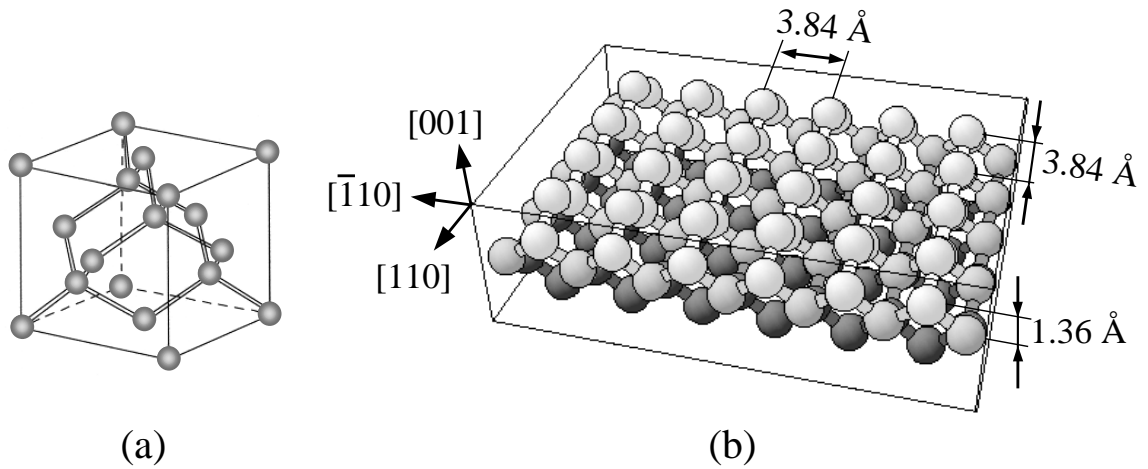
Figure 3.1: (a): Diamond structure, and (b): the unreconstructed Si(001) surface.

but not shown for the sake of simplicity). In the real life, due to the limited precision in cutting and polishing a single crystal along a certain direction, a misorientation of the order of 0.5° occurs. Accordingly, steps between (001) oriented terraces are introduced to accommodate this misorientation. This is shown in the STM image in Fig. 3.2(a), which
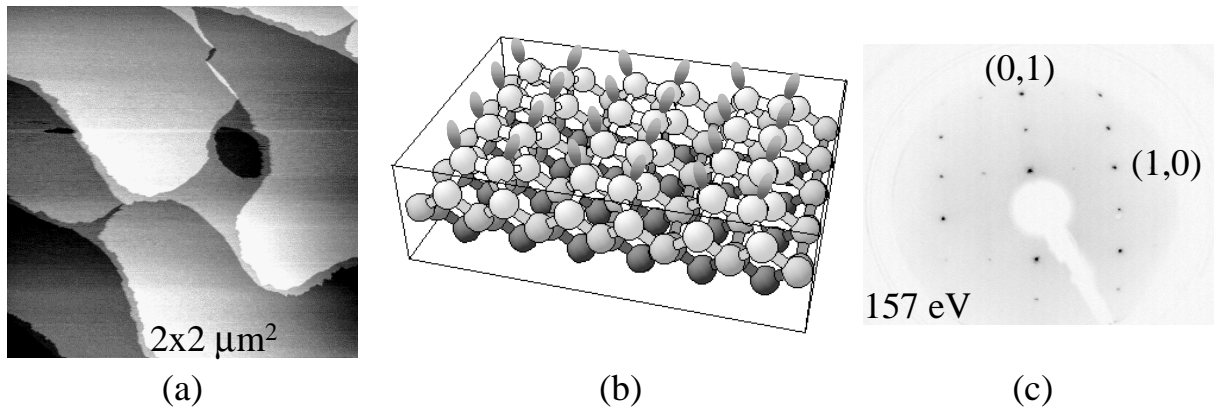
Figure 3.2: (a): STM image of a clean Si(001) surface taken at -1.6 V bias voltage and 1.0 nA constant current, (b): a three-dimensional representation of the (2×1) reconstruction with the remaining dangling bonds, and (c): LEED pattern of the two domain (2×1) reconstruction of Si(001) taken at 157 eV.

corresponds to one of the substrates used in this work, all of them cut from the same wafer along the $< 110 >$ directions. The terraces' average width is inversely proportional to the miscut angle and on the local roughness of the surface, ranging between tens and

hundreds of nm. The steps are usually monoatomic, *i.e.*, 1.36 Å high (single steps), but double steps may also occasionally occur.

To obtain a more favorable configuration, the number of the dangling bonds has to be decreased. This is achieved by pairing two dangling bonds of two neighboring surface atoms along, *e.g.* [$\bar{1}10$] in Fig. 3.1(b), resulting in the formation of a covalent bond dimer. This is schematically shown in the three dimensional representation in Fig. 3.2(b). Consequently, the paired atoms move slightly towards each other, and the surface unit cell is enlarged along the dimerisation direction by a factor of two. In this way, the (2×1) reconstruction [50] associated with the occurrence of the half order spots in the LEED pattern is built, and the number of dangling bonds is reduced by a factor of two. On terraces separated by a monoatomic step, the dimerisation is realized in directions perpendicular to each other for bond symmetry reasons of the diamond structure. Therefore, two (2×1) configurations coexist on the surface, as observed by LEED (Fig. 3.2(c)) and STM (Fig. 3.3(a)) on the substrates used in this study. The dimerised atoms are arranged

(a)   (b)   (c)
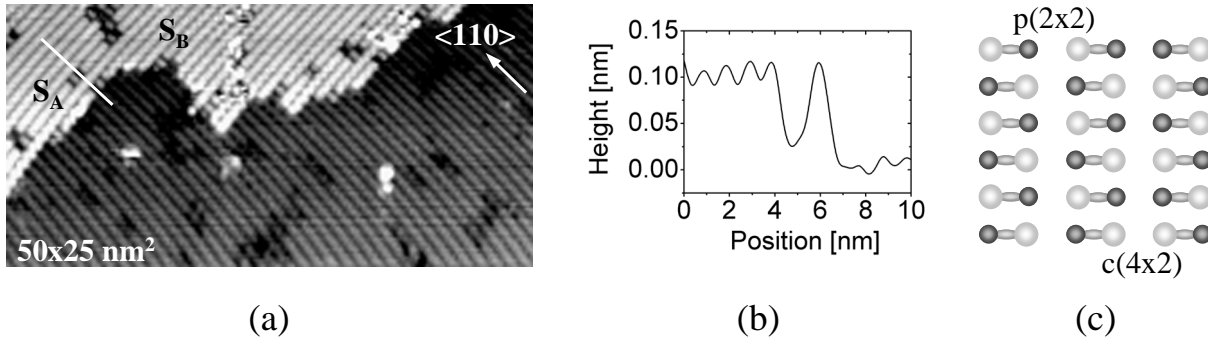
Figure 3.3: (a): 50×25 nm^2 STM image of the reconstructed Si(001) surface taken at a bias voltage of -1.6 V and a constant tunneling current of 0.3 nA. The line scan in (b) is taken along the direction marked in (a), across several dimer rows and over the step edge. A schematic drawing of the p(2×2) and c(4×2) reconstructions responsible for the zig-zag appearance of some rows in (a) are shown in (c).

in parallel and equally spaced rows (Fig. 3.3(b)) running along the < 110 > directions, either parallel or perpendicular to the downward step edge, as one can see in the STM image in Fig. 3.3(a). These two distinct step configurations are denoted as S_A and S_B steps, respectively [51]. They do not necessarily correspond to different physical steps: for the steps follow a rather irregular trajectory in the case of a low miscut angle (Fig. 3.2(a)), S_A and S_B steps occur on the same physical step, as marked in Fig. 3.3(a). Defects are always

present on the surface and, beside the occurrence of the monoatomic steps (Fig. 3.3(b)), also the so called "split off dimer" defects [52] can be seen on the substrates used here (the dark rectangles along the rows containing one dimer in Fig. 3.3(a)). This type of defect is associated with the presence of contaminant Ni and consists of a missing dimer, the "split off dimer" itself and another two adjacent missing dimers. The line scan in Fig. 3.3(b) is taken over such defects.

In addition to the (2×1) surface phase, higher order reconstructions, namely the p(2×2) and c(4×2) [53,54], are found on the clean Si(001) surface. Earlier, it was claimed that the introduction of these phases induces a rise in the surface energy with such a small quantity that approaches the limits of computation accuracy [55]. More recent first principle calculations [56] and the observation of an increased number of buckled dimers at low temperatures [57] proved that the surface equilibrium state consists of the high order phases as in the case of Ge(001) [58]. These reconstructions, schematically shown in Fig. 3.3(c), are obtained by tilting the dimers with respect to the surface plane as the result of charge transfer from one dangling bond of the dimer to the other. Neighboring dimers in the same row usually buckle in opposite directions giving rise to the zig-zag appearance of some rows, as observed also here (Fig. 3.3(a)). If the dimers in the adjacent rows buckle in-phase, the p(2×2) reconstruction is obtained, while the out-of-phase buckling is responsible for the occurrence of the c(4×2) one (Fig. 3.3(c)). These high order reconstructions coexist with the (2×1) phase associated with unbuckled areas which, in fact, is believed to flip so fast, that the STM only "sees" the time-averaged position of the dimers [57, 59].

3.3 Fe grown on (2×1) Si(001)

3.3.1 Growth investigation

The growth of Fe on Si(001) at various temperatures by molecular beam epitaxy has been abundantly investigated with several techniques by various groups. Therefore, only a brief discussion of the STM results obtained in this study will be given. Previous studies showed that the Fe/Si interface at room temperature (RT) is far from being sharp. A ferromagnetic amorphous phase [60] with the stoichiometry close to Fe_3Si starts to form after ≈ 1 monolayer (ML) of Fe is deposited [17]. Adams *et al.* [61] found that in the submonolayer Fe growth stage, the average cluster size does not show a conspicuous

coverage dependence in the MBE growth, but enlarges with increasing the amount of deposited Fe by chemical vapor deposition (CVD), while no clear temperature dependence was observed regardless of the growth method. Up to a coverage of 1 ML, a layer-by-layer growth mode was suggested by Gallego *et al.* [17], as they deduced from the coverage dependence of the low energy Fe_{MNN} and Si_{LMM} Auger lines. With increasing the film thickness above 1 ML, no LEED pattern could be seen any longer [12–17,60]. The Fe-Si reaction was shown to slow down above 5 ML [17], to end abruptly at 10 ML [60], with the beginning of *bcc* Fe formation.

Since the magnetic behavior is a matter of concern in this work, it is useful to follow the film morphology at that particular thickness which corresponds to the onset of the long range ferromagnetic order. However, in the case of disordered films, relevant changes in some of the physical quantities can hardly be associated with visible transformations in the morphology. For slightly less than 4 ML of Fe deposited at RT on Si(001), small coalesced islands are observed in the STM scans (Fig. 3.4(a)). This film thickness will be shown
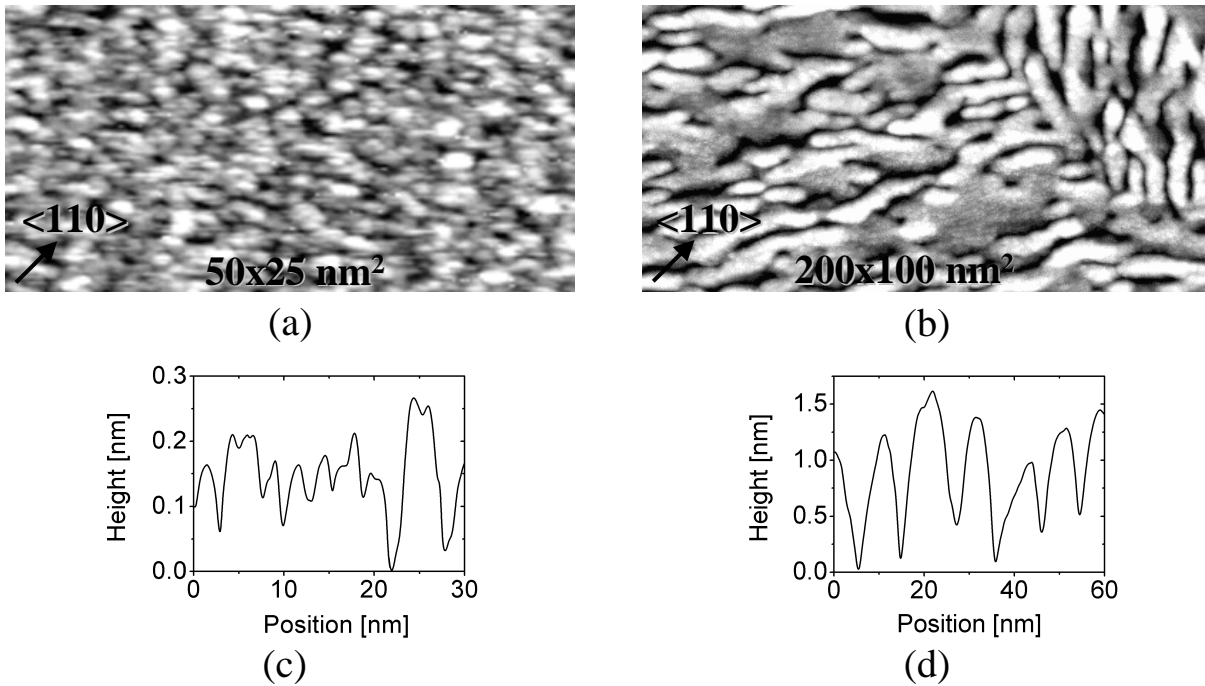
Figure 3.4: STM images of slightly less than 4 ML, (a), and ≈20 ML of Fe, (b), grown on Si(001) at RT. The scans in (a) and (b) were performed at -1.6 V bias voltage/0.56 nA constant current and 0.8 V/0.1 nA, respectively. Corresponding line profiles are shown in (c) and (d), respectively.

in the next section to stand for the occurrence of magnetic signal in the magneto-optic Kerr effect (MOKE) measurements. As revealed by the line scan shown in Fig. 3.4(c), the corrugation is rather low, with no more than three layers being exposed. It seems that, at least up to this coverage, the growth of a rather smooth film is favored by the reaction between the deposited Fe and the Si(001) substrate. By further increasing the Fe coverage up to ≈20 ML, the morphology is characterized by elongated islands (Fig. 3.4(b)) and a much higher corrugation is noticed (Fig. 3.4(d)).

3.3.2   Magnetic properties

A long-range in-plane ferromagnetic order in the silicide films was shown by different authors to set in after the deposition of about 4 ML of Fe at RT [60, 62], with a reduced magnetization in comparison to the one of bcc Fe [60].

In this work, the magnetization was probed by MOKE in longitudinal geometry with the magnetic field oriented along $< 110 >$. For the whole thickness range investigated (up to ≈20 ML), the magnetization was always found to lie in the film plane and no measurable magnetic anisotropy was observed. For films grown at RT, the first in-plane hysteresis loops were detected after about 3.6 ML of Fe were deposited. By increasing the amount of deposited Fe, a smoothly increasing MOKE signal was measured (Fig. 3.5(a)), except for Fe coverages between 9 and 12 ML.
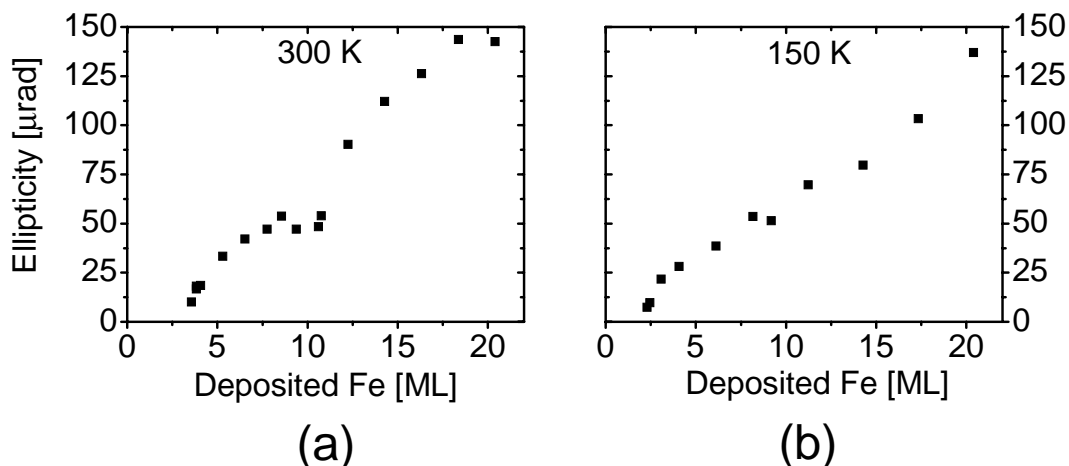
Figure 3.5: MOKE ellipticity in longitudinal geometry at saturation *vs.* the amount of deposited Fe on (2×1) Si(001) at: (a), room temperature (≈300 K), and (b), ≈150 K.

Recent spin-integrated and spin-resolved photoemission studies performed by Kläsges

et al. [60] showed that the silicide formation ends abruptly at 10 ML. This is roughly where a kink in the MOKE signal is observed in this study (see Fig. 3.5(a)), which is assigned to changes in magnetic moment, structure and/or chemical modifications at the growth front. The late onset of magnetization observed in RT grown films might be correlated to the weak ferromagnetism of the amorphous silicide film and to an intermixed interface. To reduce the thermally activated silicide formation, the growth temperature was reduced down to ≈150 K. This induces an earlier onset of the in-plane magnetization at slightly below 2.5 ML as shown in Fig. 3.5(b). No perpendicular orientation of the magnetic moment was observed, as earlier reported for Fe grown at 100 K on Si(001) [62] probably because the growth temperature in the experiments performed in this study was higher. The early onset of magnetization observed here at 150 K might be put on the expense of the low growth temperature, or to the low measuring temperature. Since a ≈2.5 ML thick Fe film grown at RT showed no magnetic signal at both RT and 150 K, one may conclude that the reduced intermixing at low growth temperatures is at least partly responsible for the early onset of magnetization. Additionally, the kink at about 10 ML of Fe in the MOKE ellipticity at saturation *vs.* the amount of deposited Fe shown in Fig. 3.5(b) is not as well defined as in the RT growth case (Fig. 3.5(a)). This finding might be associated with a reduced intermixing, in agreement with the observation of Kläsges *et al.* [60] who detected a smooth change in the photoemission spectra with Fe thickness at 100 K. However, the early onset of magnetization is not accompanied by a significantly larger Kerr signal in comparison to the RT growth. This points at only a minor reduction of intermixing at 150 K.

3.4   Au-passivated Si(001)

In the attempt to suppress the silicide formation, a thermodynamically stable passivation of the (2×1) Si(001) was employed in this study, as described in the following. By the deposition of slightly less than 1 ML of Au at temperatures of the order of 1000 K, the typical two-domain (2×1) LEED pattern of clean Si(001) (Fig. 3.2(c)) transforms into complex ones (Fig. 3.6) due to a complete surface restructuring. By comparing the LEED patterns in Fig. 3.6, one can conclude that relatively small variations in the deposition temperature leads to the formation of different surface structures, in agreement with the early work of Oura *et al.* [23]. Moreover, the different surface reconstructions are accompanied by different topographs, as one can deduce from the STM images in Fig. 3.7.

1000 K **95 eV**

(1,0) (0,0)

(0,1)

(a)

1100 K **78 eV**

(1,0) (0,0)

(0,1)

(b)
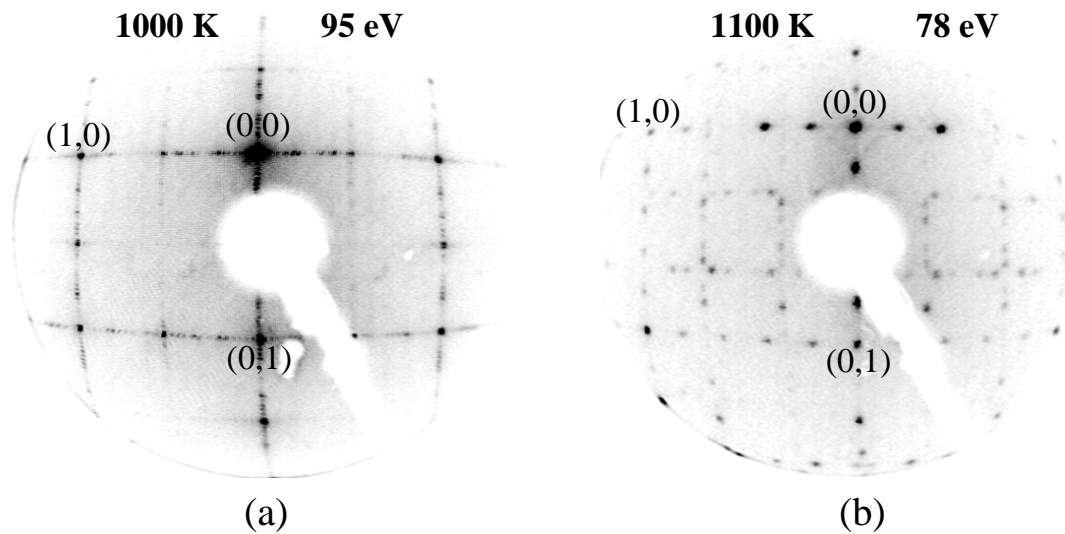
Figure 3.6: LEED patterns of $\approx$1 ML of Au deposited on Si(001) at (a) 1000 K, and (b) 1100 K. The images were taken at beam energies of (a) 95 eV, and (b) 78 eV.

The deposition conditions have to be carefully tuned to realize a complete reconstruction and to avoid the formation of Au crystallites. Such tiny crystallites uniformly littered throughout the surface, which occur as the result of Au deposited in excess, are clearly seen in the STM topograph in Fig. 3.7(b).

The images shown in Fig. 3.7(a)-(c) correspond to the similar amount of deposited Au, but at different substrate temperatures, ranging from $\approx$900 K in (a) to $\approx$1100 K in (c). Such differences in the deposition temperature lead to different topographs as the result of different surface diffusion lengths. The most striking feature which macroscopically characterizes the reconstructed surface obtained here is the overall rectangular-like appearance of the terraces (compare with Fig. 3.2(a)), especially for deposition temperatures of about 1100 K (Fig. 3.7(c)). If the deposition temperature is low, defects like missing dimers do not gain enough energy to form regular trenches [63], but appear to gather and form elongated dark features, while the steps become ragged. This situation is captured in the STM image shown in Fig. 3.7(a). The line scans depicted in Fig. 3.7(d)-(f) give valuable information about the step height in the corresponding STM topographs. If in the case of a Au deposition temperature of about 900 K mainly single atomic steps of $\approx$1.5 Å height are observed (Fig. 3.7(d)), by increasing the substrate temperature to *e.g.* $\approx$1100 K, bi- and tri-atomic steps develop (Fig. 3.7(f)). These kind of steps can also be seen in Fig. 3.7(b) by simply following the gray tones of the terraces.
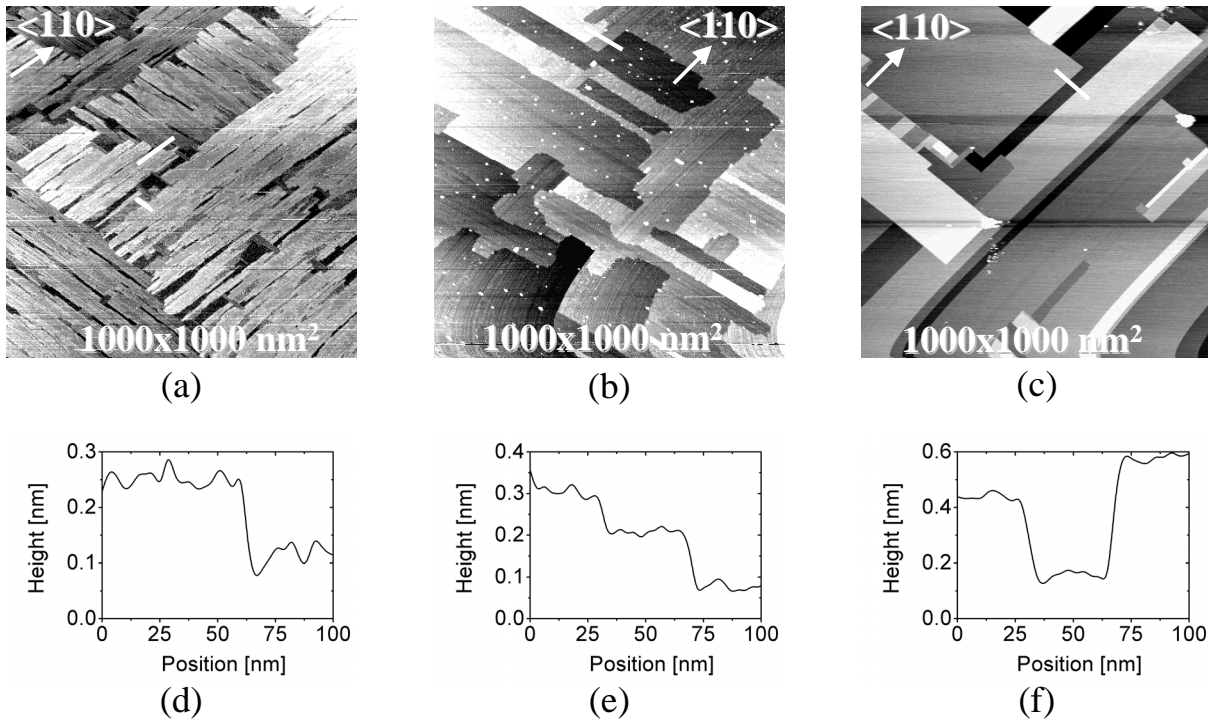
Figure 3.7: Large area STM topographs of Au-induced reconstructed Si(001) taken at 1.6 V bias voltage and a constant tunneling current of 1.0 nA, (a) and (b), and 0.5 nA, (c). Au was deposited at different substrate temperatures, increasing from (a) to (c). The profiles in (d), (e) and (f) were taken over the steps marked with white lines in the corresponding STM topographs.

3.5 Fe grown on Au-covered Si(001)

3.5.1 Growth investigation

After the Au-induced reconstruction was performed as described above, Fe films were initially grown at RT directly on such surfaces. As in the case of growth on (2×1) Si(001), no LEED pattern could be seen any longer for deposited Fe in excess of about 1 ML, suggesting a high degree of disorder in the film. Small islands form in the incipient growth stages, and some of the bright stripes characteristic to the underlying reconstructed surface are clearly visible at least up to 2 ML of deposited Fe at RT, as one can see in the STM image in Fig. 3.8(a). The brightest spots in Fig. 3.8(a), except for the features on the reconstruction stripes, are 2 ML tall islands (see the line profile in Fig. 3.8(a)), while most of the islands are 1 ML high. The film is smooth, but a layer-by-layer growth is not
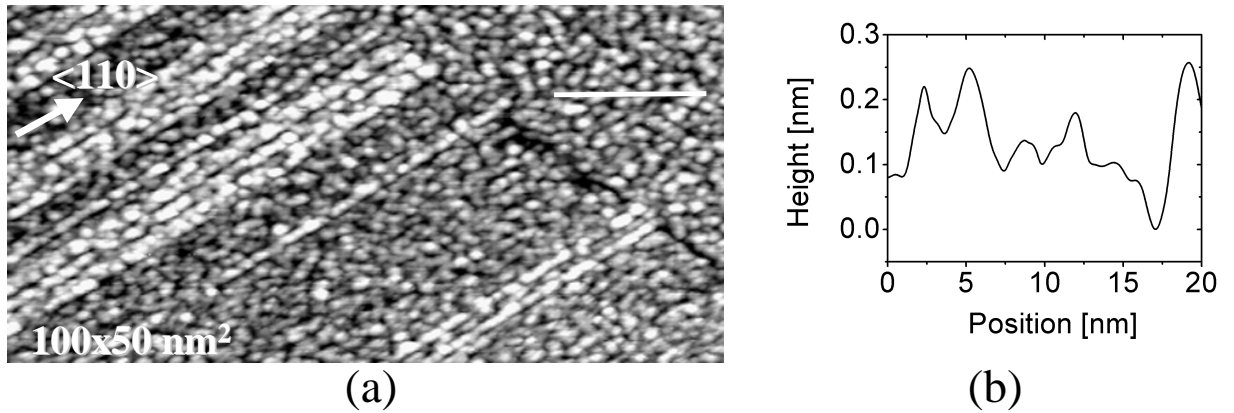
Figure 3.8: (a): 100×50 nm^2 STM image of slightly less than 2 ML of Fe deposited at RT on Au-induced reconstructed Si(001), and (b): a corresponding line profile taken along the white line over a group of islands. The scan was performed at -1.6 V bias voltage and a constant tunneling current of 0.56 nA.

inferred. It roughens slightly with increasing the coverage, while the overall reconstruction features persist. For an approximately 12 ML thick Fe film deposited at RT, the typical topography of the Au-induced reconstructed surface is clearly preserved (Fig. 3.9(a)) and only 4 layers are exposed, as one can deduce from the line profile in Fig. 3.9(b). To rule on the thermal stability of the underlying reconstruction in the presence of an Fe film which is known to strongly react with the bare substrate [11,15–17,60], a very short and mild annealing up to about 400 K was performed. In this experiment, the annealing temperature was chosen so that no reduction in the magnetic signal was observed, and only a decrease in the coercive field was measured by MOKE, as it will be discussed in the next section. The rectangular step-terrace configuration of the underlaying reconstruction is preserved upon annealing, while the size of the islands is increased and became decorated with elongated details (Fig. 3.9(c)). Most likely, the appearance of such elongated features might represent a fingerprint of an enhanced Si out-diffusion into the Fe film triggered by rising temperature. However, the intermixing is not strong since it does not lead to a reduced magnetic signal, as mentioned above, but the peak-to-peak roughness is apparently increased (Fig. 3.9(d)), and the average island size became larger due to the temperature driven coalescence. The observed change in corrugation might be just a scanning artifact in the sense that the depth of the narrow space between the small islands prior to the annealing is not correctly accounted for.

(a)

(c)

(b)

(d)
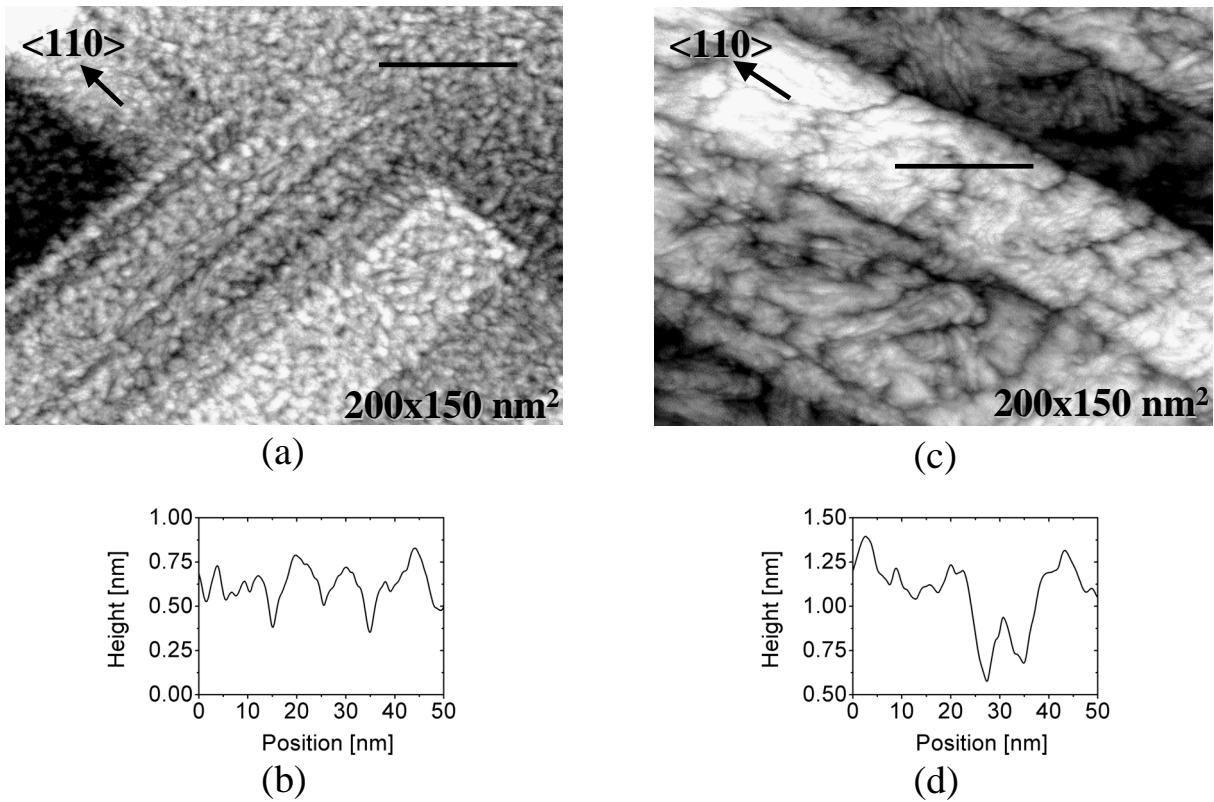
Figure 3.9: (a): STM image of $\approx$12 ML of Fe deposited at RT on Au-induced reconstructed Si(001), along with a profile, (b), taken along the black line in (a). The STM image in (c) was recorded after a short and mild annealing up to about 400 K, and the profile in (d) was taken along the black line in (c). The 200$\times$150 nm^2 scans in (a) and (c) were performed at -1.6 V bias voltage and a constant tunneling current of 0.5 nA.

In the attempt to inhibit the diffusion of silicon into the Fe layer even at the ambient temperatures, about 1.5 ML of Au was further added on the Au-induced reconstructed surface of Si(001) at RT, or LT ($\approx$150 K), as a buffer layer. In both cases, the LEED pattern of the reconstructed surface is completely wiped out upon the growth of the buffer layer. Furthermore, no difference between the film morphologies corresponding to the two growth temperatures was observed in the STM images (all of the STM scans in this work were taken at RT). The morphology of such Au buffer layers grown at LT is shown in Fig. 3.10(a). Due to their high mobility, the Au adatoms coalesce into small 1 and 2 ML high islands as one can see from the line profile in Fig. 3.10(b) (the lattice constant of fcc Au is 4.08 Å). Accordingly, small areas which were not covered with Au still exist and
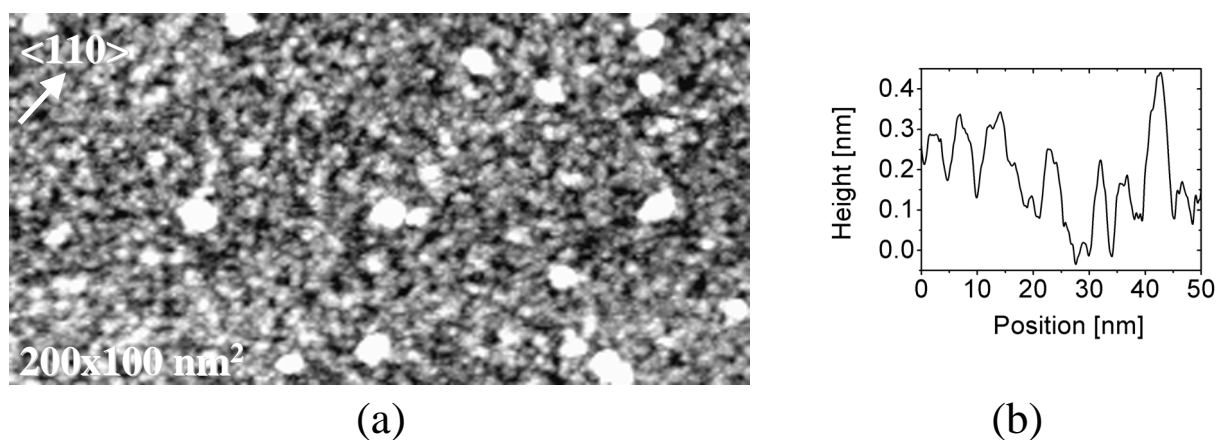
Figure 3.10: 200×100 nm^2 STM image of ≈1.5 ML thick Au film deposited at LT on Au-induced reconstructed Si(001), taken at 1.6 V bias voltage and a constant tunneling current of 1.0 nA, (a), along with a line profile, (b).

may act as channels for Si outdiffusion. It is not clear whether the observed roughness is the result of annealing the sample up to RT where the STM scans were performed, or the buffer layer grows indeed as 3D islands from the very beginning even at LT. Certainly, in the RT growth case, the tendency toward droplet formation due to high Au mobility does not favor the growth of a smooth film, and consequently its role as a buffer layer is not fully achieved. Moreover, the lower surface free energy of Au with respect to that of Fe is responsible for the segregation of a single Au capping layer as reported earlier [64]. This would, in the worst case, leave roughly only 0.5 ML of Au together with about 0.6 ML of Au involved in the reconstruction [65] to limit the Fe-Si intermixing.

Hereafter, attention was paid to the growth of both Au and Fe films at reduced temperatures in the hypothesis that a smoother, and therefore efficient Au passivating layer can be obtained, on one hand, and the temperature driven Si outdiffusion can be reduced, on the other hand. The buffered Au-induced reconstructed surface will be denominated as Au-covered surface, for short.

The stripes belonging to the Au-induced reconstructed surface are still visible after about 2.5 ML of Fe were grown at LT on Au-covered Si(001) (Fig. 3.11(a)). As one can deduce from a comparison between the line profiles in Fig. 3.10(b) and Fig. 3.11(b), the deposition of Fe does not result in the growth of a rougher film. On contrary, it seems that the asperities visible in the Au-buffer layer were flattened and somewhat larger islands are observed. Some Au deposited in excess while the reconstruction was

(a)   (c)

(b)   (d)
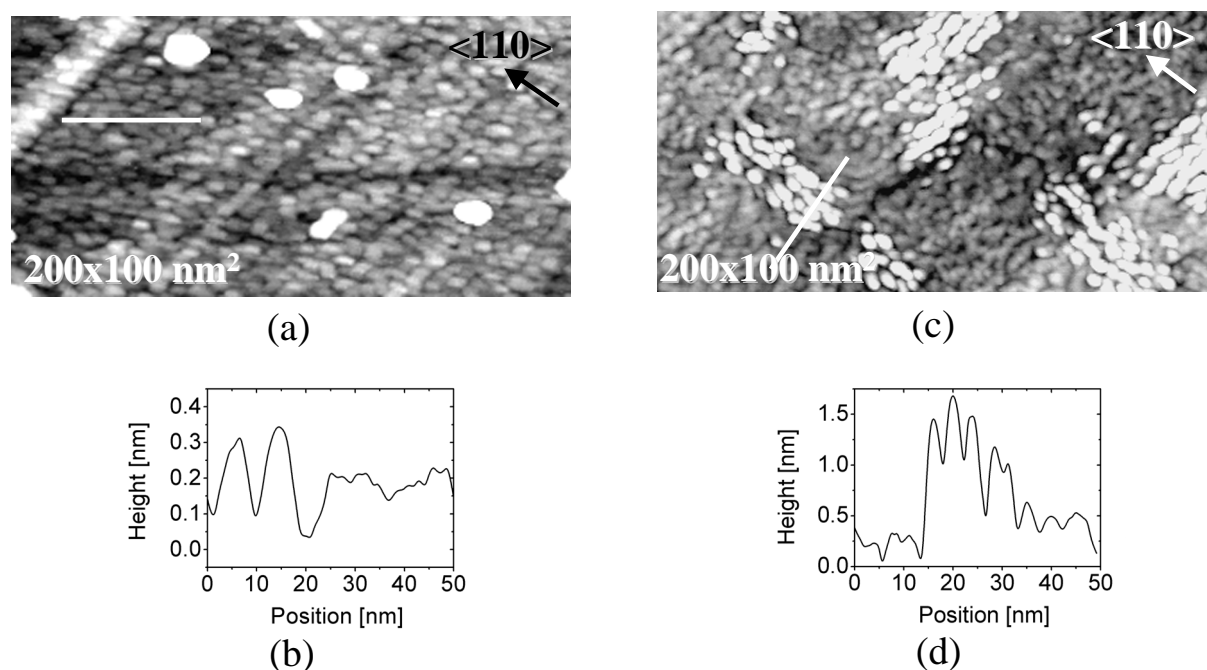
Figure 3.11: 200×100 nm² STM images of: (a), ≈2.5 ML, and (c), ≈20 ML, of Fe grown at LT on Au-covered Si(001). Line profiles taken along the white lines in (a) and (c) are shown in (b), and (d), respectively. All scans were performed at 1.6 V bias voltage and a constant tunneling current of 1.0 nA.

performed is responsible for the growth of small Au droplets seen as bright details in Fig. 3.10(a) and Fig. 3.11(a). Not even the deposition of 20 ML of Fe is able to completely wipe out the overall details of the underlying reconstruction (Fig. 3.11(c)), but some additional elongated bright features, apparently oriented along the substrate < 110 > directions become visible. They are responsible for a drastic local roughening of the surface (Fig. 3.11(d)) which is otherwise as flat as in the case of 2.5 ML deposited Fe. These approximately 1.5 nm tall details appearing in large groups might be associated with a local formation of silicide grains, triggered by rising the temperature up to RT to perform the STM scans. Intermixing might have taken place through incomplete reconstructed patches which always appeared in the STM images if the reconstruction was not performed at high enough temperatures, or the amount of deposited Au was insufficient.

3.5.2 Magnetic properties

It should be emphasized at this point that the complex structure of the reconstructed surface induces crystallographic relationships in the Au buffer layer which could not be assessed due to the lack of the LEED pattern. As shown in the previous section, this layer is far from being smooth, and the subsequent deposition of Fe does not result in the growth of an ordered film. Accordingly, the findings on the magnetic behavior of the Fe films grown on Au-covered Si(001) presented here cannot be directly related to the previously works concerning the magnetic properties of Fe grown on Au(001) [64, 66–69].

The onset of magnetization in the Fe film grown on Au-covered Si(001) at RT was found in this study to take place at about the same coverage (slightly below 4 ML) as in the case of films deposited at RT directly on (2×1) Si(001). The reason for the "late" magnetization onset found here does not necessarily reside in a large scale silicide formation due to the inefficient surface passivation, because increasing the thickness of the buffer layer up to 4÷5 ML does not help an earlier onset of magnetization. Instead, the roughness itself of the buffer layer and Au segregation might be responsible for the "late" onset of the ferromagnetic order. However, at the onset coverage, an out-of-plane orientation of the magnetic moment was detected (the dotted loop in Fig. 3.12(a)), which
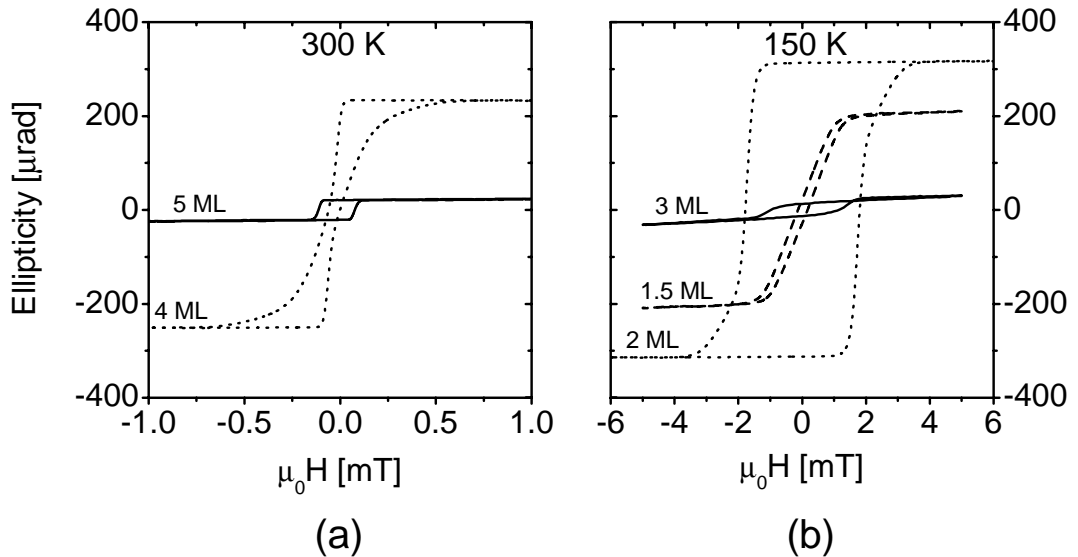
Figure 3.12: Perpendicular (dotted and dashed lines) and in-plane (solid lines) hysteresis loops taken shortly after the magnetization onset at RT ($\approx$300 K), (a), and $\approx$150 K, (b). Fe film thicknesses are marked on the corresponding loops.

flips in-plane with the addition of another monolayer of Fe (the solid loop in Fig. 3.12(b)). The out-of-plane orientation of magnetization in such films at RT is unexpected if a straightforward connection to the case of Fe growth on Au(001) is made. In this respect, it was shown by Bader *et al.* [64, 66] that the ferromagnetic order exists at RT even in the submonolayer range, but the direction of magnetization lies always in the film plane. The perpendicular magnetization was observed in this work only for films grown on substrates which were previously reconstructed by the deposition of Au at high temperatures and additionally buffered with an ultrathin Au layer.

By growing both the buffer layer and the Fe film at LT on the Au-induced reconstructed Si(001) surface, an early onset of the out-of-plane magnetization at slightly less than 1.5 ML of Fe was observed (the dashed line in Fig. 3.12(b)). Thus, the existence of a significant magnetically dead layer is excluded. For no ferromagnetic order is possible in an isotropic two dimensional system [70], such very early onset of magnetization is put on the expense of the perpendicular anisotropy induced in the Fe film by the underlying Au layer. With slightly increasing the film thickness, the out-of-plane orientation of magnetization is preserved and an even stronger signal was measured (see the dotted line in Fig. 3.12(b) corresponding to a $\approx$2 ML thick film). Eventually, between 2.5 and 3 ML, the magnetization flips into the film plane and typical in-plane MOKE loops are observed hereafter (solid line in Fig. 3.12(b)). It is worth emphasizing again the occurrence of the out-of-plane magnetization in a very thin Fe film at temperatures higher than 100 K, reported by Liu *et al.* [68] as the prerequisite for the onset of a thermally unstable perpendicular magnetization on freshly prepared Au(001). Moreover, Fe (silicide) films thinner than 2.5 ML grown directly on Si(001) did not yield any magnetic signal in the MOKE measurements and no perpendicular magnetization was detected for thicker films at both 150 and 300 K. In this view, one should make the ultrathin Au passivation layer responsible for the early onset of the perpendicular magnetization in the Fe film.

The plots of MOKE ellipticity at saturation measured here at both RT and LT *vs.* the amount of deposited Fe on Au-covered Si(001) (open squares in Fig. 3.13(a),(b)) show interesting behaviors if compared to the corresponding values in the absence of the buffer layer (solid squares in Fig. 3.13(a),(b)). Except for the out-of-plane signal found shortly after the magnetization onset, the measured MOKE ellipticity increases monotonously with coverage, but their modest values infer a quite low magnetization in the RT grown films. In the case of in-plane magnetized films grown at LT, strongly enhanced Kerr signals in comparison to films grown without buffer layers at the same temperature were observed
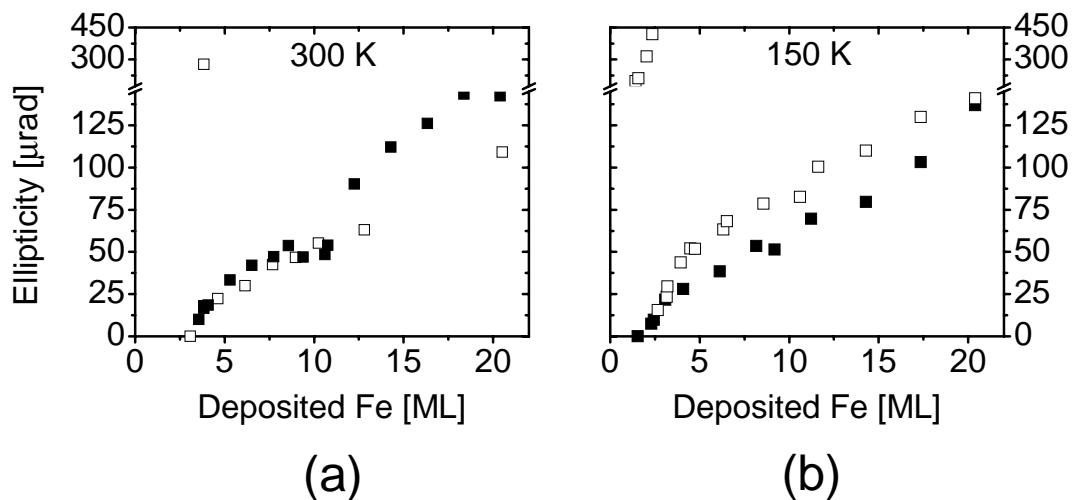
Figure 3.13: MOKE ellipticity at saturation *vs.* the amount of deposited Fe at room temperature (300 K), (a), and ≈150 K, (b), on (2×1) Si(001) (solid squares) and Au-covered Si(001) (open squares). The points above 200 μrad at low coverage stand for the out-of-plane magnetization.

(compare the open and solid squares in Fig. 3.13(b)). From the onset of magnetization at ≈1.5 ML of Fe and from the enhanced magnetic signal at LT one may conclude that silicide formation is significantly suppressed. A silicide film resulting after the deposition of about 1.5 ML of Fe on (2×1) Si(001) does not exhibit any magnetic signal in MOKE at LT, as observed in this work. The suppression is further inferred by the absence of any kink in the plot of ellipticity at saturation *vs.* coverage around 10 ML in the case of Fe grown on buffered Si(001) at 150 K (the open squares in Fig. 3.13(b)).

If the system Fe/Au/Si(001) is meant to be compatible with the silicon technology, than, beside the influence of the diffused Au into the bulk Si on the properties of the charge carriers [71], the thermal stability is a serious matter of concern. Therefore, films of various thicknesses were investigated in this study with respect to their magnetic properties upon different annealing conditions.

First, a 12 ML thick Fe film grown at RT directly on the Au-induced reconstructed Si(001) was shortly annealed up to about 400 K to check for the thermal stability of the reconstruction, and account for the magnetization behavior as the result of thermally activated Si out-diffusion. As shown in the preceding section, the overall appearance of the underlying reconstruction is preserved, while the film's morphology undergoes certain modifications (see Fig. 3.9). The longitudinal MOKE loops, measured before and after
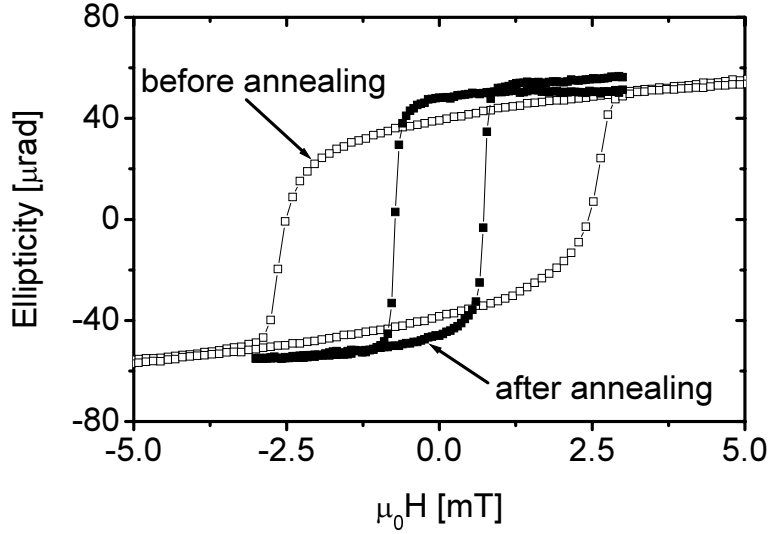
Figure 3.14: Longitudinal MOKE loops of ≈12 ML of Fe deposited at RT on Au-induced reconstructed Si(001), before (open squares) and after a short annealing up to about 400 K (solid squares).

annealing, saturate basically at the same ellipticity, but the remanence is slightly enhanced upon annealing, and a decrease in coercivity by a factor of almost 4 is noticed (Fig. 3.14). Such magnetic softening of the film might be explained by both a structural and chemical change as the result of annealing. However, the unchanged saturation suggests that either Si outdiffusion is only minor, or the resulting intermixing does not affect the Fe magnetization.

Second, the magnetization of several monolayers thick Fe films grown at LT on Au-buffered Si(001) was pursued with respect to annealing temperatures close to RT. To obtain a complete picture of the interface phenomena which may be thermally triggered, both perpendicularly and in-plane magnetized films with thicknesses of 2.3 and 3 ML, respectively, were considered for annealing. In doing this, one expects that any structural and chemical modifications which might be undergone by the film will leave a fingerprint on the magnetization behavior. As revealed by the loops in Fig. 3.15(a),(b), two different situations were observed. The 2.3 ML thick film, whose MOKE loops are depicted Fig. 3.15(a), preserves its perpendicular orientation of magnetization upon annealing up to 280 K. A decrease in ellipticity from ≈420 μrad at LT (the solid line in Fig. 3.15(a)) to ≈310 μrad was measured at about 280 K (the dotted line in Fig. 3.15(a)). This behavior is attributed to the reduction of magnetization when the Curie temperature is
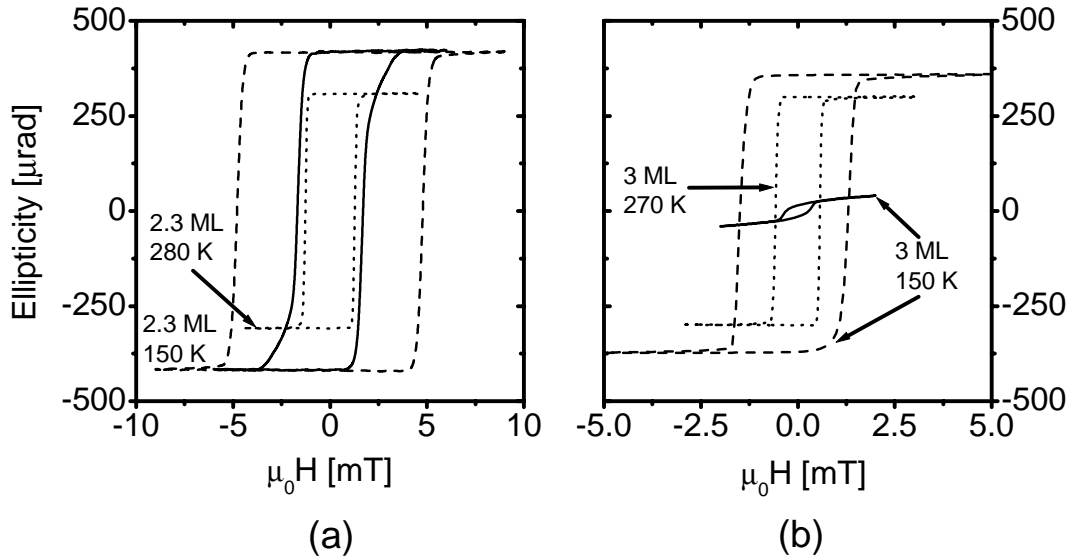
Figure 3.15: (a): Out-of-plane hysteresis loops of a 2.3 ML thick Fe film grown on Au-covered Si(001) at 150 K (solid line), annealed to 280 K (dotted line) and cooled back to 150 K (dashed line). (b): An in-plane magnetized 3 ML thick Fe film grown on Au-covered Si(001) at 150 K (solid line), undergoes a transition to a state with perpendicular magnetization at 270 K (dotted line), which is preserved upon cooling back to 150 K, where a larger signal is measured (dashed line).

approached. The MOKE remanence retrieved its initial value upon cooling back to 150 K (the dashed line in Fig. 3.15(a)), indicating no measurable loss of magnetization which would have been attributed to intermixing. The increase in coercivity noticed after the cycle is completed might be caused by minor local silicide formation, hindering domain wall motion. The overall square-like shape of the hysteresis loops and the perpendicular orientation of magnetization was preserved throughout the process.

In the situation depicted in Fig. 3.15(b), an in-plane magnetized 3 ML thick film (the continuous loop) becomes perpendicularly magnetized upon annealing to ≈ 270 K (the dotted loop in Fig. 3.15(b)). Since a transition from the in-plane to the out-of-plane magnetization in a given film upon rising the temperature is thermodynamically prohibited, such behavior appears unphysical. However, it will be shown in Chapter 5 that such transition is not unlikely if structural and/or compositional modifications involving the Au buffer layer are considered. An even stronger out-of-plane signal was measured as the temperature was decreased back to ≈ 150 K (the dashed line in Fig. 3.15(b)), and,

with slightly increasing the thickness, the magnetization flipped back into the film plane.

One can say at this point that the facts presented so far cast some favorable light on the possible use of the system under investigation here in new fields of semiconductor technology. In this respect, the possibility of manipulating the perpendicular magnetization, appears quite promising. A detailed discussion on the issue of perpendicular magnetic anisotropy is presented in a broader framework in Chapter 5.

Chapter 4

Fe on InP(001)

In this work, Fe films of thickness ranging from the submonolayer coverage to almost 20 monolayers were grown by molecular beam epitaxy on InP(001). An investigation of the substrate reconstruction is made, and the films were characterized with respect to their structural, morphological, compositional and magnetic properties.

Among the III-V compound semiconductors, InP shows, under certain conditions, a (2×4) reconstruction of the (001) surface which does not resemble to any other seen before [72,73]. In spite of the low lattice mismatch $(a_{InP(001)} - 2a_{Fe})/2a_{Fe}$ of only +2.2 %, the growth of Fe is expected to be strongly affected due to the reactions which were previously shown to occur at the interface, leading to the formation of metallic phosphide compounds and to In out-diffusion [9, 10, 25, 26]. The attempt of growing phosphide and indium free Fe films on sulphur passivated InP(001) failed [27]: the S-terminated surface was shown to be disrupted upon Fe deposition, and, while the substrate InP(001) core-level photoemission signal has been completely attenuated, the P, In, and in addition the S chemically shifted components of the spectra are clearly visible even for ordered Fe films.

4.1   Substrate preparation

Small pieces of about $10 \times 2 \times 0.4$ mm^3 were cut from undoped n-InP(001) $\pm 0.25°$ wafers with a specified electrical resistivity of 3.0×10^{-1} Ωcm, and mounted on molybdenum holders equipped with radiative heating facilities. No chemical pre-treatment was carried out prior to inserting the sample into the UHV chambers via the load lock system. The

substrates were firstly degassed in UHV up to about 570 K, and then sputtered at the same temperature with an off-normal 500 eV Ar^+ ion beam, while the sample was rotated to reduce the amount of surface roughening due to sputtering. At a partial Ar pressure of about 5×10^{-8} mbar, a sputtering current density of about 0.02 $\mu A/mm^2$ was measured. After the cleaning cycle was completed, no traces of contaminants were noticed in the AES spectra. Sharp LEED patterns, and flat and large terraces in the STM topographs were observed, as discussed in the next section.

4.2   The (001) surface of InP

Indium phosphide has a lattice constant of 5.87 Å, and exhibits the same structure as all of the III-V compound semiconductors, *i.e.*, the zinc-blende structure. This is depicted in Fig. 4.1 and is basically identical to the one of silicon, except for the fact that the
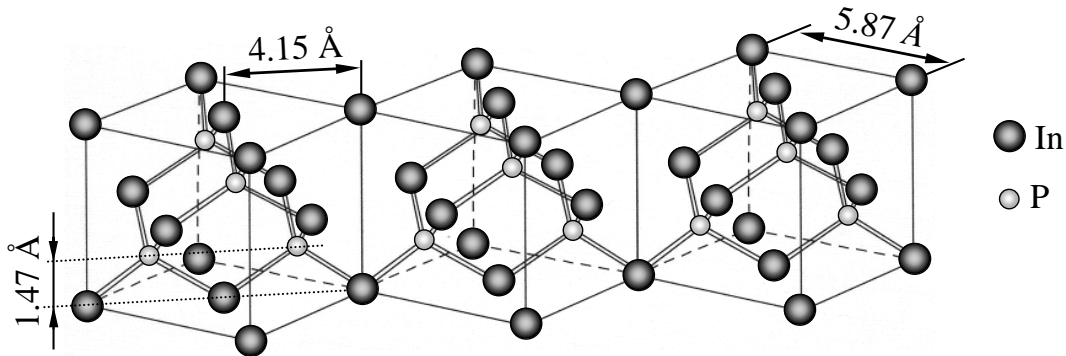
Figure 4.1: The structure of InP(001). The relevant interatomic distances are shown.

building atoms belong to two different chemical species.

The ideal (001) surface of a III-V compound semiconductor is polar, either cation (group III elements) or anion (group V elements) terminated, and has a metallic character. As in the case of bulk terminated Si(001), partially filled dangling bonds (sp^3 hybridized) should be found on the surface. However, truncation gives rise to an incomplete hybridization and the dangling bonds (antibonding orbitals) are both p- (for cation) and s-like (for anion) [74]. For stability reasons, both bonding and antibonding electronic states, must be filled if they lie below the Fermi level (*e.g.* the anion s-like orbital), and empty if they lie above it (*e.g.* the cation p-like orbital) [74]. Therefore, to achieve a

stable semiconducting state, electron transfer occurs from the cation to the anion dangling bonds, so that the former are empty and the latter are filled [75, 76], according to the electron counting model [74]. In addition, the dimers are arranged within the unit cell to yield the lowest possible electrostatic energy [77]. These considerations were found to apply for the GaAs(001) surface and are expected to be valid for all III-V compound semiconductors.

Experimentally, the InP(001) surface has been investigated by many authors with respect to the types of reconstructions and terminations that can be assessed under different preparation conditions [72, 73, 78–91]. In those studies, molecular beam epitaxy (MBE) and chemical beam epitaxy (CBE) systems, as well as metal-organic chemical vapor deposition (MOCVD) and metal-organic vapor phase epitaxy (MOVPE) reactors have been used in connection with UHV facilities to obtain flat and clean surfaces. In some of those works [78–81], where mainly the In-rich (2×4) and $c(2\times8)$ phases were investigated, As/P cap layers have been employed to prevent surface deterioration while transporting the samples through the air from the growth reactors into the UHV systems. Different phases were shown to form by thermal desorption of the cap layers. A high resolution STM investigation was performed by MacPherson *et al.* [72] on the In-rich (2×4) phase and a trimer model was proposed, later supported by first-principle calculations [92]. However, it has been recently shown by Guo *et al.* [73], who performed a comprehensive study of the structural transformations of P-rich InP(001) surface phases obtained by sputtering and annealing in a P_2 atmosphere, that the observed trimer-like structures are also consistent with the occurrence of mixed In-P dimers on a P-rich (2×4) surface. In their model, the top layer is composed of 0.25 ML of mixed dimers oriented along $[\bar{1}10]$, while the second layer consists of 0.5 ML of In and P in the same proportion on a complete third layer of P. Mixed In-P dimers are found also in the troughs between the rows. The P-rich (2×4), (2×1), (2×2) and (4×4) phases were also previously obtained by MBE [82–84] and CBE [85], as well as in MOVPE [85–90] and MOCVD [91] reactors with direct connections to the UHV chambers, that is, without the use of cap layers.

The ion bombardment and annealing of InP(001) has been shown by some authors [93–95] to yield mainly an In-rich $(4\times2)/c(8\times2)$ reconstruction. The reported P-rich surface obtained in this way was unreconstructed [94, 95], and was associated with the existence of contaminant hydrogen, carbon and oxygen. However, by the cleaning procedure used in this work, surfaces free of contaminants were obtained, as one can deduce from the AES spectra depicted in Fig. 4.2(a). In addition, a sharp (2×4) pattern with basically no

(a)   (b)
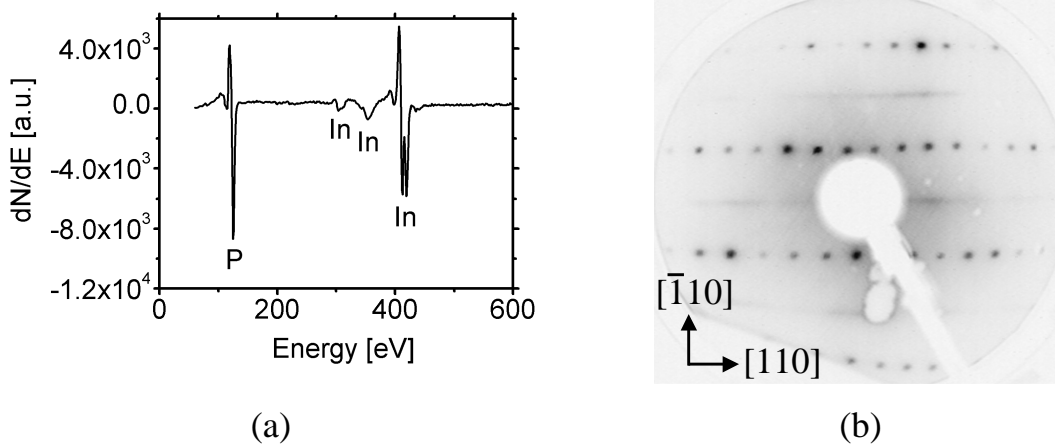
Figure 4.2: The surface of InP(001) after sputtering at ≈570 K: (a), AES spectrum, and (b), the (2×4) LEED pattern taken at a beam energy of 57 eV.

background was seen in LEED (Fig. 4.2(b)). The measured AES spectra give a ratio of 1.20 ± 0.05 between the peak-to-peak intensities of the P_{LMM} line at 120 eV and In_{MNN} line at 404 eV, indicating a P-rich surface. Slight variations in the sputtering temperature, which might cause a minute P depletion and/or an incipient In segregation as the decomposing temperature is approached, may be responsible for the small variance in the above ratio. To find out the type of the predominant surface species, the values obtained here are compared with the P_{LMM}/In_{MNN} ratios of 1.05 and 1.30 earlier reported for the P-rich (2×1) and c(4×4) phases, respectively, prepared by MOCVD [91]. The discrepancy between the values found in this work and some of the previously published results assigning the dominant surface chemical species to In is explained by the difference in the annealing temperature: beyond about 600 K, that is, close to the decomposing temperature, In droplets start to form and a hazy appearance of the surface is noticed, while the sharp (2×4) LEED pattern persists. As suggested by Guo *et al.* [73], the formation of In droplets on a P-rich (2×4) surface obtained by ion bombardment and annealing certainly misled the interpretation of the data obtained by macroscopical spectroscopic techniques employed in the those studies [93–95]. Erroneously, the results were associated with an In-rich (4×2)/c(8×2) reconstruction due to a high density of In droplets on the surface.

The cleaning procedure applied in this work always yields a droplet-free surface with large terraces, as can be seen in the STM scans in Fig. 4.3(a),(b), with predominantly *single* step-edges of 0.3 nm height (see the line profile in Fig. 4.3(c)). This value is close
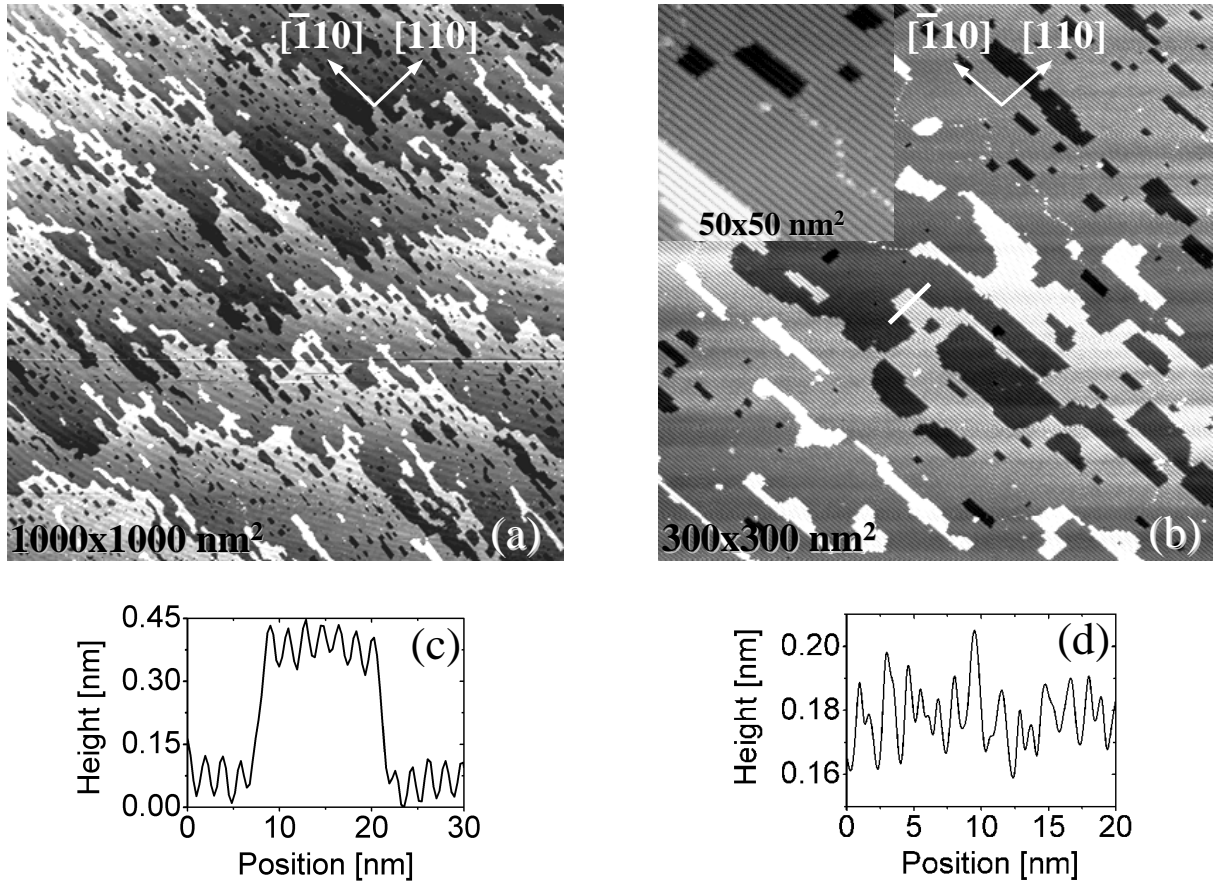
Figure 4.3: 1000×1000 nm^2, (a), and 300×300 nm^2, (b), STM scans of the InP(001) surface after sputtering at ≈570 K. The inset in (b) reveals the row-like appearance of the reconstructed surface on a 50×50 nm^2 area. The scans were performed at -2.7 V bias voltage and a constant tunneling current of 0.3 nA. The profile in (c) was taken over the terrace in (b) marked with a white line. The line profile in (d) was taken over one of the rows in the inset of (b), along [$\bar{1}$10].

to half of the InP lattice parameter, that is, the projection along [001] of the distance between atoms belonging to the same group, either III or V (see Fig. 4.1). Since this is the minimum separation distance between (001) planes of identical chemical species, such steps are denominated as *single*. The high resolution STM image shown in the inset of Fig. 4.3(b) reveals an overall row-like appearance of the surface. The same characteristic is found on all of the scanned areas, and is associated with surface restructuring. The line profile in Fig. 4.3(d) taken along one of the reconstruction rows in the inset of Fig. 4.3(b) gives a corrugation of about 0.4 Å. According to the STM analysis presented so far, the

same surface phase is expected to exist throughout the sample, terminated with the same species on all of the terraces.

4.3   Fe grown on (2×4) InP(001)

In contrast to the abundance of work concerning the magnetic, structural and morphological properties of ferromagnetic films grown under different conditions on the most widely used semiconductors, *i.e.*, Si(001) and GaAs(001), there are few data published on thin Fe films grown on the technologically relevant (001) surface of InP. So far, only the chemical reaction between thin Fe films and S-passivated InP(001) has been investigated [27], and no information on the magnetic behavior has been reported up to date.

4.3.1   Growth investigation

In this study, thin Fe films were grown by molecular beam epitaxy on (2×4) P-rich InP(001) at substrate temperatures of ≈150 (LT) and ≈300 K (RT). For morphological characterization, only the RT case was considered since the transport into the STM is performed via uncooled manipulators. The early growth stages were investigated in the thickness regime starting from fractions of a monolayer up to several ML. The deposition of a minute amount of Fe, *e.g.* slightly less than 0.2 ML, is able to almost completely wipe out the streaks at the half order position in the LEED pattern (Fig. 4.4(a)), and a stronger background is noticed. It appears that an increased disorder is induced by the growing of small size Fe islands, but no preferred growth direction can be seen in the filled states STM image in Fig. 4.4(b). The regular and sharp appearance of the substrate reconstruction, like the one revealed by the STM image in the inset of Fig. 4.3(b), becomes smeared out by the Fe islands, but the overall row-like characteristic is preserved. Thus, it seems that the Fe islands prefer to nucleate atop the rows rather than in the troughs between them. The line profile in Fig. 4.4(c) taken along substrate [$\overline{1}10$] direction over one of the reconstruction rows gives a hint about the island sizes. A comparison with the equivalent profile for the bare surface in Fig. 4.3(d) supports the fact that the observed ≈1.5 Å corrugation in Fig. 4.4(c) is assigned to the irregularly separated Fe islands, of 1 ML thickness. The most predominant island lateral size appears to be about 1 nm, which stand for approximately 7±1 Fe atoms. These numbers point at the same island size as the one found earlier in the case of ≈0.2 ML of Fe grown on As-rich (2×4)
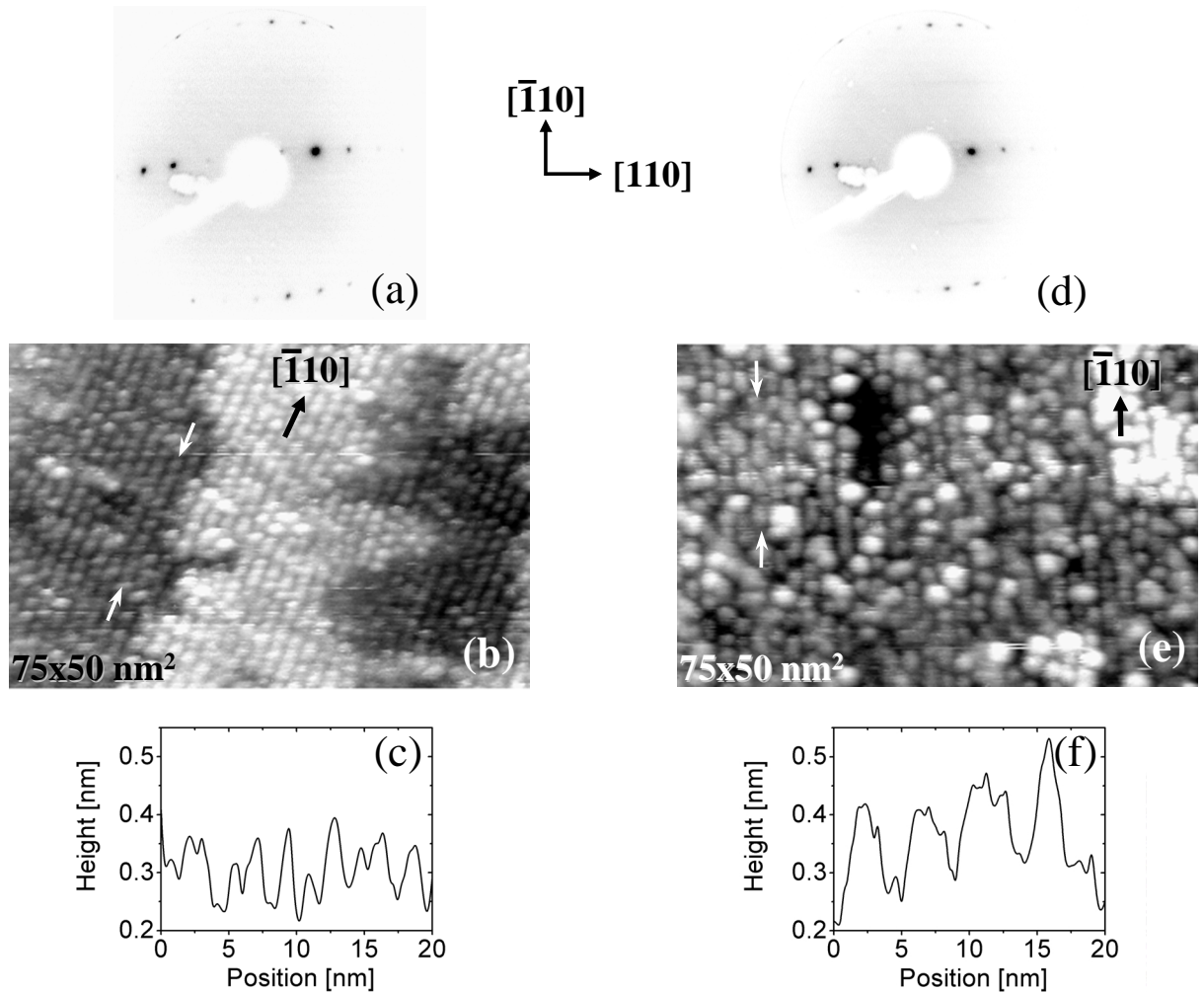
Figure 4.4: LEED patterns taken at a beam voltage of 52 eV, and 75×50 nm² STM scans of RT grown Fe films of thickness slightly less than 0.2 ML, (a) and (b), and of ≈0.4 ML, (d) and (e). The STM images were taken at a bias voltage of -2.7 V and constant tunneling currents of 0.3 and 0.1 nA, respectively. The line scans shown in (c) and (f) were taken along the substrate's [$\bar{1}$10] direction, as marked with the white arrows. The substrate symmetry axis are shown.

GaAs(001) [96]. The addition of slightly more Fe to a total thickness of 0.4 ML is not able to disrupt the reconstruction, since sharp LEED spots are still observed (Fig. 4.4(d)), and the row-like appearance in the filled states STM image persists to some extent (Fig. 4.4(e)). Therefore, small Fe islands and (2×4) reconstructed areas coexist at least up to 0.4 ML. The line profile in Fig. 4.4(f) taken along substrate [$\bar{1}$10] direction over one of the rows reveals larger Fe islands than in $\lesssim$0.2 ML thick film, with the distribution of the lateral

sizes around several nanometers. Most of the islands are 1 ML thick, but also 2 ML thick
islands are observed. They can be seen as brighter bumps in Fig. 4.4(e) and are generally
associated with larger islands lying over two substrate rows. One can state now that the
growth of 3D islands proceeds very early at RT, after no more than 0.4 ML of Fe were
deposited.

At an Fe thickness of about 0.8 ML, the LEED spots can hardly be seen, and no
pattern is visible any longer as the thickness approaches 1 ML. As inferred from the
STM image in Fig. 4.5(a), the LEED pattern disappearance is associated with a complete
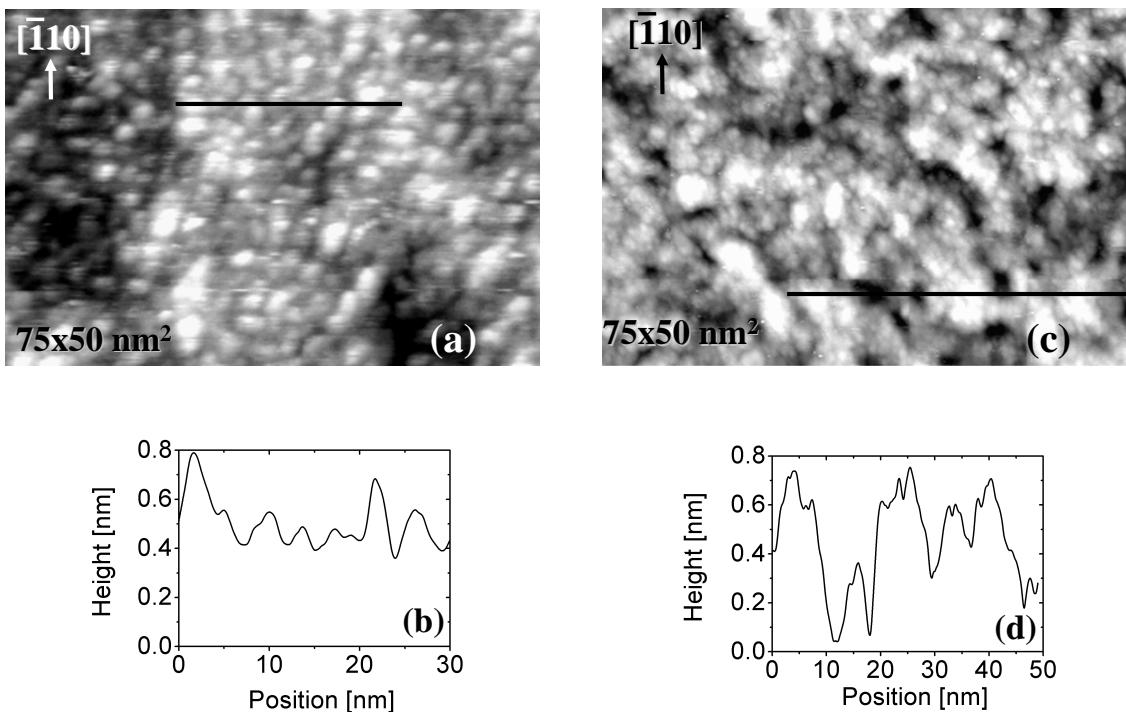
Figure 4.5: 75×50 nm² STM scans of RT grown Fe films of thickness ≈0.8 ML, (a), and ≲4 ML,
(c), taken at a bias voltage of -2.7 V and 1.4 V, respectively, and 0.1 nA constant tunneling
current. The profiles in (b) and (d) were taken along the black lines in (a) and (c), respectively.
The substrate symmetry axis are marked on the figures.

fading of the row-like look of the surface. Therefore, a high degree of structural disorder
in the film or on the surface of the growing film is inferred. The islands are not so
clearly defined as in the case of lower Fe coverage (compare to Fig. 4.4(b),(e)), and, by
inspecting the line profile in Fig. 4.5(b), a slight increase in corrugation is noticed. At
higher coverage, no LEED pattern reappears, at least up to the coverage investigated here

($\approx$20 ML). This result is in contrast to the reappearance of a sharp LEED pattern in the case of RT Fe growth in excess of about 3 ML on GaAs(001) [97], which cannot be solely explained by the differences in the sign and magnitude of the lattice misfits: ($a_{substrate}$ - $2a_{Fe}$)/$2a_{Fe}$ = +2.2 % and -1.6 % for InP(001) and GaAs(001) substrates, respectively. The reason for the high disorder in the Fe film grown on InP(001) is not clear. At an Fe thickness slightly below 4 ML, the film is characterized by small 3D coalesced islands, and no preferred orientation can be distinguished (Fig. 4.5(c)). The islands are irregular and their heights vary between 2 and 5 ML as can be deduced from the line profile in Fig. 4.5(d). Therefore, the RT deposition does not results in the growth of a smooth film.

To assess the degree of intermixing, an Auger electron spectroscopy (AES) investigation of the Fe films grown at both LT and RT was performed. The evolution of the P_{LMM} line at 120 eV, the In_{MNN} one at 404 eV, and the Fe_{LMM} line at 651 eV were measured as a function of Fe film thickness. The normalized peak-to-peak intensities are shown in Fig. 4.6(a),(b) for the two growth temperatures. The normalization of phosphorus and indium signals was done with respect to the sum of P_{LMM} and In_{MNN} peak-to-peak intensities at zero Fe coverage. Along with the experimental line intensities, the predicted P (the dashed line) and In (the solid curve) AES peak-to-peak intensities normalized as before are shown. The predicted curves were deduced by assuming an attenuation of exponential form according to:

$$I^{P,In} = I_0^{P,In} exp \left(-\frac{1.435 \; t_{Fe}}{cos\phi \; \lambda_{Fe}^{P,In}} \right) \tag{4.1}$$

with inelastic mean free paths (IMFP) in iron, λ_{Fe}^P and λ_{Fe}^{In}, of 4.6 Å for the 120 eV P_{LMM} Auger electrons [98], and 8.6 Å for the 404 eV In_{MNN} ones [98–100], without taking into account the back-scattered electrons. Here, $I_0^{P,In}$ stands for the normalized substrate P_{LMM} and In_{MNN} intensities without attenuation, t_{Fe} is the Fe film thickness in ML, and ϕ represents the admittance angle into the cylindrical mirror analyzer. In the above approach, it is supposed that the deposited Fe forms a flat and continuous film, and no intermixing occurs at the interface. For both the sample and cylindrical mirror analyzer with electron gun had to be moved between the successive depositions/measurements, the scattering of the experimental data points appears quite strong, but valuable information can still be obtained.

From a first glance at the AES signals measured at the two growth temperatures, one can immediately see the completely different In line behavior from one case to the other:

while the experimental signal follows rather closely the predicted curve of no intermixing at LT (Fig. 4.6(a)), an almost constant signal was observed at RT up to about 12 ML, followed by a rather slow decay (Fig. 4.6(a)). This behavior is associated with a significant amount of In segregating on the top of Fe grown at RT, which gradually becomes buried
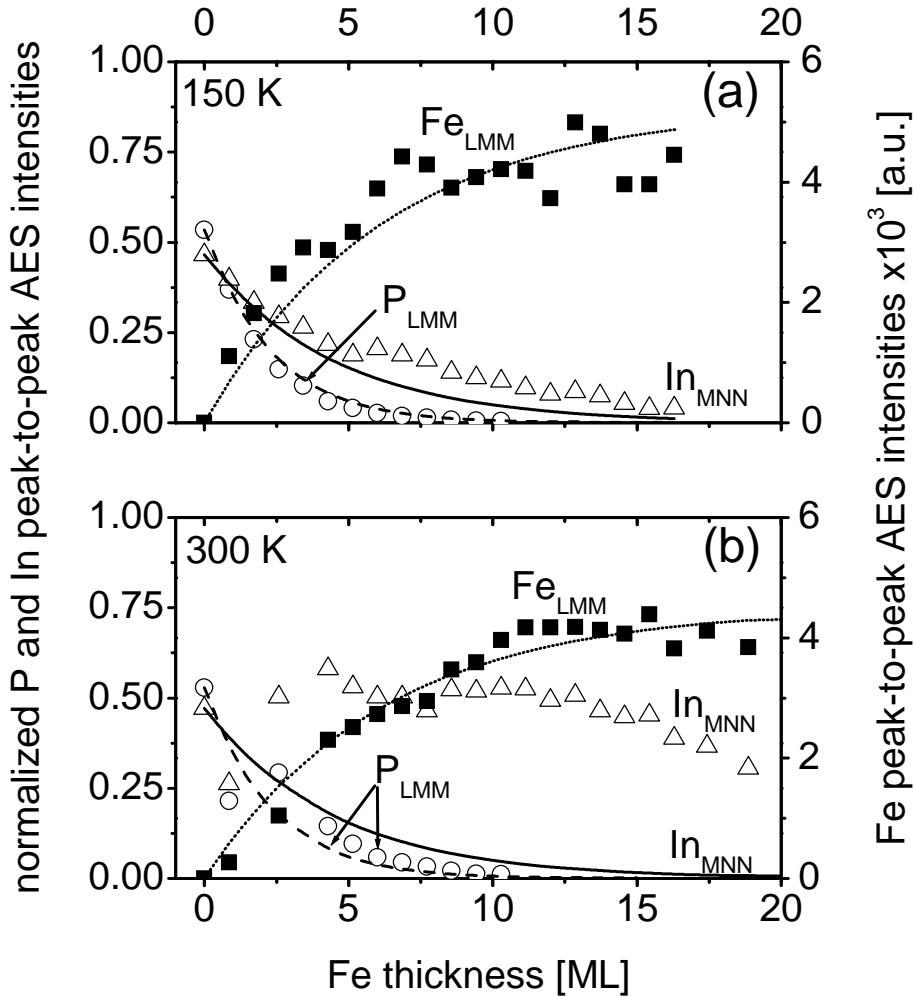
Figure 4.6: AES peak-to-peak intensities of the Fe_{LMM} line at 651 eV (solid squares), along with the normalized AES peak-to-peak intensities of the P_{LMM} line at 120 eV (open circles) and In_{MNN} line at 404 eV (open triangles), measured for films grown at $\approx$150 K, (a), and at $\approx$300 K, (b). The dashed and solid curves stand for the predicted P and In normalized intensities, respectively, in the hypothesis of an ideal Fe growth (flat and continuous film as well as no intermixing). The dotted curves are fits of the Fe signal. The normalization of P and In signals was done with respect to the sum of P and In intensities at zero Fe coverage.

into the growing Fe film as its thickness increases, similarly to the finding of Hughes *et al.* [27].

By a careful comparison between the evolution of the experimental P_{LMM} AES intensity with the thickness of the LT grown film and its prediction curve (the open circles and the dashed line, respectively, in Fig. 4.6(a)), one can assert on the remarkably good agreement between each other. However, one should keep in mind that the Fe film shows a significant departure from the ideal growth assumed in computing the prediction curves. The exponentially decaying P_{LMM} intensity close to its prediction curve, and its vanishing at about 11 ML of deposited Fe do not support the picture of a *strong* Fe-InP(001) intermixing with a significant Fe phosphide formation [27]. Instead, intermixing can be excluded within the sensitivity of AES.

4.3.2 Magnetic properties

In contrast to the apparent disordered growth, magnetic measurements point at some order in the film, as described below. During LT and RT Fe growth, the magnetization behavior was probed *in-situ* by the longitudinal magneto-optic Kerr effect (MOKE), for fields along the two relevant substrate symmetry directions, [$\bar{1}$10] and [110], that is, parallel and perpendicular to the reconstruction rows. Shortly after the ferromagnetic order sets in, the loops taken at LT (Fig. 4.7(a),(b)) and RT (Fig. 4.7(c),(d)), for 2.6 and 3.6 ML thick films, respectively, reveal a strong uniaxial in-plane magnetic anisotropy behavior similar to the case of Fe grown on GaAs(001) [101]: while hysteresis open up in square-like shapes for fields along [$\bar{1}$10] (Fig. 4.7(b),(d)), pure rotation loops were observed along [110] (Fig. 4.7(a),(c)), regardless of the growth temperature. Thus, one can denote the substrate [$\bar{1}$10] direction as the easy axis of magnetization for the Fe film, and the [110] one as the hard axis. Hence, the magnetic anisotropy is the fingerprint of some order in the grown film, in contrast to the LEED results. The magnetization appears to be fully rotated parallel to [110] at fields of roughly one order of magnitude higher than the coercive fields of the hysteresis measured along [$\bar{1}$10]. For the two growth temperatures and for the whole range of thickness investigated, the easy axis was found to lie in-plane, and no perpendicular component of magnetization was detected. The discrepancy between the lack of any LEED pattern and the order inferred by the uniaxial behavior of magnetization might be explained by assuming a high degree of disorder at the film's growth front induced by In segregation, as shown in the preceding section. As deduced
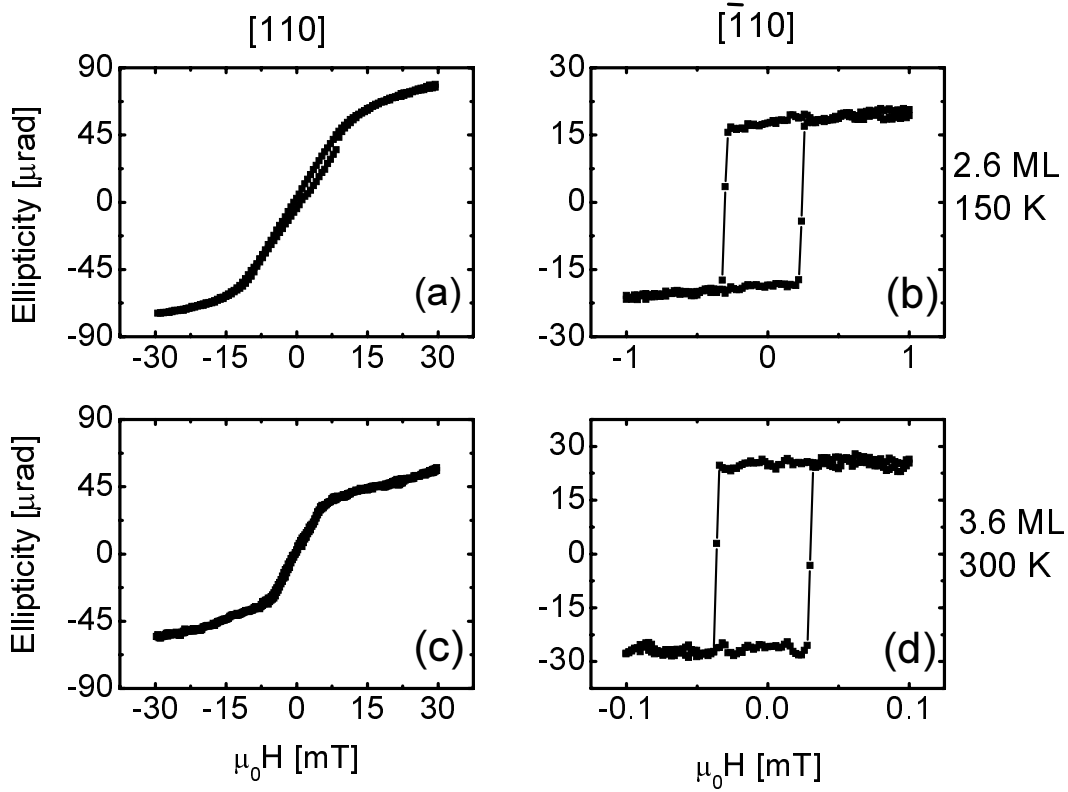
Figure 4.7: In-plane magnetic loops taken shortly after the magnetization onset at both LT (≈150 K) and RT (≈300 K), *i.e.*, for Fe film thicknesses of 2.6 and 3.6 ML respectively. The magnetic field was oriented, along the two relevant crystallographic directions of the substrate: [110], (a), and [$\bar{1}$10], (b), at ≈150 K. The loops in (c) and (d) were measured at ≈300 K, for the same field orientations. The two directions defined by the substrate [110] and $\bar{1}$10] axis are denoted as the hard and easy axis of magnetization, respectively, for the Fe films

from the MOKE investigation along both [$\bar{1}$10] and [110] directions, the uniaxial behavior of the in-plane magnetic anisotropy persists up to about 13÷15 ML. This behavior cannot be related to any shape anisotropy of the incipient growing film, as already mentioned. Therefore, the uniaxial character of the substrate's (2×4) unit cell, and implicitly of the interface may bear the whole responsibility for the magnetic anisotropy found here.

The attempt of tempering with the magnetic anisotropy in the manner discussed in the previous chapter by growing an intermediate, or cap Au layer (see Chapter 5), did not produce the expected perpendicular anisotropy. Instead, a rotation of the easy/hard axis with 90° was observed, as reported by Elmers and Gradmann [102] in the case

of Au capped Fe(110) films grown on W(110). Beside of a somewhat earlier onset of magnetization observed when a Au buffer layer was used ($\approx$3 ML at RT), the uniaxial character of the magnetic anisotropy is preserved, but its strength is drastically reduced.

In the following, an evidence is brought to support the existence of a net magnetization in the very first layer of Fe being deposited. The hysteresis loops measured along the easy axis, the substrate [$\bar{1}$10], more precisely the remanent ellipticity, gives a good estimate of the magnetization, and, by plotting this values *vs.* Fe thickness, valuable information can be obtained about the state of magnetization in the first layers by simply determining the intercept between the linear fit of the remanent ellipticity data points and the coverage axis. This is shown in Fig. 4.8(a),(b) for the two growth temperatures investigated here,
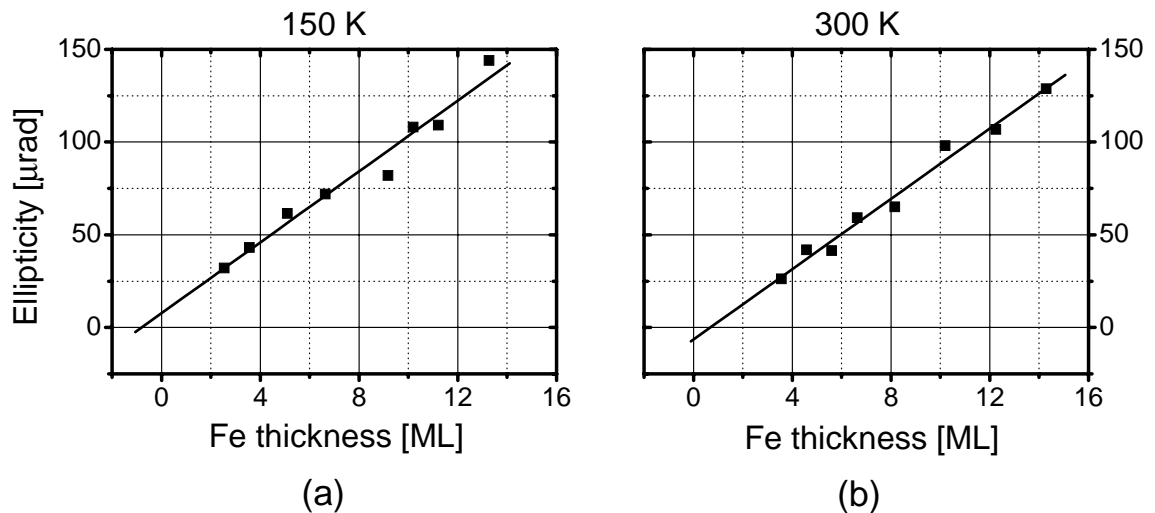
Figure 4.8: MOKE remanence deduced from the loops measured along [$\bar{1}$10] *vs.* the Fe coverage at $\approx$150 K, (a), and $\approx$300 K, (b). Linear fits of the data points intersect the coverage axis at -0.5$\pm$0.7 ML in (a) and +0.8$\pm$0.4 ML in (b), respectively.

and the following values for the intercepts were found: -0.5 $\pm$ 0.7 ML for Fe films grown at LT and 0.8 $\pm$ 0.4 ML in the RT case. The later value would have been definitely lower if the MOKE ellipticity had been measured farther from the Curie temperature of the film. Thus, one can state from this finding that the ferromagnetic order is likely present in the first layer of the growing film. In other words, no significant magnetically dead layers form at the interface between the substrate and the film, at least in the case of LT growth. The slightly different numbers found above for the two growth temperatures are indicative of different interfaces (as also inferred from the AES data shown in Fig. 4.6), and different

surface/interface magnetic anisotropies are expected in these two cases. This last issue
will be addressed in detail in Chapter 5. The lack of a significant dead layer might be due
to either a very sharp interface or to the formation of ferromagnetic Fe-based compounds,
among which, only ones with $\lessapprox$27 at.% P are known to posses a non-zero magnetization
at RT [103]. However, as found in the preceding section, a large scale formation of such
compound is not supported by our experimental findings, and not expected either from
the literally zero P solubility in αFe at room temperature [104]. Thus, at most a minute
amount of the ferromagnetically ordered compound whose stoichiometry is close to Fe_3P
might form at the interface.

4.3.3   Schottky barrier height

The other aspect of interest, the height of the Schottky barrier, was also addressed in this
study for the role it plays on processes associated with spin injection into semiconductors.
The schematic representation of the energy band diagrams depicted in Fig. 4.9 explains
the processes leading to the formation of the Schottky barrier in a simplified picture [105].
Bringing a metal into intimate contact with a semiconductor results in the match of the
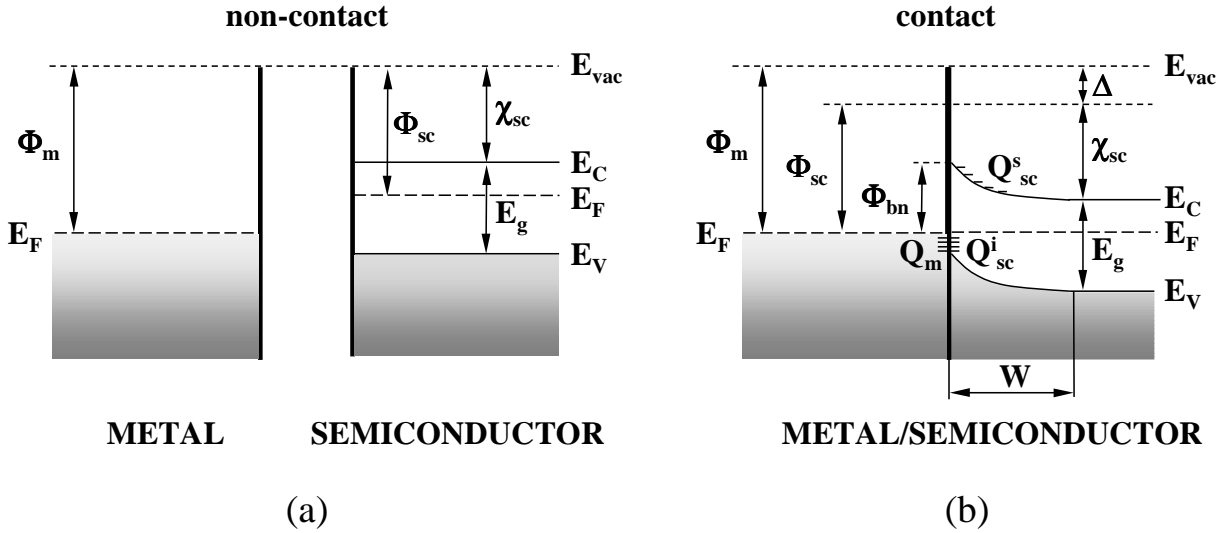
Figure 4.9: The energy band diagrams for a metal and a n-type semiconductor in non-contact,
(a), and in contact, (b). The Schottky barrier height, Φ_{bn}, is the difference between the Fermi
level, E_F, and the bottom of the conduction band E_C at the interface.

Fermi level E_F in both materials accompanied by a charge transfer. Due to the high
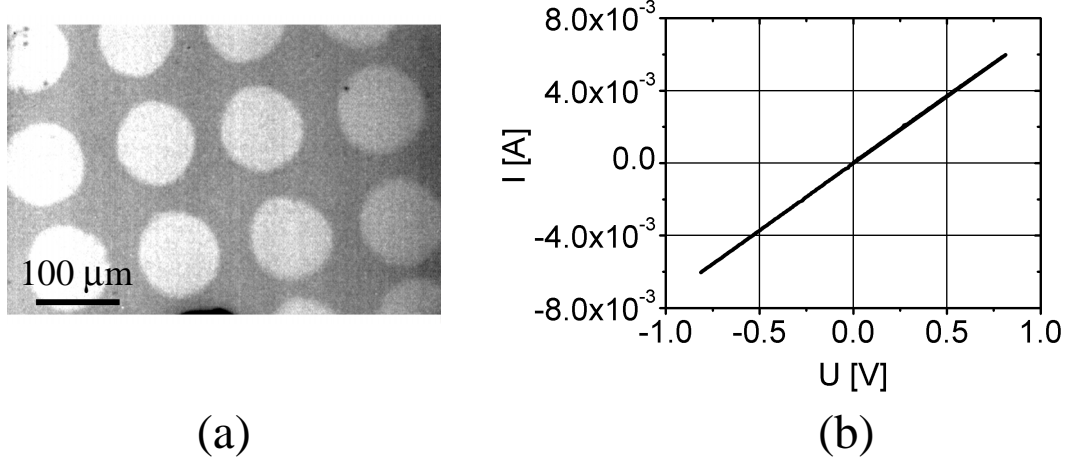
Figure 4.10: (a): An image of the patterned film. The separation distance between the patches (diameter of 100 μm) was about 50 μm. (b): Room temperature current-voltage characteristic performed on a 25 ML thick Fe film grown at $\approx$300 K on n-type InP(001).

density of states in the metal, charges remain on the metal side of the interface Q_m while on the semiconductor side one can find both space Q_{sc}^s and interface charges Q_{sc}^i. Since the space charges occur because of the uncompensated ionized donors, their density depends on the doping level. The space charges extend into the semiconductor over distances of about 100-1000 nm (the depletion zone, W) and are responsible for the band bending. The interface charges Q_{sc}^i occur if semiconductor surface states exist, but they might also be induced by the metal in contact. They are located in about 1 nm into the semiconductor, and give rise to the Fermi level pinning. The other quantities in Fig. 4.9 represent the top of the valence band E_V, vacuum level V_{vac}, metal work function Φ_m, semiconductor work function Φ_{sc}, semiconductor electron affinity χ_{sc}, semiconductor band gap E_g, the interface dipole Δ, and are defined as sketched in the figure.

To perform the electrical characterization, a patterned Fe film of about 25 ML thickness capped with a protection layer of Au was grown at RT on an n-type InP(001) for *ex-situ* current-voltage (I-V) characterization. The patterning into disks of 100 μm diameter laterally separated by 50 μm (Fig. 4.10(a)), was performed *in-situ* by means of the deposition through a shadow mask with the corresponding mesh flipped over the cleaned substrate. Due to the low lateral dimension of the patches distributed over the sample, the measurements were performed in the two-point geometry. For an estimate of the Schottky barrier height, the current-voltage characteristic measured *ex-situ* is plot-

ted in Fig. 4.10(b). From the linear shape of the I-V characteristic one can state that no measurable Schottky barrier can be detected at RT. The non-rectifying character of the Fe/n-InP(001) contact appears favorable for the implementation of the system into spintronic devices as discussed in the introductory chapter.

Chapter 5

Discussion

The results presented so far give more insights into the phenomena arising upon the growth of ultra thin iron films on certain elemental (silicon) and compound (indium phosphide) semiconductor substrates, known as strongly reactive. Due to the variety of aspects investigated, the findings described in the previous chapters need a cohesive discussion to account for the underlying physics in a more unified picture. Thus, the issues of surface reconstruction, film growth and magnetic anisotropy will be addressed in the following.

5.1 Surface reconstructions

5.1.1 Au-induced reconstructed Si(001)

As shown in Chapter 3, slightly less than 1 ML of Au deposited at high temperatures on Si(001) leads to a complete surface restructuring. The mechanisms leading to the new surface reconstruction can be summarized as follows [63]: with the first Au atoms impinging on the (2×1) Si(001) surface, missing dimers are generated and align in rows perpendicular to the dimer rows. With increasing the amount of deposited Au, stripes parallel to the dimer rows start to form, and the step configuration is modified drastically. The rearrangement of the surface atoms in stripes running along the $< 110 >$ directions over distances of the order of microns give rise to the occurrence of different structures, according to the substrate temperature and the amount of deposited Au [23, 63, 65, 106]. For a given thickness, the initial (2×1) structure changes into ($\sqrt{26}$×3), via c(8×2) and ($\sqrt{26}$×1), as the temperature increases [23]. Shimakura *et al.* [63], deduced from STM data solely that the ($\sqrt{26}$×2) and ($\sqrt{17}$×2) phases building a $(9 \times 2)R7°$ structure occur

as well at lower temperatures ($\approx$800 K), while c(18$\times$2) forms at $\approx$1000 K. A mixture of (5$\times$3) and ($\sqrt{26}\times$3) ($\sqrt{26}$=5.099) surface structures (3.84 Å unit mesh) built from both Si and Au atoms was shown by Lin *et al.* [65] to form on the surface around 1100 K deposition temperature. Recently, the incommensurate (5$\times$3.2) phase was also shown to occur under similar conditions on a vicinal Si(001) surface [106].

The two domain (2$\times$1) LEED pattern of clean Si(001) (see Fig. 3.2(c)) transformed upon Au deposition at temperatures of interest here (1000÷1100 K) into different ones (Fig. 3.6(a),(b)), due to new phase formation associated with surface restructuring. The overall symmetry deduced from the LEED patterns appears quite sensitive to the growth conditions. If temperatures around 1000 K are employed to perform the reconstruction, a typical two domain (2$\times n$) pattern can be observed, as shown in Fig. 3.6(a). The n-fold periodicity can hardly be assessed solely from the LEED pattern in Fig. 3.6(a), most likely because different (2$\times n$) phases coexist on the surface, rendering the streak-like appearance to the pattern. Since sharp spots can still be distinguished in addition to the integer and half order ones, it appears that the different phases arrange themselves in a rather ordered manner to build up the reconstructed surface.

In the high resolution STM images obtained in this study for a Au growth temperature of $\approx$1000K, decorated bright and dark stripes separated by trenches were observed (Fig. 5.1(a)). These stripes lie behind the occurrence of the surface phases mentioned above. The periodicity arising from the stripe decoration and their lateral separation can be assessed by taking line profiles along the relevant symmetry directions, as shown in Fig. 5.1(b)-(d). The line profile in Fig. 5.1(b) gives a separation distance between stripes of about 25 Å. The profiles along the stripe direction taken over both the bright (Fig. 5.1(c)) and dark ones (Fig. 5.1(d)) give a periodicity of $\approx$8 Å in the corresponding direction which stands for 2$\times$3.84 Å. As the high resolution STM scan in Fig. 5.1(a) shows, the two-fold periodicity along the dark stripes appears to modulate an additional decoration associated with a lateral spacing close to 3.84 Å (Fig. 5.1(d)). The decorations on adjacent rows may be in phase, or slightly shifted along the stripes, leading to the occurrence of oblique surface structures. If adjacent rows are decorated out-of-phase, larger rectangular unit structures arise. The defects along the bright stripes in Fig. 5.1(a) seem to be responsible for this behavior. Therefore, while it is relatively easy to rule on the two-fold symmetry of the surface phases from both the LEED and STM data, it appears quite intricate to resolve the higher order periodicity. Consequently, a complete account on the surface phases can be hardly given in this case. Moreover, for the filled state
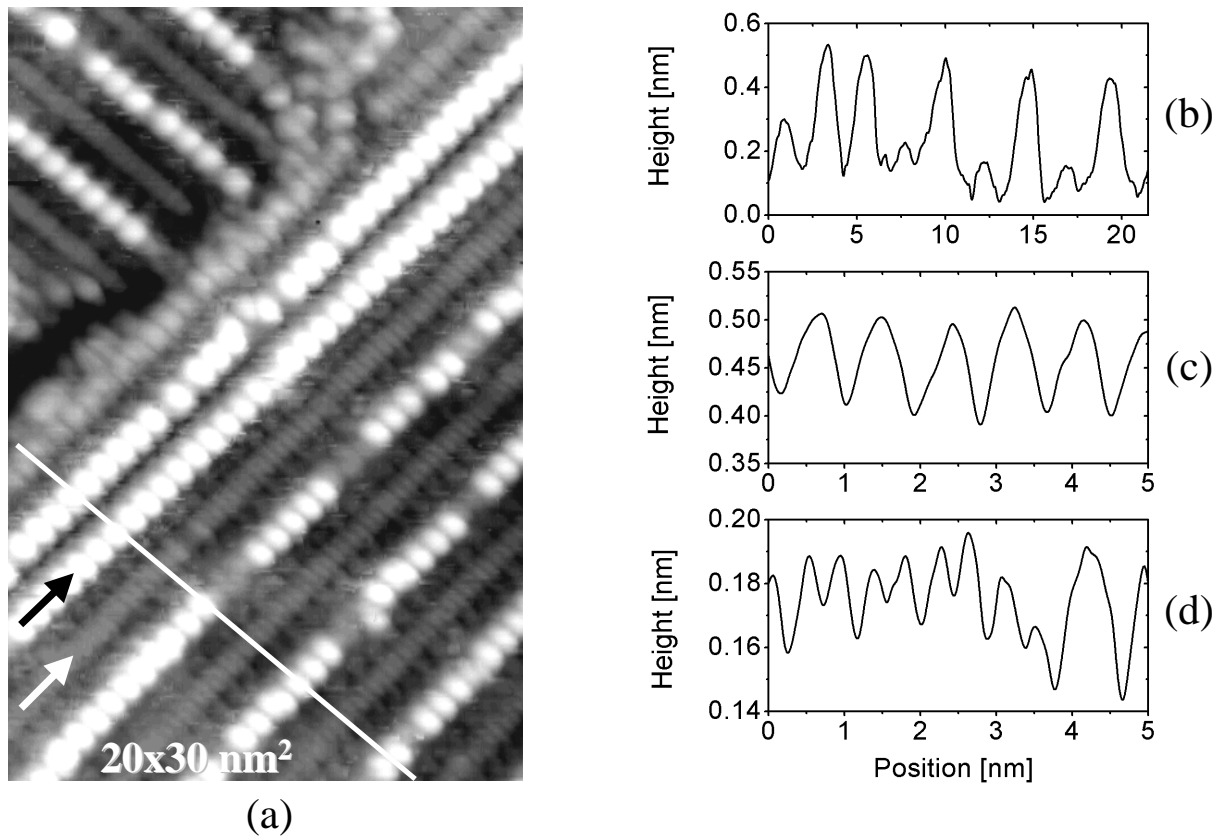
Figure 5.1: (a): High resolution STM image of the reconstructed surface performed by the deposition of ≈1 ML of Au on Si(001) at 1000 K. The image was taken at -1.6 V bias voltage and a constant tunneling current of 1.0 nA. The scanning direction is at 45° with respect to < 110 > (the direction of stripes). The line profiles were taken across the stripes, (b), on the path marked accordingly, and over the bright, (c), and dark stripes, (d), indicated with arrows.

STM image in Fig. 5.1(a) lack the atomic resolution, and the drifts are conspicuous while scanning small areas, the correct periodicity of the surface unit cells might be obscured.

If the reconstruction is performed at a slightly higher temperature (1100 K), the structure of the surface phase(s) can apparently be easier deduced from the LEED pattern, in spite of its becoming more complex (Fig. 3.6(b)). As in the previous case, the sharpness of the LEED spots is indicative of a good crystallographic order on large distances. At the first sight, the overall periodicity of the diffraction spots suggests that a phase whose structure is close to (5×3) is the dominant one. However, from the sequences of additional spots at one and two third order positions, one can rule on the existence of additional

phases. It was deduced by Lin *et al.* [65] from their atomic resolution STM images and LEED data that the oblique ($\sqrt{26} \times 3$) phase also occurs around 1100 K. From the resemblance between the LEED pattern and STM image shown here (Fig. 3.6(b) and Fig. 5.2(a), respectively), and their results, one can state that it is the ($\sqrt{26} \times 3$) phase
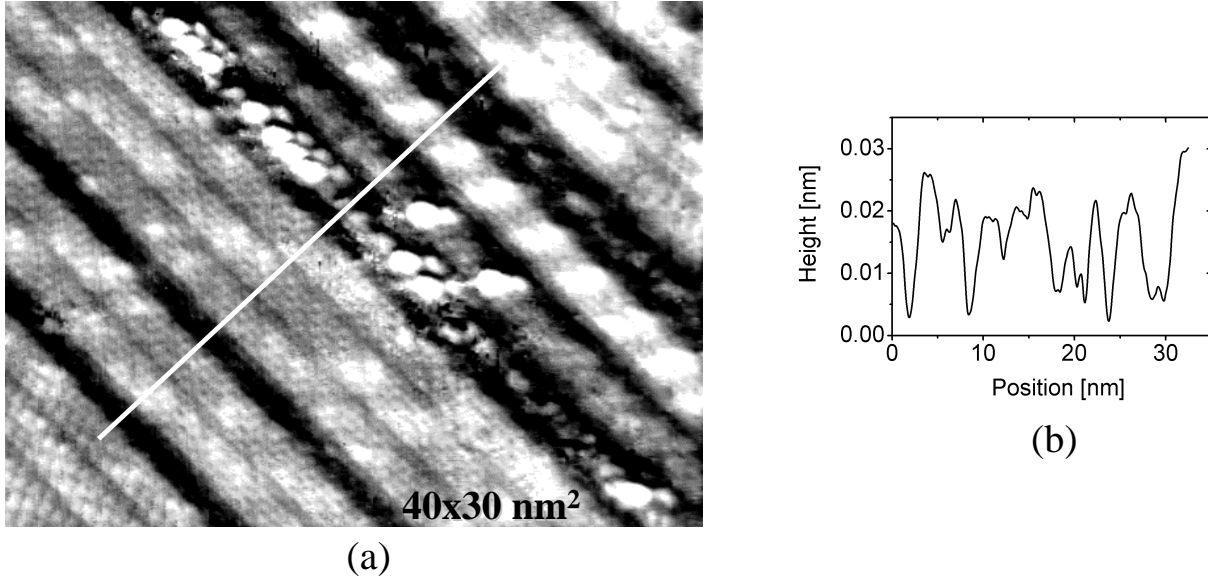
Figure 5.2: (a): High resolution STM image of the reconstructed surface performed by the deposition of $\approx$1 ML of Au on Si(001) at 1100 K. The image was taken at -1.6 V bias voltage and a constant tunneling current of 0.6 nA. The scanning direction is at 45° with respect to $< 110 >$ (the direction of stripes). The line profile in (b) was taken over the stripes, along the path marked in (a).

which most likely coexists with the (5×3) one on the sample prepared here.

However, for the reasons to be discussed in the following, precautions should be taken in assigning the correct surface structure. The atomic resolution STM data shown in Ref. [65] clearly point at displacements of the surface atoms with respect to the bulk (1×1) positions. The corresponding STM images are definitely not misleading for they were uniquely drift corrected by matching the aspect ratio of cells on neighboring terraces. On this basis, the (5×3) and ($\sqrt{26} \times 3$) structures were unambiguously sketched. Nevertheless, the periodicity of the LEED spots in Ref. [65] at the one third and two thirds positions does not match the proposed diagram (compare Figs. 8 and 9 in Ref. [65]), for the latter was pictured for *bulk* positions of the surface atoms. Accordingly, the real structures might be slightly distorted with respect to the proposed ones. Indeed, Minoda *et al.* [106], assigned

the (5×3.2) structure to the phases on the (001) terraces of a vicinal Si(001) crystal.

The high resolution STM image acquired in this study (Fig. 5.2(a)) reveals the atomic decoration of the reconstruction stripes, but is not sufficient for an accurate determination of the surface phases. Moreover, some residual drift corroborated with a slight scanner decalibration make difficult a precise determination of the small distances. The important result here is that the $\approx$24 Å wide stripes (5×3.84 Å $=19.2$ Å) in Fig. 5.2 appear lying next to each other or separated either by $\approx$18 Å wide trenches or by differently decorated stripes. Such sequences of stripes and trenches were not reported by Lin *et al.* [65] in their work. Therefore, it is reasonable to assert that not only the (5×3) and ($\sqrt{26}\times3$) phases contribute to the surface reconstruction observed here. In addition, the stripes may slightly slip with respect to each other along their length. This process is responsible not only for the formation of the oblique ($\sqrt{26}\times3$) surface phase, but may also lead to the occurrence of larger rectangular structures if out-of-phase atomic decorations arise in adjacent stripes.

5.1.2 P-rich (2×4) InP(001)

It was shown in the previous chapter that sputtering InP(001) with low energy ions at elevated temperatures leads to the formation of the P-rich (2×4) surface phase. The corresponding LEED pattern (Fig. 4.2(b)) appears in the STM topographs taken here as rows running along [$\bar{1}$10], as shown in Fig. 5.3(a). The rows are 0.15 nm tall and

(a)   (b)
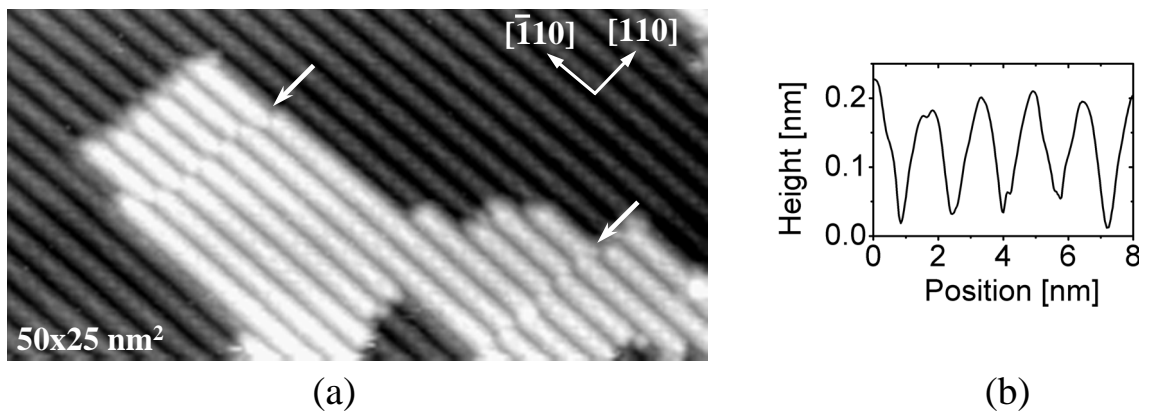
Figure 5.3: 50×25 nm^2 STM scan performed at -2.7 V bias voltage and a constant tunneling current of 0.3 nA, (a). Row displacements are marked with white arrows. The line profile in (b) is taken across the rows.

equally spaced by about 1.6 nm, as deduced from the line profile in Fig. 5.3(b) taken across a sequence of rows. This is consistent with the size of the (2×4) unit cell of 4×4.15 Å along [110] (see Fig. 4.1). It was proposed by Yang *et al.* [107] that the P-stabilized (2×4) phase shows a missing-dimer arrangement similar to that observed in the case of GaAs(001) [108], with two kinds of microscopic structures: α and β. In their work, these structures were obtained after annealing the P-rich (2×1) phase at about 630 and 600 K, respectively, and can be microscopically distinguished by the number of missing P-dimer rows: two dimer rows and two missing-dimer rows for the α phase giving a P coverage of 0.5, and three dimer rows and one missing-dimer row for the β phase giving a P coverage of 0.75. It is obvious from the filled states STM image pictured in Fig. 5.3(a) that mainly the (2×4) phase is present on the substrates prepared by sputtering at ≈570 K, and a very low degree of disorder is to be noticed. From both the AES spectrum shown in Fig. 4.2(a) and the width of the reconstruction rows of about 1.1 nm deduced from the line profile in Fig. 5.3(b), one can conclude that a phase whose structure is similar to the β phase of (2×4) GaAs(001) is the predominant one. The width of 1.1 nm found from the line profile in Fig. 5.3(b) is the closest to 3×4.15 Å which corresponds to three P dimer rows (see Fig. 4.1). However, the difference between the typical appearance of the α- and β-(2×4) phases of GaAs(001) as previously seen by STM [109] and the high resolution STM image of P-rich (2×4) InP(001) shown here in Fig. 5.4(a) is striking. The reported rectangular shape of the two and three As dimers parallel to [$\bar{1}$10] in the α-, and β-(2×4) GaAs(001) respectively, cannot be mapped into a similar peculiarity in the case of (2×4) InP(001), but rather a trimer-like feature possibly associated with the formation of mixed In-P dimers [73] should be considered.

The LEED pattern displayed in Fig. 4.2(b) shows sharp (1×4) spots and intensity modulated streaks along [110] at the superstructure half order positions, indicative of a significant degree of disorder at first sight. Weiss *et al.* [94] associated the LEED streaks at half order position they observed on In-rich (4×2) surface with the occurrence of the c(8×2) phase as the result of a phase shifted domain between (4×2) cells. The apparent inconsistency with the high degree of order inferred by the STM images shown in Fig. 4.3 and 5.3 might be simply explained by a mechanism proposed by Hashizume *et al.* [110] to account for the occurrence of the c(2×8) phase of GaAs(001) by a slight modification of the (2×4) one. If adjacent dimers shift by 5.87×$\sqrt{2}$/2 Å, *i.e.*, by 4.15 Å, in the [110] direction, the quarter LEED spots remain unchanged, and only the half order ones become streaky. Shifts in the reconstruction rows which were considered to lead to a streaking of the half

(a)

(b)
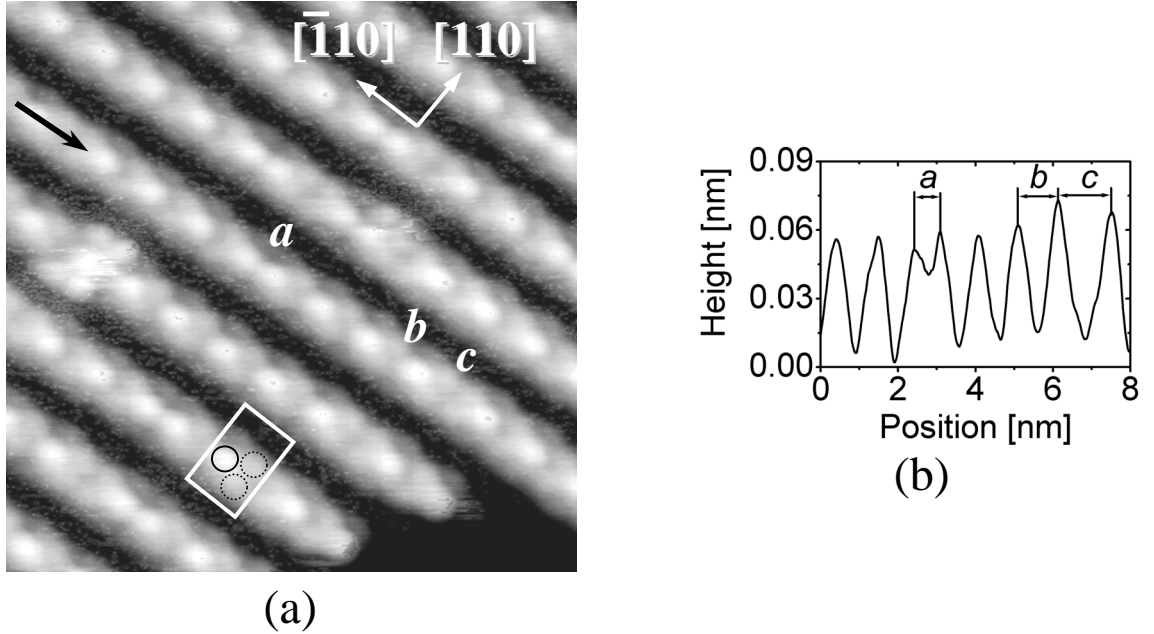
Figure 5.4: 10×10 nm^2 STM scan performed at -2.7 V bias voltage and a constant tunneling current of 0.3 nA, (a). The (2×4) unit cell comprising the mixed P-In dimers indicated with circles is shown. The solid circle marks the bright central dimer. The line profile in (b) is taken along [$\bar{1}$10] over the row marked with a black arrow in (a). The three spacings between the central dimers, namely *a*, *b* and *c* are marked accordingly. They correspond to the three stackings responsible for the streaks seen in the LEED pattern in Fig. 4.2(b).

order spots in the LEED pattern were also observed by MacPherson *et al.* [72] on In-rich (2×4) InP(001), again with a question mark on the predominant surface element. These dimer displacements are accompanied by shifts in the same direction of entire groups of rows, without affecting the row position on the neighboring terraces. This kind of row displacements are clearly pointed out by the white arrows in Fig. 5.3(a). Following the same line of reasoning one should also consider the displacement of rows with respect to each other on adjacent terraces (Fig. 5.3(a)) by the same quantity, *i.e.*, 4.15 Å, as leading to streak formation in the LEED patterns. However, as one can see from the STM images in Fig. 4.3(b) and Fig. 5.3(a), the minimum lateral size of the shifted domains is of the order of 100 Å, which accounts for about 4 % of the surface Brillouin zone (SBZ). In other words, this corresponds to a half order spot broadening along [110] with 4 % of the distance between the (00) and (01) spots. Thus, it is obvious that the mechanism described above will not result in any conspicuous departure from a sharp (2×4) pattern

with very well defined half order spots. Accordingly, their complete wipe out must be induced by a mechanism which originates from atomic scale disorder, as described in the following.

A careful inspection of the high resolution filled states STM image in Fig. 5.4(a) reveals remarkable details concerning not only the structure of the (2×4) unit cell (marked correspondingly in the Fig. 5.4(a)), but also their "packing" to build up the surface reconstruction. As already mentioned above, the observed trimer-like appearance of the unit cell was shown by Guo *et al.* [73] to be comprised of mixed In-P and missing dimers. Accordingly, the central brightest feature in the cells, whose approximate lateral dimension is about 5 Å, may be associated with a topmost In-P dimer. Two additional weaker features, P anions (mostly the electron rich species, *i.e.*, the anions, are visible as protrusions in the STM filled state images) in the second layer, bonded most likely with the P anions in the third layer can be seen in the unit cell, forming a triangle-like peculiarity with the mixed dimer in the first layer. The features were marked accordingly with circles in the (2×4) unit cell depicted in Fig. 5.4(a). This finding supports the existence of a (2×4) phase on the crystals used in this work, whose structure appears to be similar to the one previously reported by Guo *et al.* [73]. Moreover, by closely inspecting the sequences of the trimer-like features along the reconstruction rows, an undoubtful experimental evidence for the proposed packing orders [73] is brought here: the three letters on the line profile along [$\bar{1}$10] in Fig. 5.4(b) correspond to the three possible orientations of the topmost In-P dimers with respect to each other in the neighboring cells along the row marked with an arrow in the STM image in Fig. 5.4(a). The predominant sequence, namely the In-P In-P one or, equivalently, P-In P-In is marked with "b" ($\approx$10 Å), the In-P P-In sequence with "a" ($\approx$7 Å), and the P-In In-P one with "c" ($\approx$14 Å). The slight discrepancy between the double of the lattice parameter, 8.30 Å, and the measured b value can be put on the expense of unavoidable drifts while scanning very low areas and/or of a slight STM scanner decalibration. As one can distinguish from the position of the weaker features in Fig. 5.4(a), the underlying P anions accordingly follow the orientation of the mixed topmost dimers to keep the trimer-like appearance. Therefore, as suggested by Guo *et al.* [73], the disorder induced by these three distinct packings on the electron density stands for the real mechanism responsible for the occurrence of streaks in the LEED pattern. One should also mention that the existence of additional packings as well as the possibility of the out- and in-phase dimer buckling should also be taken into account. In addition, the presence of a minute amount of additional phases can not be

ruled out, among which, the c(4×4) one was reported to occur on P-rich InP(001) [82].

5.2 Growth of Fe on Si(001) and InP(001)

In the study presented in this thesis, Fe was grown on substrates whose reactivity does not allow the possibility of obtaining highly ordered films. In the first growth stages, Fe nucleates on the reconstruction rows of the bare substrates and high cluster densities were observed due to the low adatom mobility. The growth proceeds very early in the 3D way leading to a high corrugation in thicker films, usually associated with the formation of interfacial compounds even in the case of films grown at ambient temperatures. The reduction of the growth temperature limits the interdiffusion, but the degree of structural order is poor. One can obviously employ different thick (tens of Å) buffer layers to prevent the reaction and improve the structural quality of the film by adjusting the growth/annealing temperature within a rather wide range. However, such approach just relaxes the substrate influence to the point that it is no longer "seen" by the growing film. In such case, the problem reduces very often to the investigation of buffer layer growth, usually *known* as good templates for the subsequent Fe growth. Under these circumstances, one can hardly conceive spin-injection experiments, for an electron passing into the semiconducting substrate through a thick buffer layer and two interfaces (not necessarily sharp) might undergo a spin-flip scattering process with rather high probability.

In the presence of ultrathin (several monolayers) passivation films, the allowed growth and annealing temperatures are drastically restricted. In this context, a few monolayer thick Au film was deposited in two steps on (2×1) Si(001) in the attempt to hinder silicon out-diffusion even at ambient temperatures. Complications arise in this case for Au segregates on the top of the Fe film and the passivation efficiency is questionable. The growth of a smooth film is favored by reducing the deposition temperature down to about 150 K followed by annealing up to RT (see Fig. 3.11), but the lack of the LEED pattern indicates a structurally disordered film. However, from the perpendicular magnetization observed in ultrathin films (see Section 3.5.2) it is obvious that Si out-diffusion is *not* responsible for the poor crystalline order. As it will be discussed in the forthcoming section, interesting magnetic properties arise as the result of annealing LT grown films close to RT. This thermal process should be accompanied by structural/compositional modifications involving the passivation Au layer. Unfortunately, the absence of a LEED pattern does not allow any account for the structural changes undergone by the ultrathin

films.

The extent of film-substrate intermixing can be assessed by Auger electron spectroscopy (AES). According to the description given in Section 4.3.1, such approach was successfully applied in the case of Fe grown on InP(001), where a significant amount of In was found to segregate on the film at ambient temperatures, while the P signal follows the predicted curves reasonably closely. The almost constant In AES intensity measured at RT (see Fig. 4.6(b)) does not mean a constant amount of floating In. If this were the case, the exponential decaying bulk contribution to the total measured signal would inflict a similar exponential behavior to the total signal throughout the thickness range investigated. Therefore, with increasing the film thickness, an increasing amount of In segregates on the top of it, at least up to about 12 ML of deposited Fe. This segregated layer might induce a high degree of structural disorder at the film's growth front leading to a complete wipe out of the LEED pattern and might also be responsible for modifications of the surface magnetic anisotropy of the film. In the LT growth case, the intrinsic disorder due to the reduced growth temperature, and possibly a minute amount of segregated In, appear to be sufficient though to fully wipe out the LEED pattern.

The average amount of In segregating on the top of the Fe film at RT can be estimated by comparing the Fe_{LMM} signals measured at the two growth temperatures, and assuming that the reduced intensity measured at RT is solely due to absorbtion in the In overlayer, of thickness d_{In} [Å]. In the hypothesis of a negligible amount of In segregated at LT, and assuming an attenuation of exponential form, the evolution of the peak-to-peak iron intensities at LT and RT, can be fitted with the following expressions, respectively (the dotted curves in Fig. 4.6(a),(b)):

$$I_{LT}^{Fe} = I_0^{Fe} \frac{1 - exp\left(-\frac{1.435\ t_{Fe}}{cos\phi\ \lambda_{Fe}^{Fe}}\right)}{1 - exp\left(-\frac{1.435}{cos\phi\ \lambda_{Fe}^{Fe}}\right)} \tag{5.1}$$

and

$$I_{RT}^{Fe} = I_0^{Fe} \frac{1 - exp\left(-\frac{1.435\ t_{Fe}}{cos\phi\ \lambda_{Fe}^{Fe}}\right)}{1 - exp\left(-\frac{1.435}{cos\phi\ \lambda_{Fe}^{Fe}}\right)}\ exp\left(-\frac{d_{In}}{cos\phi\ \lambda_{In}^{Fe}}\right) \tag{5.2}$$

In the above expressions, λ_{Fe}^{Fe} and λ_{In}^{Fe} are, respectively, the inelastic mean free paths (IMFP) in Fe (11.9 Å [98–100]) and In (18.3 Å [98]) of the 651 eV Fe_{LMM} Auger electrons. The AES signal given by one Fe monolayer, I_0^{Fe}, is deduced from the LT fit (Eq. 5.1), and is assumed the same at both growth temperatures. Therefore, from the RT

fit according to Eq. 5.2, the thickness of the In segregated layer was estimated to 2.0 ± 0.7 Å, which stands for about 1 ML (the lattice constant of tetragonal In is 4.59 Å). The error bars appear quite large, but one should keep in mind that the coverage dependence of the measured In peak-to-peak intensity at RT (the open triangles in Fig. 4.6(b)) does not support a constant amount of segregated In. Rather, one expects that an increasing amount of In comes to the top of the Fe film as its thickness increases, and saturates at about 1 ML for about 12 ML of deposited Fe. With further increasing the Fe thickness, the 1 ML thick In layer gradually becomes buried into the growing film.

5.3 Magnetic anisotropies

5.3.1 Perpendicular magnetic anisotropy in Fe on Au-covered Si(001)

The growth of Fe on Au-passivated Si(001) was shown in Chapter 3 to lead to the perpendicular orientation of magnetization in ultrathin films. To acquire some valuable insights into the mechanisms leading to this result, and to rule on the system's thermal stability, the behavior of ultra-thin films grown at LT was also investigated here with respect to annealing close to RT. The observed perpendicular magnetization in a very narrow thickness range after the ferromagnetic order sets in, can be accounted for, in principle, by pondering the competing anisotropy terms: while the surface anisotropy favors a perpendicular orientation of magnetization, the shape anisotropy tends to rotate the magnetization into the film plane [111]. The bilayer structure of the Fe/Au system demands the consideration of both thermodynamic and structural/compositional processes.

Generally, a perpendicularly magnetized film *in an applied field* can be phenomenologically described by the direction-dependent of the relevant thermodynamic potential, *i.e.*, the *enthalpy density*, as follows [112]:

$$G_0 = K_1 sin^2\theta + K_2 sin^4\theta + \frac{1}{2}\mu_0 M^2 cos^2\theta - \mu_0 H M cos\varphi \qquad (5.3)$$

where K_1 and K_2 stand, respectively, for the first and second order perpendicular uniaxial anisotropy contributions, and are continuous and continuously differentiable functions of temperature in the transition domains. In the above expression, all of the terms corresponding to the in-plane contribution were dropped. The third term in Eq. 5.3 is the stray field energy density which accounts for the demagnetizing field due to the

infinitely expanded, flat shape of the specimen, and the last term, known as the Zeeman term, favors the alignment of magnetization $\mathbf{M}$ along the external field $\mathbf{H}$. Here, θ and φ are defined as the angles between the direction of magnetization and, respectively, the normal to the film surface, and the direction of the applied field. Further, the anisotropy terms $K_{1,2}$ can be decomposed into volume and surface/interface contributions according to:

$$K_i = \; K_i^{volume} + \frac{1}{t} 2 K_i^{surface/interface}, \qquad i = 1, 2 \qquad (5.4)$$

with t, the film thickness. The minimization of the corresponding thermodynamic potential with respect to θ in the manner performed by Horner *et al.* [113] reveals the existence of three different thermodynamic phases associated with different values of θ: $\pi/2$ (in-plane phase), 0 (perpendicular phase), and $\arcsin \sqrt{-(K_1 - \frac{1}{2}\mu_0 M^2)/2K_2}$ (canted phase). Within this frame, the concept of *anisotropy flow* was developed by Millev and Kirschner [114] to account for the possible trajectories in the anisotropy phase diagram from the out-of-plane to in-plane configuration, either thickness or temperature driven [115]. In this phenomenological approach it was found that such spin reorientation takes place via the canted phase (reversible, second-order transition) or via an out-of-plane and in-plane phase coexistence (irreversible, first order transition). Moschel and Usadel [116] predicted the occurrence of the two temperature driven phase transitions by performing a mean-field analysis of a quantum model of Heisenberg spins. These authors deduced that the angle θ between the film normal and magnetization vector either increases continuously from 0 to $\pi/2$ (see also Ref. [111]) with increasing the temperature (first-order transition), or flips between 0 and $\pi/2$ at a given temperature (second-order transition). The later situation was shown to occur in the case of a monolayer film of given surface anisotropy, or in a multilayer film with a homogeneous distribution of the surface anisotropy.

Heinrich *et al.* [118] measured the surface anisotropy constants for the systems of interest here, *i.e.*, Fe(001)/Au and Fe(001)/vacuum, for different substrates and films thickness. They found a lower surface anisotropy in the case of Fe-Au interface ($0.40 \div 0.54 \times 10^{-3}$ J/m^2) than for the Fe-vacuum interface (0.96×10^{-3} J/m^2) at RT, but of the same sign, which points at the normal direction to the film plane as the most advantageous direction for magnetization. A slightly higher value was found by Elmers and Gradmann [119] in the case of Fe(110)/Au (0.72×10^{-3} J/m^2), but still smaller than the Fe-vacuum surface anisotropy. Therefore, the perpendicular orientation of magnetization is less favorable in the case of Fe-Au interface in comparison to the Fe-vacuum one. As

already mentioned, to rule on the orientation of magnetization one has to weigh up the competing anisotropy terms. However, such approach should be made with certain precautions in the case of the system under discussion here, at least for the actual saturation magnetization in the ultrathin Fe film might be significantly different than the bulk value (see for instance Ref. [120]). In addition, the higher order anisotropy term K_2 cannot be safely neglected since, as discussed above, it is responsible for the occurrence of the canted phase, a spin reorientation transition might pass through.

However, the perpendicular magnetization was observed at RT in an artificially fabricated FeAu alloy by Takanashi *et al.* [120]. Such compound does not exist in nature since, beside the vanishing solubility limit at RT, neither intermediate phases, nor intermetallic compounds form at equilibrium in the Fe-Au system. The structure of such crystalline phase is schematically depicted in Fig. 5.5. In their work, the alloy was prepared
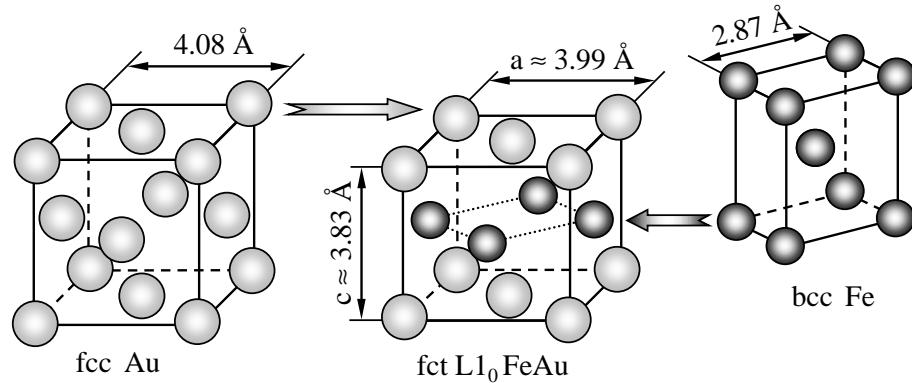
Figure 5.5: The face centered tetragonal $L1_0$ structure derived from the fcc Au and bcc Fe.

by sequential depositions of Au and Fe monolayers under UHV conditions on buffered MgO(001), and an ordered structure identical to the one of $L1_0$ FePt was found. It consists of alternating layers of Au and Fe building a face centered tetragonal (fct) structure with the lattice constants of $a \approx 3.99$ Å and $c \approx 3.83$ Å (Fig. 5.5) [121]. If the Au atoms do not contribute to the total magnetization, an enhanced magnetic moment per Fe atom of 2.75±0.25 μ_B was later deduced by the same authors [122], as compared to 2.2 μ_B, typical for an Fe atom in bulk bcc environment. As one can see in the following from the temperature and thickness dependence of magnetization in the Fe/Au/Si(001) system studied in this work, a superficial formation of the $L1_0$ FeAu phase can not be completely ruled out.

As shown in Chapter 3, the perpendicular ferromagnetic order in the films grown at

LT on Au-covered Si(001) was observed within about 1 ML of Fe above the magneti-
zation onset coverage (1.5 ML). The perpendicular magnetization occurs as the result
of the favorable anisotropy balance. A 2.3 ML thick Fe film was shown to preserve the
perpendicular orientation of magnetization (Fig. 3.15(a)) upon annealing close to RT. For
no switching to in-plane magnetization was observed, one can conclude that the Curie
temperature, T_C, of the 2.3 ML thick film is well above 280 K. This assertion is based on
the findings of Moschel and Usadel [116], who predicted a switching temperature between
$\approx 0.34 T_C$ and $\approx 0.79 T_C$ as the ratio between the strength of the surface anisotropy and
the dipole interaction increases.

If the Fe thickness of the LT grown film approaches 3 ML, the magnetization reorients
from the perpendicular to the in-plane direction. This means that, for this particular
thickness, the switching temperature equals the growth temperature. The decrease of the
switching temperature with increasing thickness was observed more than a decade ago
in ultrathin Fe films by Pappas and coworkers [123]. This behavior is due to a reduced
influence of the surface anisotropy in comparison to the one of the dipole interaction as
the film thickness is increased. Eventually, at a certain thickness, the surface anisotropy
and the shape anisotropy cancel each other resulting in a state with vanishing anisotropy,
and the film is expected to undergo a continuous transition to a vortex spin structure via
a twisted spin configuration [124].

A 3 ML thick Fe film grown at LT on Au-covered Si(001) which completed the transi-
tion from the perpendicular to the in-plane magnetization state was characterized in Chap-
ter 3 with respect to the magnetization behavior upon annealing close to RT (Fig. 3.15(b)).
The main result of the thermal treatment is the retrieval of the perpendicular orientation
of magnetization as the temperature increased. This behavior is thermodynamically for-
bidden, unless this transition is accompanied by structural and/or compositional changes.
Earlier, Liu and Bader [68] found that an initially out-of-plane magnetized ≈ 2 ML thick
Fe film grown at 100 K on Au(001) reorients irreversibly its magnetization in the film
plane upon annealing at 300 K, and they suggested that the Au-Fe intermixing is re-
sponsible for this behavior [117]. As a matter of fact, there is no conflict between these
early results and the temperature driven out-of-plane reorientation of magnetization in
the 3 ML thick Fe film grown at LT on Au-covered Si(001) observed here, since the chem-
istry of the by-layer structure of the latter has to be taken into account. Accordingly,
it appears very plausible that a temperature driven phase transition, possibly connected
to a superficial formation of the $L1_0$ FeAu phase due to Au out-diffusion, leads to the

observed out-of-plane magnetization at RT. Since such unusual behavior was not observed in the case of Fe grown on Au(001), one may point at the peculiar morphology of the buffer film grown here on the reconstructed Si(001) as its main cause.

In the following, it will be proven that a Au cap layer can indeed force the perpendicular orientation of magnetization in ultrathin Fe films grown at LT on Au-covered Si(001). Such manipulation of magnetization direction is illustrated by the sequence of loops shown in Fig. 5.6. Initially, a 2.5 ML thick Fe film was grown at $\approx$150 K on Au-covered Si(001).
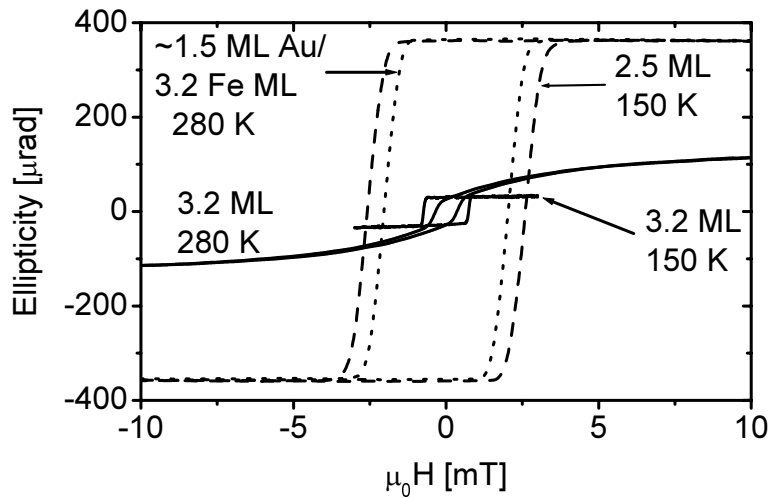
Figure 5.6: An out-of-plane magnetized $\approx$2.5 ML thick Fe film grown on Au-covered Si(001) at 150 K (dashed line) becomes in-plane magnetized at $\gtrsim$3.2 ML (solid line). The in-plane orientation of magnetization is preserved upon annealing at 280 K (solid line) and reorients out of the film plane after $\approx$1.5 ML of Au are deposited at the same temperature (dotted line).

As expected, the out-of-plane magnetization observed for this thickness (dashed line in Fig. 5.6) fliped into the film plane with increasing the thickness at $\approx$3.2 ML. The corresponding low-ellipticity square-like loop is drawn with a solid line in Fig. 5.6 and marked accordingly. Note that the Fe thickness is slightly higher here than the one of the in-plane magnetized film in Fig. 3.15(b). Upon annealing up to 280 K, the film appears to have preserved the in-plane orientation of magnetization as deduced from the measurement of a low ellipticity loop (the accordingly marked solid line in Fig. 5.6). The loop is strongly elongated and saturates by applying fields exceeding 10 mT at more than 100 μrad. Therefore, it seems that the magnetization was rotated out-of-plane by increasing the applied field, slightly misorientated with respect to the film plane. This finding is in contrast to the observation of a clear out-of-plane MOKE signal in the case of a slightly

thinner Fe film annealed at ≈270 K as described in the previous paragraph. One can observe here that the perpendicular magnetization occurs indeed under some very strict conditions. The film was afterwards capped with about 1.5 ML of Au at 280 K, and the out-of-plane orientation of magnetization was retrieved (the dotted line in Fig. 5.6). A MOKE signal as strong as the one measured for the perpendicularly magnetized 2.5 ML thick Fe film at LT was obtained. According to this result, it is obvious that the perpendicular magnetization is induced by the Au cap layer, *i.e.*, the Au/Fe interface seems to exhibit a *higher* anisotropy than the vacuum/Fe one. Since no LEED pattern was observed neither before nor after capping, one can hardly conclude on the nature of phase transition undergone by the film, but appears to have a strong compositional component.

Therefore, by an appropriate tuning of the growth and annealing temperatures, as well as of the films thickness and sequence, the orientation of magnetization can be rotated either out-of- or in the film plane at least for several ML thick films. The origin for the onset of perpendicular magnetization in such films is not fully accounted for. Magnetization flips into the film plane with increasing the Fe thickness, and no measurable in-plane magnetic anisotropy was observed for the whole thickness range investigated. This was deduced by observing the MOKE loops for different orientations of the sample with respect to the direction of the magnetic field.

The possibility of fabricating films with perpendicular magnetization on Si(001), which are magnetically "alive" almost throughout the whole thickness, opens new perspectives for the potential implementation of the system in magnetoelectronic applications. For instance, one should emphasize that tremendous progress has been recently made in the field of magnetic random access memories (MRAM's) by integrating magneto-tunnel junction (MTJ) structures with the silicon technology [125]. Since the manipulation of the magnetization direction in the ferromagnetic elements building such MTJ's appears possible, one enables additional degrees of freedom in operating the MRAM's units. Therefore, this field is expected to be among the first ones gaining significant benefits.

5.3.2 Uniaxial in-plane magnetic anisotropy in Fe on InP(001)

A thermodynamic potential with the direction dependent terms similar to the ones used in the previous section (see Eq. 5.3) can be employed here to account for the observed in-plane uniaxial magnetic anisotropy in the Fe films grown on InP(001). However, θ represents in this case the angle between the direction of magnetization and the in-plane

easy axis. In addition, for the present discussion, one can safely take into account only the first order anisotropy constant, which will be simply denominated as the uniaxial in-plane anisotropy constant K_u.

From the saturation field of the pure rotation loops measured along [110] (Fig. 4.7(a),(c)), the magnitude of the in-plane uniaxial magnetic anisotropy constant at the onset coverage was estimated [126]: $K_u = I_s B_s/2\mu_0 \approx 1.2 \times 10^4$ J/m^3 for films grown at ≈ 150 K and $\approx 0.8 \times 10^4$ J/m^3 in the RT growth case (see the lowest coverage data points in Fig. 5.7(a)). In the above approach, I_s stands for the saturation magnetization of iron (2.16 T), and B$_s$ [T] for the magnetic flux density necessary to fully rotate the magnetization along [110]. For comparison, one can notice that the measured K_u values in both LT and RT growth cases are much lower than the magnetocrystalline fourfold magnetic anisotropy, K_1, for unstrained bcc Fe at RT (4.72×10^4 J/m^3). The stronger anisotropy found here for films grown at LT suggests a sharper interface than in the RT case. In the first growth stages shortly after the ferromagnetic order sets in, an increase in the strength of the in-plane magnetic anisotropy constant can be seen in Fig. 5.7(a) regardless of the growth temperature. The weakened anisotropy observed for the very thin films is due to the measurements being performed close to their Curie temperatures. As the films thickness are increased, their Curie temperature rises, and the measured anisotropies reach their maxima at ≈ 3.5 ML for films grown at LT and ≈ 5 ML in the RT growth case. Afterwards, a monotonous decrease of the anisotropy strength with increasing coverage can be observed (Fig. 5.7).

The anisotropy constants K_u found here might vary from one sample to another, although prepared under similar conditions, pointing at the important role played by the substrates' actual degree of perfection in establishing the strength of the in-plane magnetic uniaxial anisotropy. In addition, variations in the evaporation rate, together with the different delay times necessary to perform the measurements themselves may produce a certain influence on the surface relaxation processes affecting the measured magnetic anisotropy. These facts complicate a precise quantitative interpretation of the anisotropy data shown in Fig. 5.7.

If the anisotropy K_u of a thin film can be described by a single constant K_V in terms of energy per unit volume, than for the unity of area, the total anisotropy energy, $K_u t$, per unit area should be proportional to film thickness t according to

$$K_u t \propto K_V t. \tag{5.5}$$
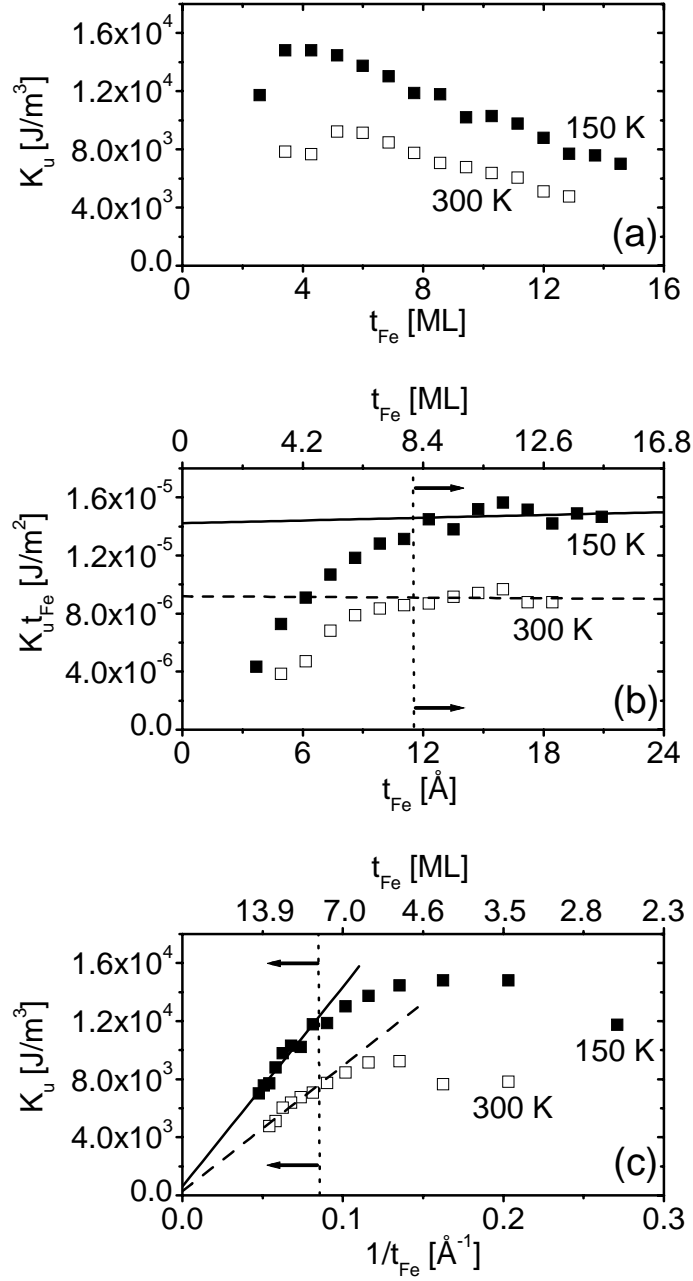
Figure 5.7: The coverage dependence of: (a) the in-plane magnetic anisotropy constant, K_u, and (b) K_u times the film thickness, t_{Fe}. (c): the dependence of the in-plane magnetic anisotropy constant, K_u, with respect to inverse coverage, $1/t_{Fe}$. The solid and dashed lines stand for linear fits of the anisotropy data points above ≈ 8 ML in the case of ≈ 150 K (the solid squares) and ≈ 300 K (the open squares) growth temperatures.

Obviously, the plots shown in Fig. 5.7(a) for the two growth temperatures do not meet this expectation. If the interfaces contribute to the total anisotropy (generally, with not the same amount for each of the two interfaces), these should add a term which is independent of thickness, namely K_I, defined in terms of energy per unit area. With the new contribution, the relation (5.5) transforms now into

$$K_u t = K_V t + K_I. \tag{5.6}$$

Therefore, the measured $K_u t_{Fe}$ values for the two growth temperatures are plot as a function of thickness t_{Fe} in Fig. 5.7(b). These plots show an initial increase, then saturate at constant values. The constants mean that for large thicknesses the volume dependent uniaxial anisotropy becomes vanishingly small, or even zero in both cases. The values of these constants may be associated with the interface anisotropy K_I and will be labelled as $K_I^{(b)}$ (derived from plot (b) in Fig. 5.7).

Alternatively, Eq. 5.6 may be rewritten as:

$$K_u = K_V + \frac{1}{t_{Fe}} K_I. \tag{5.7}$$

This representation is rather popular, but can be misleading: if one plots K_u *vs.* $1/t_{Fe}$, one often observes curves with two approximately linear slopes. Such behavior can be clearly seen here at both growth temperatures (Fig. 5.7(c)). Therefore, one needs a criterion to tell us which slope should be considered for the extrapolation to $t_{Fe} \to \infty$ or $1/t_{Fe} \to 0$. The intersection with the K_u axis for $1/t_{Fe} \to 0$ yields, according to Eq. 5.7, the volume anisotropy, while the slope yields the interface contribution. The needed criterion is provided by the plots in Fig. 5.7(b), which show that for large thicknesses (*i.e.*, $1/t_{Fe} \to 0$) the volume anisotropy becomes very small or zero, as it should be, for there is no uniaxial volume contribution to the total magnetic anisotropy in the unstrained bulk bcc Fe. Therefore, the extrapolations must be done on the left hand side of the plots in Fig. 5.7(c), yielding volume anisotropies, $K_V^{(c)}$, of $0.6 \pm 0.8 \times 10^3$ J/m^3 for films grown at 150 K and $0.3 \pm 0.9 \times 10^3$ J/m^3 for the 300 K growth case. The slopes yield the interface contributions, $K_I^{(c)}$, of $13.8 \pm 1.3 \times 10^{-6}$ J/m^2 at 150 K and $8.7 \pm 1.3 \times 10^{-6}$ J/m^2 at 300 K. If the results are consistent, the values for $K_I^{(b)}$ from the plots in Fig. 5.7(b) and $K_I^{(c)}$ from the plots in Fig. 5.7(c) must agree. Indeed, the comparison shows that they agree to within ± 3 % at 150 K ($K_I^{(b)} = 14.2 \pm 1.3 \times 10^{-6}$ J/m^2) and ± 6 % at 300 K ($K_I^{(b)} = 9.2 \pm 1.3 \times 10^{-6}$ J/m^2). The same reasoning is found to hold for $K_V^{(b)}$ ($0.3 \pm 0.8 \times 10^3$ J/m^3 at 150 K and $0.0 \pm 0.9 \times 10^3$ J/m^3 at 300 K) and $K_V^{(c)}$, which agree

to within $\approx 0.3 \times 10^3$ J/m^3. These values are about two orders of magnitude smaller than the magnetocrystalline fourfold magnetic anisotropy for unstrained bcc Fe at RT (4.72×10^4 J/m^3). One should make the remark that these results may not be obtained from the plots in Fig. 5.7(a) which seem to indicate a $1/t_{Fe}$ behavior with thickness. The important result of an approximate separation into thickness-dependent and thickness-independent terms above about 8 ML cannot be derived from the plots in Fig. 5.7(a). Films thinner than $\approx$8 ML appear to undergo modifications which prevent an extension of the analysis closer to the magnetization onset coverage. However, another important result is that, in contrast to the lack of any LEED pattern, the uniaxial behavior of magnetization infers some order in the growing film or the interface.

In the above analysis, a distinction between the contributions of the two film interfaces is hard to be made. In addition, the separation of the K_u in a volume contribution and an interface one is, generally, questionable for a few ML thick films, but also throughout the whole thickness of certain thicker films, as for instance in the case of Ni on Cu(001) [127]. Another factor which may obscure the linear dependence is the departure of the actual magnetization saturation from the bulk value due to the different film structure and chemical environment in ultrathin films. These facts, together with the Curie temperature effect, should restrict the data interpretation to film thicknesses of several monolayers above the magnetization onset coverage.

As described in the previous section, the two different growth temperatures give rise to the growth of Fe films whose interfaces are significantly different. While vacuum (and possibly some In)/Fe/P-rich InP(001) interfaces are encountered in the LT grown films, In/Fe/P-rich InP(001) interfaces are obtained in the RT case. The presence of segregated In and possibly an increased amount of P present at the RT grown film/substrate interface might lead to a disordered interface which potentially reduces the strength of the magnetic anisotropy. In contrast to the vanishing of the LEED pattern regardless of the deposition temperature, this fact points at the role of the uniaxial reconstruction of the substrate's surface. It seems that the uniaxial order at the interface is kept, which causes the uniaxial surface/interface anisotropy. In the RT case, some intermixing/segregation occurs, probably due to a larger scale disruption of the substrate's dimers by the Fe adatoms. Thus, the uniaxial character of the interface is accordingly reduced.

The uniaxial magnetic anisotropy observed in the Fe/InP(001), and the possibility of rotating the direction of the easy and hard axis of magnetization is of great importance to applications. The fabrication of devices whose operation principle relies on electronic

transport through magnetic multilayer structures (*e.g.* MRAM and the spin-valve transistor) will strongly benefit from the use of systems with tunable anisotropy. If only the issue of data storage media is concerned, the uniaxial anisotropy appears extremely useful, since two well defined magnetization states, either "1" or "0", can be obtained.

Chapter 6

Summary and conclusions

The aim of this work is to give an account on the possible implementation of two ferromagnet-semiconductor systems, namely Fe-Si and Fe-InP, into the new field of spin-electronics. The technologically relevant (001) surface of the substrates used for films growth were investigated here with respect to their structural and morphological properties. Concerning the Fe growth, it was shown that, under certain conditions, the reaction between films and substrates can be reduced. With the ingredient of a strong magnetic anisotropy, new application opportunities are opened for the studied systems.

First of all, a review on the Si(001) surface and on the growth of Fe on (2×1) Si(001) was given. The strong intermixing in the case of room temperature (RT $\cong$ 300 K) growth takes place at least up to about 10 ML of deposited Fe, and results in the formation of a ferromagnetically ordered iron silicide film. The onset of magnetization was detected at RT by magneto-optic Kerr effect (MOKE) only after the deposition of about 3.6 ML of Fe. The low temperature (LT $\cong$ 150 K) growth yields an earlier onset of magnetization at slightly less than 2.5 ML of Fe, partly as the result of the temperature inhibited reactivity of the Si(001) surface. However, it is deduced that the reduction of intermixing in this case is only minute.

To further inhibit the reaction, a ultrathin Au film grown in two steps was used as passivation layer. First, less than 1 ML of Au was deposited at high temperatures (HT $\gtrsim$ 1000 K) on Si(001). A complex reconstruction of the surface was induced, which is characterized by a drastic reshaping of the surface topography into rectangular-like terraces separated by single and multiple steps. The rearrangement of the surface atoms gives rise to the occurrence of a mixture of phases built from both Au and Si atoms.

Second, an additional ultra thin Au layer of about 1.5 ML has been employed to limit the Si diffusion into the Fe film. With this buffer layer, the magnetization always sets in with the magnetic moment oriented out-of-plane, regardless of the deposition temperature, at Fe coverages of slightly less than 4 ML at RT and about 1.5 ML at 150 K. The early onset of magnetization observed in the last case, along with the absence of any sharp feature at 10 ML in the plot of the largely enhanced Kerr signal at saturation *vs.* coverage points at the successful hampering of silicide formation and the growth with virtually zero magnetically dead layers. A 2.3 ML thick Fe film grown at LT on Au-covered Si(001) is shown to be thermally stable upon annealing up to 280 K. This is confirmed by the preservation of the perpendicular orientation of magnetization and by the reversible behavior of the MOKE signal's magnitude upon completing the thermal cycle.

The origin of the out-of-plane magnetization found in ultra-thin films at both RT and LT cannot be solely treated in terms of film surface/interface anisotropy. Therefore, modifications in the film structure and composition should be considered. This assertion is based on the observation of a transition from the in-plane to perpendicular magnetization upon annealing close to RT in 3 ML thick Fe films grown at LT on Au-covered Si(001). Since such reorientation is thermodynamically prohibited in thin films, thermally driven Au out-diffusion leading to chemical and structural changes in the grown film might be responsible for the observed behavior. These results open the possibility of growing stable and almost silicide free thin Fe films on Si(001) by simply employing a noble metal-passivation layer. The use of a thin Au buffer layer alleviates the problems associated with silicide formation and allows the manipulation of the magnetization direction in the Fe film.

Prior to the growth and magnetic characterization of thin Fe films grown on InP(001) at ≈ 150 and ≈ 300 K, the surface reconstruction of Ar^+ sputtered InP(001) was investigated. The surface reconstruction observed here is assigned to the P-rich (2×4) phase whose microstructure is associated with the existence of a mixed In-P dimer on the topmost layer. The different packing configurations of the (2×4) units occurring as the result of different sequences of mixed In-P dimers are strongly supported by the experimental results presented in this work, being aware of the likely formation of additional configurations and phases.

The growth of ultra-thin Fe films on P-rich (2×4) InP(001) proceeds as 2D islands up to about 0.4 ML, and no hints about any in-plane preferred growth direction was

found. Thereafter, 3D islands start to grow, which subsequently coalesce as the amount of deposited Fe increases. No LEED pattern can be seen any longer as the film thickness exceeds 1 ML regardless of the growth temperature. In the RT growth case, this may be due to the segregation of a monolayer of In on the growing film at RT as found by AES, which probably induces a high degree of disorder at the surface. A reduced growth temperature leads to an even more disordered film, for no LEED pattern was seen in the context of a negligible amount of segregated In. However, the AES investigation performed in this study does not point at a *strong* intermixing between the Fe film and InP(001) leading to a large scale formation of Fe phosphide.

The films show a good ferromagnetic order with a strong uniaxial in-plane magnetic anisotropy up to an Fe thickness of about 15 ML at ≈150 K and 13 ML at ≈300 K with the easy axis along substrate [$\bar{1}10$] direction. This observation infers some order in the grown film, in contrast to the lack of any LEED pattern. The uniaxial character of the underlying (2×4) substrate reconstruction is found responsible for the onset of the uniaxial magnetic anisotropy. A stronger surface/interface anisotropy was deduced at LT ($14.0 \pm 1.5 \times 10^{-6}$ J/m^2) in comparison to the RT growth case ($9.0 \pm 1.5 \times 10^{-6}$ J/m^2). No perpendicular magnetization was observed for the whole thickness range investigated at either growth temperature. While less than one ML is found magnetically dead in the case of RT growth, all of the LT grown layers are proven to be magnetically alive. In addition to the onset of a magnetic interface, the RT grown Fe film - n-type InP(001) system is characterized by a non-rectifying contact.

The experimental findings presented in this work support the potential employment of the investigated systems in integrated solid-state spintronic devices as pointed out in the introductory chapter. A magnetic interface is highly desirable for a longer spin life-time is expected to be encountered in such layer. Moreover, spin polarized electrons can also be generated within this layer, or it can act as a spin filter by itself, whose direction of magnetization can be manipulated according to specific needs.

Bibliography

[1] S. Datta, B. Das, *Appl. Phys. Lett.* **56** (7), 665 (1990).

[2] G. A. Prinz, *Physics Today* **48** (4), 58 (1995); J. L. Simonds, *Physics Today* **48** (4), 26 (1995); E. D. Dahlberg, J.-G. Zhu, *Physics Today* **48** (4), 34 (1995); D. D. Awschalom, D. P. Di Vincenzo, *Physics Today* **48** (4), 43 (1995); H. J. F. Jansen, *Physics Today* **48** (4), 50 (1995).

[3] G. Schmidt, D. Ferrand, L. W. Molenkamp, A. T. Filip, B. J. van Wees, *Phys. Rev. B* **62** (8) R4790 (2000).

[4] R. Fiederling, M. Keim, G. Reuscher, W. Ossau, G. Schmidt, A. Waag, L. W. Molenkamp, *Nature* **402**, 787 (1999).

[5] W. C. Black Jr., B. Das, *J. Appl. Phys.* **87**, 6674 (2000).

[6] D. J. Monsma, R. Vlutters, J. C. Lodder, *Science* **281**, 407 (1998).

[7] P. S. Anil Kumar, J. C. Lodder, *J. Phys. D: Appl. Phys.* **33**, 2911 (2000).

[8] R. Cao, K. Miyano, I. Lindau, W. E. Spicer, *J. Elec. Spectrosc.* **51**, 581 (1990).

[9] R. H. Williams, A. McKinley, G. J. Hughes, T. P. Humphreys, *J. Vac. Sci. Technol. B* **2** (2), 561 (1984).

[10] L. J. Brillson, C. F. Brucker, *J. Vac. Sci. Technol.* **21**, 564 (1982).

[11] J. M. Gallego, R. Miranda, *J. Appl. Phys.* **69**, 1377 (1991).

[12] G. Crecelius, *Appl. Surf. Sci.* **65/66**, 683 (1993).

[13] M. C. Bost, J. E. Mahan, *J. Appl. Phys* **58**, 2696 (1985).

[14] J. E. Mahan, K. M. Geib, G. Y. Robinson, R. G. Long, Y. Xinghua, G. Bai, M. A. Nicolet, M. Nathan, *Appl. Phys. Lett.* **56**, 2126 (1990).

[15] J. Alvarez, J. J. Hinarejos, E. G. Michel, J. M. Gallego, A. L. Vazquez de Parga, J. de la Figuera, C. Ocal, R. Miranda, *Appl. Phys. Lett.* **59**, 99 (1991).

[16] J. M. Gallego, J. M. Garcia, J. E. Ortega, A. L. Vazquez de Parga, J. de la Figuera, C. Ocal, R. Miranda, *Surf. Sci.* **269/270**, 1016 (1992).

[17] J. M. Gallego, J. M. Garcia, J. Alvarez, R. Miranda, *Phys. Rev. B* **46**, 13339 (1992).

[18] E. Kaxiras, *Phys. Rev. B* **43**, 6824 (1991).

[19] W. Yajun, R. J. Hamers, E. Kaxiras, *Phys. Rev. Lett.* **74**, 403 (1995).

[20] M. K. Weilmeier, W. H. Rippard, R. A. Buhram, *Phys. Rev. B* **59**, R2521 (1999).

[21] K. Mizushima, T. Kinno, K. Tanaka, T. Yamauchi, *Phys. Rev. B* **58**, 4660 (1998).

[22] K. Oura, Y. Makino, T. Hanawa, *Jpn. J. of Appl. Phys.* **15**, 736, (1976).

[23] K. Oura, T. Hanawa, *Surf. Sci.* **82**, 202 (1979).

[24] N. Newman, T. Kendelewicz, L. Bowman, W. E. Spicer, *Appl. Phys. Lett.* **46** (12), 1176 (1985).

[25] T. Kendelewicz, N. Newman, R. S. List, I. Lindau, W. E. Spicer, *J. Vac. Sci. Technol. B* **3** (4), 1206 (1985).

[26] R. S. List, T. Kendelewicz, M. D. Williams, I. Lindau, W. E. Spicer, *J. Vac. Sci. Technol. A* **3** (3), 1002 (1985).

[27] G. J. Hughes, P. Ryan, A. A. Cafolla, P. Quinn, *Appl. Surf. Sci.* **147**, 201 (1999).

[28] see for instance J. C. Rivière, *Contemp. Phys.* **14** (6) 513 (1973).

[29] P. Auger, *Comptes Rendus de l'Acadmie des Sciences* **180**, 65 (1925).

[30] J. J. Lander, *Phys. Rev.* **91** (6) 1382 (1953).

[31] M. F. Chung, L. H. Jenkins, *Surf. Sci.* **22**, 479 (1970).

[32] L. A. Harris, *J. Appl. Phys.* **39**, 1419 (1968).

[33] P. W. Palmberg, G. K. Bohn, J. C. Tracy, *Appl. Phys. Lett.* **15**, 254 (1969).

[34] J. B. Pendry, *Low Energy Electron Diffraction*, Academic Press, London (1974).

[35] see for instance J. M. Cowley, *Diffraction Physics*, North-Holland Publishing Company, Amsterdam (1985).

[36] see for instance L. J. Clarke, *Surface Crystalography*, Wiley and Sons, Chichester (1985).

[37] M. Henzler, in *Dynamical Phenomena at Surfaces, Interfaces and Superlattices*, eds. F. Nizzoli, K. H. Rieder, R. F. Willis, Springer Ser. Surf. Sci. 3, Springer Verlag, Berlin (1986), and references therein.

[38] J. Wollschläger, J. Falta, M. Henzler, *Appl. Phys. A* **50**, 57 (1990).

[39] G. Binning, H. Rohrer, C. Gerber, E. Weibel, *Appl. Phys. Lett.* **40**, 178 (1982); G. Binning, H. Rohrer, C. Gerber, E. Weibel, *Phys. Rev. Lett.* **49**, 57 (1982); G. Binning, H. Rohrer, C. Gerber, E. Weibel, *Physica B* **109-110**, 2075 (1982).

[40] G. Binning, H. Rohrer, *Helv. Phys. Acta* **55**, 726 (1982); G. Binning, H. Rohrer, *Surf. Sci.* **126**, 236 (1983).

[41] N. Garcia, C. Ocal, F. Flores, *Phys. Rev. Lett.* **50** (25) 2002 (1983).

[42] J. Bardeen, *Phys. Rev. Lett.* **6** (2) 57 (1961).

[43] J. Tersoff, D. R. Hamann, *Phys. Rev. B* **31**, 805 (1985).

[44] see the works of N. D. Lang in *Phys. Rev. Lett.* **55**, 230 (1985), *Phys. Rev. Lett.* **56**, 1164 (1986), *Phys. Rev. Lett.* **58**, 45 (1987), *Phys. Rev. B* **34**, 5947 (1986).

[45] P. N. Argyres, *Phys. Rev.* **97** (2) 334 (1955).

[46] H. R. Hulme, *Proc. Roy. Soc.* **A135**, 237 (1932).

[47] J. Zak, E. R. Moog, C. Liu, S. D. Bader, *J. Magn. Magn. Mater.* **88**, L261 (1990), and in *J. Magn. Magn. Mater.* **89**, 107 (1990).

[48] P. Ma, G. W. Anderson, P. R. Norton, *Surf. Sci* **420**, 134 (1999).

[49] P. Bertoncini, P. Wetzel, D. Berling, G. Gewinner, C. Ulhaq-Bouillet, V. Pierron Bohnes, *Phys. Rev. B* **60**, 11123 (1999).

[50] R. E. Schlier, H. E. Farnsworth, *J. Chem. Phys.* **30**, 917 (1959).

[51] D. J. Chadi, *Phys. Rev. Lett.* **59**, 1691 (1987).

[52] V. A. Ukraintsev, J. T. Yates, Jr. *Surf. Sci.* **346**, 31 (1996), and references therein.

[53] M. J. Cardillo, G. E. Becker, *Phys. Rev. B* **21**, 1497 (1980).

[54] R. M. Tromp, R. J. Hamers, J. E. Demuth, *Phys. Rev. Lett.* **55**, 1303 (1985).

[55] M. C. Payne, N. Roberts, R. J. Needs, M. Needels, J. D. Joannopoulos, *Surf. Sci.* **211/212**, 1 (1989).

[56] A. García, J. E. Narthrup, *Phys. Rev. B* **48**, 17350 (1993).

[57] R. A. Wolkow, *Phys. Rev. Lett.* **68**, 2636 (1992).

[58] H. J. W. Zandvliet B. S. Swartzentruber, W. Wulfhekel, B. J. Hattink, B. Poelsema, *Phys. Rev. B* **57**, R6803 (1998).

[59] R. J. Hamers, R. M. Tromp, J. E. Demuth, *Phys. Rev. B* **34**, 5343 (1986).

[60] R. Kläsges, C. Carbone, W. Eberhardt, C. Pampuch, O. Rader, T. Kachel, W. Gudat, *Phys. Rev. B* **56**, 10801 (1997).

[61] D. P. Adams, L. L. Tedder, T. M. Mayer, B. S. Swartzentruber, E. Chason, *Phys. Rev. Lett.* **74**, 5088 (1995).

[62] Z. H. Nazir, C.-K. Lo, M. Hardiman, *J. Magn. Magn. Mater.* **156**, 435 (1996).

[63] T. Shimakura, H. Minoda, Y. Tanishiro, K. Yagi, *Surf. Sci.* **407**, L657 (1998).

[64] S. D. Bader, E. R. Moog, *J. Appl. Phys.* **61**, 3729 (1987).

[65] X. F. Lin, K. J. Wan, J. C. Glueckstein, J. Nogami, *Phys. Rev. B* **47**, 3671 (1993).

[66] S. D. Bader, E. R. Moog, P. Grünberg, *J. Magn. Magn. Mater.* **53**, L295 (1986).

[67] W. Dürr, M. Taborelli, O. Paul, R. Germar, W. Gudat, D. Pescia, M. Landolt, *Phys. Rev. Lett.* **62**, 206 (1989).

[68] C. Liu, S. D. Bader, *J. Vac. Sci. Technol. A* **8**, 2727 (1990).

[69] V. Blum, Ch. Rath, S. Müller, L. Hammer, K. Heinz, J. M. García, J. E. Ortega, J. E. Prieto, O. S. Hernán, J. M. Gallego, A. L. Vázquez de Parga, R. Miranda, *Phys. Rev. B* **59**, 15966 (1999).

[70] N. D. Mermin, H. Wagner, *Phys. Rev. Lett.* **17**, 1133 (1966).

[71] E. Weman, A. Henry, T. Begum, B. Monemar, O. O. Awadelkarim, J. L. Lindström, *J. Appl. Phys.* **65**, 137 (1990); see also *Handbook of semiconductor silicon technology*, Eds. W. C. O'Mara, R. B. Herring, L. P. Hunt, Noyes Publ., U.S.A., 399 (1990).

[72] C. D. MacPherson, R. A. Wolkow, C. E. J. Mitchell, A. B. McLean, *Phys. Rev. Lett.* **77**, 691 (1996).

[73] Q. Guo, M. E. Pemble, E. M. Williams, *Surf. Sci.* **468**, 92 (2000).

[74] H. H. Farrell, J. P. Harbison, L. D. Peterson, *J. Vac. Sci. Technol. B* **5**, 1482 (1987).

[75] D. J. Chadi, *J. Vac. Sci. Technol. A* **5**, 834 (1987).

[76] M. D. Pashley, *Phys. Rev. B* **40**, 10481 (1989).

[77] J. E. Northrup, S. Froyen, *Phys. Rev. B* **50**, 2015 (1996).

[78] N. Esser, U. Resch-Esser, M. Pristovsek, W. Richter, *Phys. Rev. B* **53**, R13257 (1996).

[79] C. Goletti, N. Esser, U. Resch-Esser, V. Wagner, J. Foeller, M. Pristovsek, W. Richter, *J. Appl. Phys.* **81**, 3611 (1997).

[80] T. K. Johal, S. D. Barrett, M. Hopkinson, P. Weightman, J. R. Power, *J. Appl. Phys.* **83**, 480 (1998).

[81] W. G. Schmidt, F. Bechstedt, N. Esser, M. Pristovsek, Ch. Schultz, W. Richter, *Phys. Rev. B* **57**, 1496 (1998).

[82] K. B. Ozanyan, P. J. Parbrook, M. Hopkinson, C. R. Whitehouse, Z. Sobiesierski, D. I. Westwood, *J. Appl. Phys.* **82**, 474 (1997).

[83] B. X. Yang, H. Hasegawa, *Jpn. J. Appl. Phys.* **33** 1 (1b), 742 (1996).

[84] M. T. Norris, *Appl. Phys. Lett.* **34**, 282 (1980).

[85] M. Zorn, T. Trepk, J.-T. Zettler, B. Junno, C. Meyne, K. Knorr, T. Wethkamp, M. Klein, M. Miller, W. Richter, L. Samuelson, *Appl. Phys. A* **65**, 333 (1997).

[86] L. Li, B.-K. Han, Q. Fu, R. F. Hicks, *Phys. Rev. Lett.* **82**, 1879 (1999).

[87] L. Li, B.-K. Han, D. Law, C. H. Li, Q. Fu, R. F. Hicks, *Appl. Phys. Lett.* **75**, 683 (1999).

[88] P. Vogt, Th. Hannappel, S. Visbeck, K. Knorr, N. Esser, W. Richter, *Phys. Rev. B.* **60**, R5117 (1999).

[89] L. Li, Q. Fu, C. H. Li, B.-K. Han, R. F. Hicks, *Phys. Rev. B* **61**, 10223 (2000).

[90] T. Kawamura, Y. Watanabe, Y. Utsumi, K. Uwai, J. Matsui, Y. Kagoshima, Y. Tsusaka, S. Fujikawa, *Appl. Phys. Lett.* **77**, 996 (2000).

[91] Th. Hannappel, S. Visbeck, K. Knorr, J. Mahrt, M. Zorn, F. Willig, *Appl. Phys. A.* **69**, 427 (1999).

[92] S. Mirbt, N. Moll, K. Cho, J. D. Joannopoulos, *Phys. Rev. B* **60**, 13283 (1999).

[93] J. M. Moison, M. Bensoussan, *Surf. Sci.* **169**, 68 (1986).

[94] W. Weiss, R. Hornstein, D. Schmeisser, W. Gpel, *J. Vac. Sci. Technol. B* **8**, 715 (1990)

[95] M. M. Sung, C. Kim, H. Bu, D. S. Karpuzov, J. W. Rabalais, *Surf. Sci.* **322**, 116 (1995).

[96] P. M. Thibabo, E. Kneedler, B. T. Jonker, B. R. Bennett, B. V. Shanabrook, L. J. Whitman, *Phys. Rev. B* **53**, R10481 (1996).

[97] G. W. Anderson, M. C. Hanf, X. R. Qin, P. R. Norton, K. Myrtle, B. Heinrich, *Surf. Sci.* **346**, 145 (1996); M. Gester, C. Daboo, S. J. Gray, J. A. C. Bland, *J. Magn. Magn. Mater.* **165**, 242 (1997).

[98] S. Tanuma, C. J. Powell, D. R. Penn, *Surf. Interface Anal.* **17**, 911 (1991).

[99] C. M. Kwei, Y. F. Chen, C. J. Tung, J. P. Wang, *Surf. Sci.* **293**, 202 (1993).

[100] W. H. Gries, *Surf. Interface Anal.* **24** (1) 38 (1996).

[101] M. Gester, C. Daboo, R. J. Hicken, S. J. Gray, A. Ercole, J. A. C. Bland, *J. Appl. Phys.* **80**, 347 (1996).

[102] H. J. Elmers, U. Gradmann, *Surf. Sci.* **304**, 201 (1994) and references herein.

[103] A. J. P. Meyer, M. C. Cadeville, *J. Phys. Soc. Jpn.* **17** (Suppl. B-I), 223 (1962); K. Huller, G. Dietz, R. Hausmann, K. Kolpin, *J. Magn. Magn. Mater.* **53**, 103 (1985).

[104] see for instance *Binary alloy phase diagrams*, vol. 2, 2nd edition, Ed.-in-chief T. B. Massalski, Publisher W. W. Scott, Jr., U.S.A., 1746 (1996).

[105] see for instance the review of L. Magaud and F. Cyrot-Lackmann in *Encyclopedia of Aplied Physics* Vol. 16, VCH Publishers, Inc., 573-591 (1996).

[106] H. Minoda, K. Yagi, F.-J. Meyer zu Heringdorf, A. Meier, D. Kähler, M. Horn von Hoegen, *Phys. Rev. B* **59**, 2363 (1999).

[107] B. X. Yang, Y. Ishikawa, T. Ozeki, H. Hasegawa, *Jpn. J. Appl. Phys.* **35** 1 (2b), 1267 (1996).

[108] H. H. Farrell, C. J. Palmstrom, *J. Vac. Sci. Technol. B* **8**, 903 (1990).

[109] see for instance Q.-K. Xue, T. Hashizume, T. Sakurai, *Appl. Surf. Sci.* **141**, 244 (1999).

[110] T. Hashizume, Q.-K. Xue, A. Ichimiya, T. Sakurai, *Phys. Rev. B* **51**, 4200 (1995).

[111] P. J. Jensen, K. H. Bennemann, *Phys. Rev. B* **42**, 849 (1990).

[112] L. D. Landau, E. M. Lifshitz, L. P. Pitaevskii, *Electrodynamics of Continuous Media*, Chaps. 4 and 5, 2nd edition, Butterworth-Heinenann (Reed Elsevier), Oxford (1999).

[113] H. Horner, C. M. Varma *Phys. Rev. Lett* **20**, 845 (1995).

[114] Y. Millev, J. Kirschner, *Phys. Rev. B* **54**, 4137 (1996).

[115] Y. Millev, H. P. Oepen, J. Kirschner, *Phys. Rev. B* **57**, 5837 (1998), Y. Millev, H. P. Oepen, J. Kirschner, *Phys. Rev. B* **57**, 5848 (1998).

[116] A. Moschel, K. D. Usadel, *Phys. Rev. B* **49**, 12868 (1994), A. Moschel, K. D. Usadel, *Phys. Rev. B* **51**, 16111 (1995).

[117] C. Liu, S. D. Bader, *J. Magn. Magn. Mater.* **93**, 307 (1991).

[118] B. Heinrich, Z. Celinski, J. F. Cochran, A. S. Arrott, K. Myrtle, *J. Appl. Phys.* **70**, 5769 (1991), and references herein.

[119] H. J. Elmers, U. Gradmann, *Appl. Phys. A* **51**, 225 (1990).

[120] K. Takanashi, S. Mitani, M. Sano, H. Fujimori, H. Nakajima, A. Osawa, *Appl. Phys. Lett.* **67**, 1016 (1995).

[121] S. Mitani, K. Takanashi, H. Nakajima, K. Sato, R. Schreiber, P. Grünberg, H. Fujimori, *J. Magn. Magn. Mater.* **156**, 7 (1996).

[122] K. Takanashi, S. Mitani, K. Himi, H. Fujimori, *Appl. Phys. Lett.* **72**, 737 (1998).

[123] D. P. Pappas, K.-P. Kämper, H. Hopster, *Phys. Rev. Lett.* **64**, 3179 (1990).

[124] E. Vedmedenko, H. P. Oepen, A. Ghazali, J.-C. S. Lévy, J. Kirschner, *Phys. Rev. Lett.* **84**, 5884 (2000).

[125] S. S. P. Parkin, K. P. Roche, M. G. Samant, P. M. Rice, R. B. Beyers, R. E. Scheuerlein, E. J. O'Sullivan, S. L. Brown, J. Bucchigano, D. W. Abraham, Yu Lu, M. Rooks. P. L. Trouilloud, R. A. Wanner, W. J. Gallagher, *J. Appl. Phys.* **85**, 5828 (1998).

[126] see for instance S. Chikazumi, in *Physics of Ferromagnetism*, Clarendon Press, Oxford (1997), and W. J. M. de Jonge, P. J. H. Bloemen, F. J. A. Broeder in *Ultrathin Magnetic Structures I*, eds. J. A. C. Bland and B. Heinrich, Springer-Verlag, 65 (1994).

[127] W. L. O'Brien, T. Droubay, B. P. Tonner, *Phys. Rev. B* **54**, 9297 (1996).

Appendix A

Curriculum vitae

Personal data:

Name:	Florin Zavaliche
Date of birth:	January 09, 1970
Place of birth:	Bacău, Romania
Marital status:	Married

Education and professional experience:

Sept. 1976 – June 1984:	Primary School Nr. 10, Bacău, Romania
Sept. 1984 – June 1988:	Industrial High School Nr. 1, Bacău, Romania
Sept. 1988 – July 1989:	Military service
Oct. 1989 – July 1994:	University of Bucharest, Bucharest, Romania. **Diploma thesis**: The study of X-ray emission from plasma focus
Oct. 1994 – Aug. 1996:	research assistant in the National Institute of Materials Physics, Bucharest, Romania. **Research topic**: the structure of amorphous, quasicrystalline, and metastable crystalline alloys.
Oct. 1996 – July 1997:	DAAD scholarship holder at the Technical University of Chemnitz, Germany. **Research topic**: electronic transport properties in amorphous and quasicrystalline thin film alloys.

Sept. 1997 – June 1998:	graduate visiting student at the University of Virginia, Charlottesville, USA.
	Research topic: preparation and electronic transport in bulk intermetallic and quasicrystalline alloys.
Since July 1998:	Ph.D. candidate at Max-Planck-Institut für Mikrostrukturphysik, Halle, Germany.
	Supervisor: Prof. Dr. Jürgen Kirschner
	Thesis: The metal-semiconductor interface: Fe-Si(001) and Fe-InP(001)

Halle, April 22, 2002   Florin Zavaliche

Appendix B

Erklärung

Ich versichere hiermit, die vorliegende Dissertation

The metal-semiconductor interface: Fe-Si(001) and Fe-InP(001)

selbständig verfaßt und keine anderen als die von mir angegebenen Quellen und Hilfsmittel verwendet zu haben. Die den benutzten Werken wörtlich oder inhaltlich entnommennen Stellen sind als solche kenntlich gemacht.

Halle, April 22, 2002 Florin Zavaliche

Appendix C

Acknowledgements

It is so little just saying "Thank you!" to my supervisor, Professor Jürgen Kirschner, for making possible my work into his group! Without his permanent guidance and confidence in my work, none of my scientific achievements would have been possible. It is he whom I owe my initiation into the secrets of the nano-world and my current scientific profile.

I am grateful to Dr. Wulf Wulfhekel for his patience in unveiling me his vast experience in surface science and for his sharing with me the experimental tricks making everything possible. There is really a great thing the friendly atmosphere he created around him.

I will always be deeply indebted to Professor Rodica Mănăilă and Professor Andrei Devenyi for their endless patience and confidence in my person. They did not only open the door of scientific research for the young graduate student I was, but also taught me much more than physics. I would like to say a heartfelt "thank you" to Dr. Dan Macovei for the permanent support and friendship he offered to me.

Many thanks to Professor Marek Przybylski, Professor Bretislav Heinrich and Professor Hans Peter Oepen for the numerous and fruitful discussions we have had.

I owe a significant amount of my scientific achievements to Professor Joe Poon, Professor Peter Häussler and Dr. Roland Haberkern, who offered me the possibility of working in their groups, and taught me so much about making science.

I show my gratitude for their helping hands and useful hints to PD Dr. Holger L. Meyerheim, Dr. Manfred Klaua, Dr. Jochen Barthel, Dr. Haifeng Ding, Dr. Gerold Steierl, Dr. Wolfgang Kuch, Dr. Marin Alexe, Dr. Dimitrie Iorgov, Dr. Sabine Pütter, Dr. Wim Lutzke. I thank also to my Canadian colleagues, Dr. Ted L. Monchesky and Mr. Radovan Urban for the great collaboration we had had during their stay in Halle.

My life during the Ph.D. work was made much easier by the spirited discussions with Dr. Riccardo Hertel, Dr. Simona Bodea, Dr. Radian Popescu, Dr. Hartmut Schwabe, Mr. Fabrizio Porrati, Mr. Liviu Chelaru, Mr. Jerzy Grabowsky about and beyond physics.

I would like to greatly acknowledge the constant assistance and kindness of Ms. Doreen Röder, Mrs. Heike Menge, Mr. Herbert Engelhard, Mr. Detlef Hartung, Mr. Eberhard Hunold, Mr. Günter Kroder, Mr. Ralph Dietmann, Dr. Roland Scholz, Dr. Wilfried Erfurth, Mrs. Ursel Doß and Mrs. Sigrid Hopfe.

For an experimental Ph.D. can hardly be conceived without the permanent help of the colleagues from the mechanical and electronic workshop, I would like say a warm "thank you" to Mr. Jürgen Wille, Mr. Bernd Rau, Mr. Klaus Hänecke, Mr. Wolfgang Eberhardt, Mr. Michael Oppelt and Mr. Detlef Proske.

I should not forget to thank to Dr. Wolfgang Keller, Mr. Detlef Hoehl, Mrs. Martina Witzig, Mrs. Karin Pohlink, Mrs. Birgit Frankenstein, Mrs. Andrea Amm and Mrs. Annelies Kroder for their permanent help and kindness.

Many thanks to Rodica Alexe, Viorel Drăgoi, Paul and Manuela Miclea, Nicoleta and Ionuţ Radu, Hermina and Cătălin Harnagea along with my newest friend Alexandra, Alina Vişinoiu, Oana and Cristian Cojocaru for the friendship they showed to me and for the great time we have had together.

I owe a lot to the DAAD foundation for offering me the possibility of coming into contact with the German scientific community and becoming acquainted with the magnificent culture and customs of the German people.

My special thanks go to my mother and my wife, Delia, for their constant love and support throughout the years of my Ph.D. work.